Effects of uniaxial pressure on the charge density wave state in intermetallic systems

by

Fellipe Baptista Carneiro

Centro Brasileiro de Pesquisas Físicas

Advisor:
Eduardo M. Bittar

Doctoral Thesis

March 2024

1949 | 2024 75 ANOS CBPF

César Lattes 100 ANOS 1924 | 2024

MINISTÉRIO DA
CIÊNCIA,TECNOLOGIA
E INOVAÇÃO

GOVERNO FEDERAL
BRASIL
UNIÃO E RECONSTRUÇÃO

"EFFECTS OF UNIAXIAL PRESSURE ON THE CHARGE DENSITY WAVE STATE IN INTERMETALLIC SYSTEMS"

FELLIPE BAPTISTA CARNEIRO

Tese de Doutorado em Física apresentada no Centro Brasileiro de Pesquisas Físicas do Ministério da Ciência Tecnologia e Inovação. Fazendo parte da banca examinadora os seguintes professores:

Eduardo M. Bittar

Eduardo Matzenbacher Bittar - Orientador/CBPF

Victor Carozo Gois de Oliveira

Victor Carozo Gois de Oliveira – PUC-RIO

Luis Ghivelder

Luis Ghivelder – UFRJ

Ricardo D. Reis

Ricardo Donizeth dos Reis – CNPEM/LNLS

Documento assinado digitalmente
gov.br
NATANAEL DE CARVALHO COSTA
Data: 31/03/2024 21:10:32-0300
Verifique em https://validar.iti.gov.br

Natanael de Carvalho Costa – UFRJ

Rio de Janeiro, 26 de março de 2024.

Centro Brasileiro de Pesquisas Físicas
Rua Doutor Xavier Sigaud, 150, URCA, Rio de Janeiro, Brasil
Tel.: +55 21 2141-7100 CEP:22290-180
http://www.cbpf.br

Acknowledgment

I would like to thank my parents Vinicus and Sonia, and my sister, Fabiane, for always being my support and fundamental in my life.

I would like to thank my longstanding friends Lucas and Quemuel for being at my side for as long as I can remember, your friendship was always fundamental to me.

I would like to thanks to my advisor, Eduardo, for his commitment to my academic and professional journey, which began during my undergraduate studies. I am grateful for his dedication in sparing no efforts to provide me with the best opportunities to develop and refine my skills.

I would like to thanks my lab colleagues, Calazans, Allan, and Henrique for our friendiship and for always helping me at the lab throughout the years.

I would like to thank Sean and Priscila, for your invaluable support, hospitality and guidance during my stay in Los Alamos and for helping me to achieve the works presented here.

I would like to thank Gabriel and Pascoal, which I met during my stay in Los Alamos for their valuable help, friendship and discussions.

I also would like to thank the entire SCES team in LANL, for all the support and insightful discussions. Specially thanks to Ajeesh and Clement for all help in set up experiments.

I would like to thank CNPq, for the financial support.

Finally, I would like to thank the CBPF, for all the support during my academic formation.

Work at Los Alamos was supported by the U.S. Department of Energy, Office of Basic Energy Sciences, Division of Materials Science and Engineering project “Quantum Fluctuations in Narrow-Band Systems”.

This study was financed in part by the Coordenação de Aperfeiçoamento de Pessoal de Nível Superior - Brasil (CAPES) - Finance Code 001 and Conselho Nacional de Desenvolvimento Científico e Tecnológico (CNPq).

Abstract

Charge density waves (CDW) are a phenomenon that has garnered attention in the condensed matter physics community due to their intricate interplay between electronic, structural, and thermal properties in various materials. CDW are characterized by periodic modulations in the material's electron density, which can be formed altogether with lattice distortions. Interestingly, these density waves can take different forms, depending on the crystal symmetry and local coupling between the electronic and lattice degrees of freedom. Therefore, perturbations in the crystal symmetry act as a tuning parameter to selectively break local electronic and lattice symmetries and may lead to changes in the properties of the materials. Nowadays, studies under uniaxial pressure can provide such tunability. In this thesis, we use this tool combined with the AC-elastocaloric effect and electrical transport probes to study the effect of uniaxial pressure on two charge density wave systems, namely, $La_3Co_4Sn_{13}$ and ScV_6Sn_6. In $La_3Co_4Sn_{13}$ We demonstrate the unconventional behavior of these states under uniaxial pressure, which markedly contrasts with previous measurements under hydrostatic pressure. Our study reveals a potential connection between the charge density wave (CDW) and superconducting states with the anisotropy in the electronic structure. It also uncovers a possible domain physics of the CDW order for measurements along the ordering vector. In ScV_6Sn_6 we found a substantial anisotropy between in-plane and out-of-plane thermal expansion coefficients. Our electrical resistivity measurements under c-axis uniaxial stress reveal a fast suppression of the CDW transition followed by a change in the CDW character for $\sigma_c > 1$ GPa. Isotherm resistance *versus* c-axis uniaxial stress measurements unveil a secondary kink preceding the main transition, which persists down to lower temperatures. Our findings suggest a stress-induced modification of the CDW order in ScV_6Sn_6 and highlight the importance of c axis lattice parameter for tuning the CDW order in this material. Additionally, we report the growth of ScV_6Sn_6 single-crystalline samples with *c*-axis rod shapes, which are suitable for measurements under uniaxial pressure.

Resumo

Ondas de densidade de carga (CDW) são um fenômeno que tem atraído atenção na comunidade de física da matéria condensada devido à sua complexa interação entre propriedades eletrônicas, estruturais e térmicas em vários materiais. CDWs são caracterizadas por modulações periódicas na densidade de elétrons do material, que podem ser formadas juntamente com distorções na rede cristalina. Interessantemente, essas ondas de densidade podem assumir diferentes formas, dependendo da simetria do cristal e do acoplamento local entre os graus de liberdade eletrônicos e da rede. Portanto, perturbações na simetria do cristal atuam como um parâmetro de ajuste para romper seletivamente as simetrias eletrônicas e da rede locais e podem levar a mudanças nas propriedades dos materiais. Atualmente, estudos sob pressão uniaxial podem proporcionar tal ajustabilidade. Nesta tese, utilizamos essa ferramenta combinada com o efeito AC-elastocalórico e sondas de transporte elétrico para estudar o efeito da pressão uniaxial em dois sistemas de ondas de densidade de carga, a saber, La_3Co4Sn13 e ScV_6Sn_6. Em La_3Co4Sn13, demonstramos o comportamento não convencional desses estados sob pressão uniaxial, que contrasta marcadamente com medições anteriores sob pressão hidrostática. Nosso estudo revela uma conexão potencial entre os estados de onda de densidade de carga (CDW) e supercondutividade com a anisotropia na estrutura eletrônica. Ele também revela uma possível física de domínios da ordem CDW para medições ao longo do vetor de ordenamento. Em ScV_6Sn_6, encontramos uma anisotropia substancial entre os coeficientes de expansão térmica no plano e fora do plano. Nossas medições de resistividade elétrica sob estresse uniaxial no eixo c revelam uma rápida supressão da transição CDW seguida por uma mudança no caráter da CDW para $\sigma_c > 1$ GPa. Medições de resistência isotérmica *versus* estresse uniaxial no eixo c revelam uma torção secundária precedendo a transição principal, que persiste até temperaturas mais baixas. Nossos achados sugerem uma modificação induzida por estresse na ordem CDW em ScV_6Sn_6 e destacam a importância do parâmetro de rede do eixo c para ajustar a ordem CDW neste material. Adicionalmente, relatamos o crescimento de amostras monocristalinas de ScV_6Sn_6 com formas de bastão no eixo c, que são adequadas para medições sob pressão uniaxial.

Contents

List of Figures

List of Tables

Chapter 1

Introduction

The collective phenomena of charge density waves (CDW) have been studied for over a century, and its relationship with the material's properties is a subject of great interest in condensed matter physics. Such electronic modulations commonly arise in the normal state of conventional or unconventional superconductors. They can either compete or coexist with the superconducting state, and this interplay is usually studied using hydrostatic pressure and/or chemical substitution. There are several examples in the literature where the CDW can be suppressed using hydrostatic pressure and chemical doping, and, as a counterpart, the superconducting state is enhanced [1, 2, 3]. Among these examples, one can find a variety of materials such as ceramic High-T_c superconductors, intermetallic, and layered systems [4, 5, 6]. Therefore, comprehensive studies on the CDW state properties are desirable to understand this ordered state's role in the emergence of superconducting states. Despite the significant advantages of hydrostatic pressure studies, since the pressure is equally applied in all crystallographic directions, it cannot reveal any symmetry-related dependence of the CDW or superconductor order parameter. On the other hand, uniaxial pressure has proved to be a powerful tool to reveal symmetry-related dependencies of the order parameter of exotic phases, such as in multi-component superconductors and nematic transitions, in which the order parameter can couple to the uniaxial pressure in different ways [7, 8, 9]. In CDW systems, it is known that the charge order can break the transitional symmetry, which, in consequence, creates a strong anisotropy in the material's properties [10, 11, 12]. This makes the use of uniaxial pressure extremely useful to fully understand the phase diagram of compounds presenting phase transitions of this nature.

Long-ranged CDW have remarkable signatures in most of the physical characterization techniques frequently available in modern condensed matter laboratories, such as heat capacity, electrical transport, magnetic susceptibility, and X-ray diffraction. However, combining these techniques with the use of uniaxial pressure cells is not always trivial work, which makes the use of this experimental tool often focused on electrical transport, with a few research groups actively engaged in this research domain. However, with the improvement of uniaxial strain/stress cells [13], the newly developed AC elastocaloric effect (AC-ECE) measurements brought a new perspective to studying thermodynamic signatures under uniaxial pressure and the dependence of the elastocaloric signal with uniaxial pressure can bring new information regarding the nature of the transition and its dependence on the symmetries of the system. With the high signal-to-noise ratio compared with other AC techniques [14], AC-ECE has been used to study the thermodynamic signatures of phase transitions under uniaxial pressure in various materials [15, 16, 17]. Here, we are focused on the use of electrical transport and AC elastocaloric effect under uniaxial pressure to study two CDW intermetallic systems: $La_3Co_4Sn_{13}$ (3-4-13) and ScV_6Sn_6 (1-6-6). The first compound (3-4-13) is a cubic system that presents a CDW transition around $T_{CDW} \sim 145$ K and a superconducting state at $T_c \sim 2.7$ K [18]. The second compound (1-6-6) is a newly discovered Kagome material [19], with a long-ranged CDW transition at $T_{CDW} \sim 84$–93 K and a short-ranged CDW that appear at room temperature and seems to compete with the long-range order once the latter emerges [20].

This thesis is organized in six chapters. In chapter 2 are shown the main theoretical aspects to understand and analyze our results. The chapter 3 describes the main experimental techniques used in this work.

Throughout the chapter 4, we present the study of the 3-4-13 compound under uniaxial pressure. Probing the superconducting and CDW transition using electrical resistivity measurements and AC-ECE. In the 3-4-13 compound, we found striking differences in the dependence of CDW and SC states between hydrostatic and uniaxial pressure at different crystallographic directions, with the superconducting transition being suppressed for three high symmetry directions, [100], [110], and [111] at different rates in the later. Along [110] direction we observe a possible signature of CDW domain physics.

Chapter 5 illustrates the results on 1-6-6 compound, studied using heat capacity, thermal expansion and the effects of *c*-axis uniaxial and hydrostatic pressure on the CDW transition. We observe that CDW transition is suppressed more rapidly for pressures along the *c*-axis than for hydrostatic pressure. An important anisotropy between the in-plane and out-of-plane components of the thermal expansion coefficient was found. We discuss two possible scenarios to explain the observed results, one based on the competing CDW correlations and the other based o the rich nature of the electronic structure of this compound.

In the appendix A, we briefly describe the Dark-field X-ray microscopy (DFXM) technique, used to explore another intermetallic CDW compound, $\mathrm{Sr_{0.4}Ca_{0.6}Rh_4Sn_{13}}$. We show preliminary results on exploring this new synchrotron-based image technique to study the domain physics of the CDW across the superconducting transition in this material. Due to the complexity of the data analysis this study is not complete, and was not included in the main text of the thesis.

The Appendix B shows a list of the articles related to this thesis, and in appendix C, the articles from collaborations during the PhD.

Chapter 2

Theoretical Framework

In this chapter will be given a general overview of the theoretical aspects covering charge density waves in solids, superconductivity and the concepts of uniaxial pressure.

2.1 Charge density waves

Peierls and Fröhlich [15, 22] introduced the concept of charge density waves (CDW) in one-dimensional (1D) systems. It was postulated that a metallic system confined to one dimension would exhibit instability at low temperatures, leading to periodic lattice distortion and the emergence of a gap in the electronic spectrum. It was demonstrated that this lattice distortion would induce a modulation in the density of conduction electrons, a phenomenon known as a charge density wave.

The ground state resulting from this lattice distortion was shown to be energetically favorable for the electron-phonon system. Despite the elastic energy cost associated with the crystal lattice distortion, the energy gain from the formation of the electronic spectrum gap outweighed it [23]. Figure 2.1 provides a schematic representation of the electronic dispersion relation in a one-dimensional lattice with periodicity a before and after the Peierls transition. Notably, after the transition, the lattice parameter doubles, creating a periodic structure in the density $\rho(x)$ of conduction electrons (equation 2.1) with a propagation vector of $q = 2k_F$:

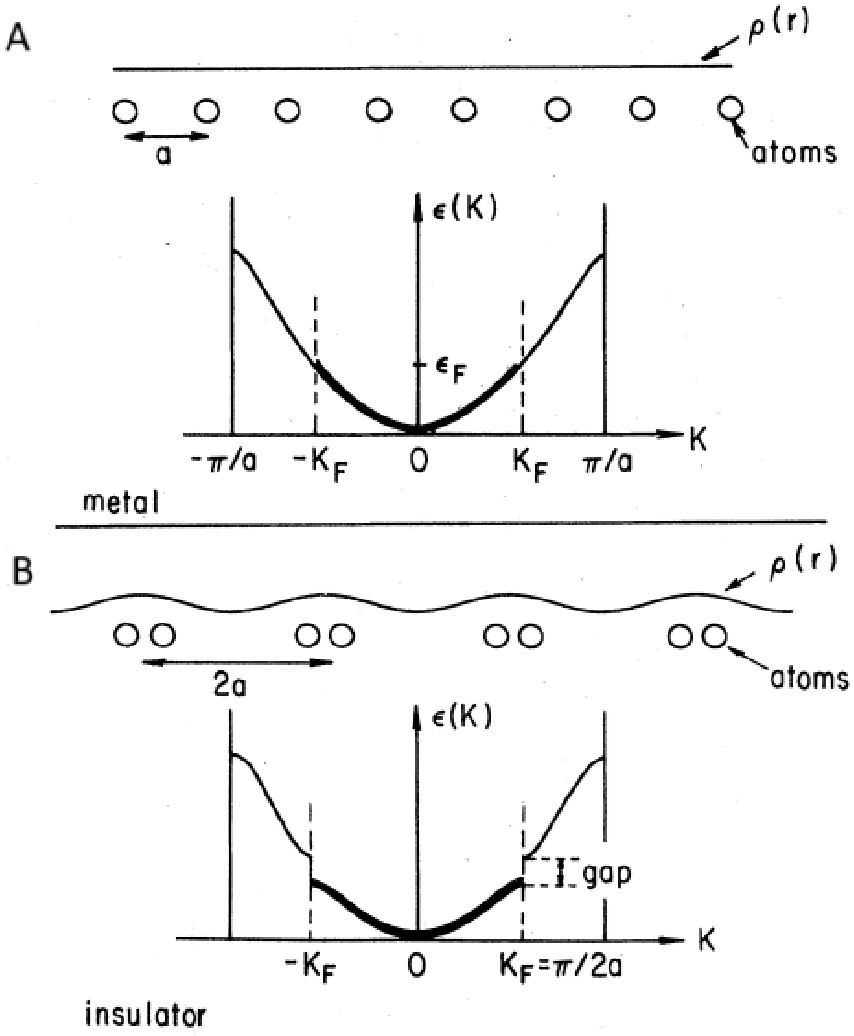

Figure 2.1: Single-particle electronic band structure in 1D lattice above (A) and below (B) CDW transition. Figure from reference [23].

$$\rho(x) = \rho_0 + \rho_1 cos(2k_F x + \phi), \tag{2.1}$$

where ρ_0 is the density without the presence of modulation, ϕ is a phase, k_F is the Fermi vector, and ρ_1 is the amplitude of the modulation, which depends on the gap (Δ) formed in the spectrum.

In the spectrum of a one-dimensional system (as shown in Figure 2.1), the Fermi surface (FS) is formed by two points connected by a vector q=$2k_F$, characterizing a condition of perfect nesting. The general definition of FS nesting is when surface regions are connected by the same wave vector $\mathbf{q}$ in momentum space. Quantitatively, Lindhard's formulation can be used to measure the nesting of the FS. If the real part of the so-called Lindhard response function $\chi'(\mathbf{q})$, also known in the literature as the nesting function [18], exhibits a divergence at a certain wave vector $\mathbf{q}$, it is considered a nesting vector. The nesting function is given by:

$$\chi'(\mathbf{q}) = \sum_k \frac{f(\varepsilon_\mathbf{k}) - f(\varepsilon_{\mathbf{k}+\mathbf{q}})}{\varepsilon_\mathbf{k} - \varepsilon_{\mathbf{k}+\mathbf{q}}}, \tag{2.2}$$

where $f(\varepsilon_\mathbf{k})$ is the well-known Fermi distribution function, and $\varepsilon_\mathbf{k}$ is the energy of the band at a specific position $\mathbf{k}$ in reciprocal space. The divergence in $\chi'(\mathbf{q})$ occurs when various regions of the Fermi surface are connected by the same wave vector $\mathbf{q}$, resulting in $\varepsilon_\mathbf{k} \rightarrow \varepsilon_{\mathbf{k}+\mathbf{q}}$. Consequently, $\chi'(\mathbf{q}) \rightarrow \infty$. However, this divergence strongly depends on the system's dimensionality. In one dimension, nesting is considered perfect because the Fermi surface, in reality, consists of two fixed points, causing the divergence in $\chi'(\mathbf{q})$ to be much more pronounced than in two or three dimensions. This is exemplified in Figure 2.2A for an electron gas in 1D, 2D, and 3D, and the instability at $q = 2k_F$, as proposed by Peierls.

Typically, a transition involving charge density waves (CDW) can be elucidated by employing a model in which the free electron gas interacts with the underlying lattice via $e - ph$ coupling. The Fröhlich Hamiltonian is often employed to characterize such a model:

$$\hat{H} = \sum_\mathbf{k} \varepsilon_\mathbf{k} \hat{a}^\dagger_\mathbf{k} \hat{a}_\mathbf{k} + \sum_\mathbf{q} \hbar\omega_\mathbf{q} \hat{b}^\dagger_\mathbf{q} \hat{b}_\mathbf{q} + g \sum_{\mathbf{k},\mathbf{q}} \left(\hat{a}^\dagger_{\mathbf{k}+\mathbf{q}} \hat{a}_\mathbf{k} \hat{b}_\mathbf{q} + \hat{a}^\dagger_\mathbf{k} \hat{a}_{\mathbf{k}+\mathbf{q}} \hat{b}^\dagger_{-\mathbf{q}} \right), \tag{2.3}$$

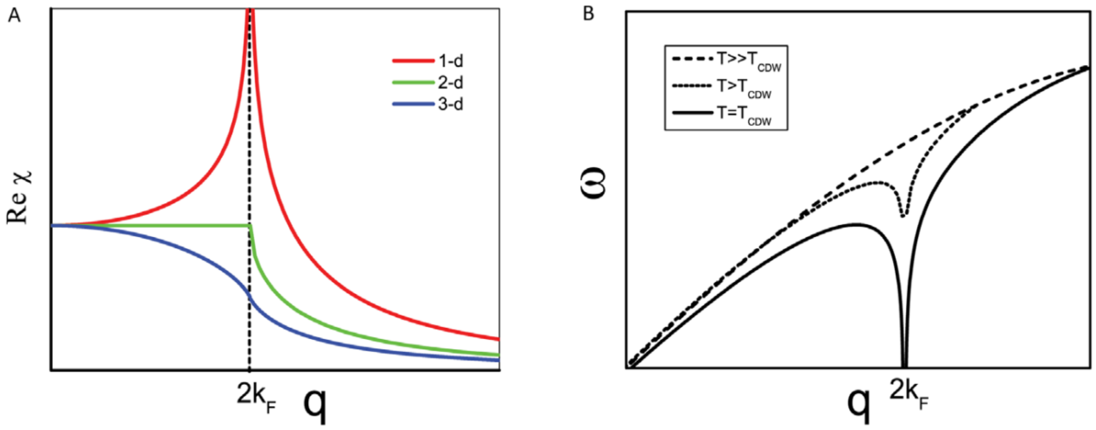

Figure 2.2: Divergence in the nesting function for different system dimensions (A). Kohn anomaly in phonon spectrum due to the CDW transition (B). Figure from reference [29].

the first term is the free electron gas Hamiltonian, where $\hat{a}^{\dagger}_{\mathbf{k}}$ and $\hat{a}_{\mathbf{k}}$, are the creation and annihilation operators for electrons states with energy $\varepsilon_{\mathbf{k}}$ and wave vector $\mathbf{k}$. The second term is the bare phonon term, $\hat{b}^{\dagger}_{\mathbf{q}}$ and $\hat{b}_{\mathbf{q}}$ are the creation and annihilation operators for phonons with energy $\hbar\omega_{\mathbf{q}}$ and momentum $\mathbf{q}$. The last term describes the interaction between electrons and phonons with a coupling constant g. The phonon frequencies can be re-normalized, giving:

$$\tilde{\omega}^2_{\mathbf{q}} = \omega^2_{\mathbf{q}}\left(1 + \frac{2g}{\hbar\omega_{\mathbf{q}}}\chi'(\mathbf{q})\right), \tag{2.4}$$

where, $\chi'(\mathbf{q})$ is the Lindhard function, mentioned earlier. For a 1D system, the eq.2.2 it becomes:

$$\chi'(q) = -e^2 n(\varepsilon_F) ln\left|\frac{q+2k_F}{q-2k_F}\right|, \tag{2.5}$$

e is the electron charge and $n(\varepsilon_F)$ is the density of states. Combining eq. 2.5 with the eq. 2.4, one obtains:

$$\tilde{\omega}^2_q = \omega^2_q\left(1 - \frac{2ge^2 n(\varepsilon_F)}{\hbar\omega_q} ln\left|\frac{q+2k_F}{q-2k_F}\right|\right). \tag{2.6}$$

As one can see, as $q \to 2k_F$ the logarithm part diverges, and the phonon frequency will be reduced, as shown in figure 2.2B. This is the so-called *Kohn anomaly*, which is a signature of the Fermi surface in the vibration spectrum [25]. Electronic excitation with zero energy at $q = 2k_F$ will effectively screen any lattice vibration at this wave vector, creating a dip in the phonon spectrum as the system approaches T_{CDW}.

The formulation above is grounded in the weak-coupling limit of electron-phonon (*e-ph*) interactions, where the coupling term g is $\mathbf{q}$-independent. This entails the computation of the phonon self-energy at the lowest order, drawing parallels in mathematical terms with the BCS theory of superconductivity [22, 26]. The theory predicts that the ratio of the CDW gap to T_{CDW} is $2\Delta/k_BT_{CDW} \approx 3.52$. However, numerous systems have exhibited substantial ratios that cannot be accounted for by this approximation. McMillan [26], based on Raman experimental data of the CDW system $2H$-TaSe$_2$, proposed that the elevated ratio suggests an extremely small correlation length during the transition (a few lattice spacings). This implies that phonons spanning a broad range in the Brillouin zone will be softened at the transition, leading to a significantly larger contribution to entropy than electronic entropy. In 1983, a comprehensive microscopic strong-coupling theory for CDW was introduced in collaboration with C. M. Varma and A. L. Simons [27]. The key components of this theory involved the pronounced wave-vector dependency of electronically induced anharmonicity and phonon mode-mode coupling. Consequently, this interplay results in a reduction in the transition temperature and a substantial wave-vector-dependent softening of phonons, elucidating the significant $2\Delta/T_{CDW}$ ratio and the presence of short correlation lengths. Hence, CDW are typically divided into two regimes: the weak-coupling scenario, where CDW predominantly originates from Fermi surface instabilities (primarily electronic), and the strong-coupling scenario, characterized by intense *e-ph* interactions. The primary method for determining the origin of the CDW in a particular material lies in the measurement of phonon dispersion, serving as the main experimental evidence for classification. In contrast to the bare electronic susceptibility $\chi'(\mathbf{q})$, the phonon spectrum can be directly observed through experiments employing inelastic neutron or X-ray scattering. Figure 2.3 illustrates the contrast in phonon softening between the weak-coupling (A) and strong-coupling (B) regimes around the CDW wave vector ($\mathbf{Q}_{CDW}$). In the weak-coupling scenario, the anomaly is sharply localized around

$\mathbf{Q}_{CDW}$, whereas in the strong-coupling regime, the softening occurs over an extended range of $\mathbf{Q}$ around $\mathbf{Q}_{CDW}$.

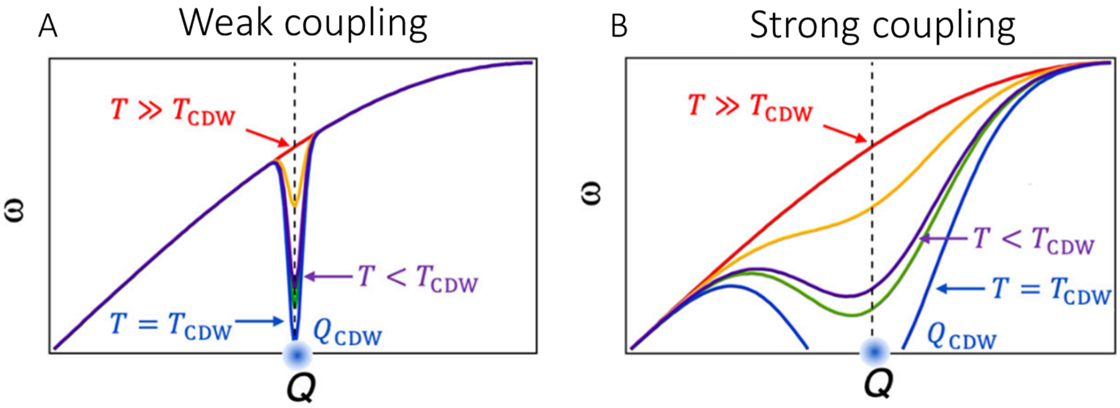

Figure 2.3: Phonon softening due to a charge density wave transition in weak- (A) and strong-coupling (B) regimes. Figure adapted from [28].

In the realm of materials with dimensions greater than 1, the mechanism guiding a charge density wave transition becomes more complex. It is widely acknowledged that various pathways exist for a material to undergo such a transition, owing to the unconventional nature of Fermi surface nesting in high-dimensional materials. It is noteworthy that this was pointed out by M. D. Johannes and I. I. Mazin [18]. They argued that only a small fraction of the observed charge ordering phase transitions in real materials are true analogs of the Peierls instability, and this is because the electronic instabilities which may drive a CDW are easily destroyed by even small deviations from perfect nesting conditions. Moreover, they reinforced the importance of the $e-ph$ coupling for the CDW formation, even for low-dimensional materials. In real materials, a structural distortion and the appearance of a gap at the Fermi level occur. However, the inherent complexity of the Fermi surface may result in a partial Fermi surface reconstruction, affecting the physical properties differently. For instance, in electrical resistivity measurements as a function of temperature, $\rho(T)$, this distinction becomes apparent. As exemplified by the 1D chain TTF-TCQN [29], a metal-insulator transition is observed (Figure 2.4A). This behavior is anticipated for Peierls-like CDW with a fully gapped Fermi surface. On the contrary, compounds like in the quasi-1D NbSe_3, an observable upturn initiates at $T = 149$ K and a secondary CDW transition at $T =$59 K (Figure 2.4B), leading to

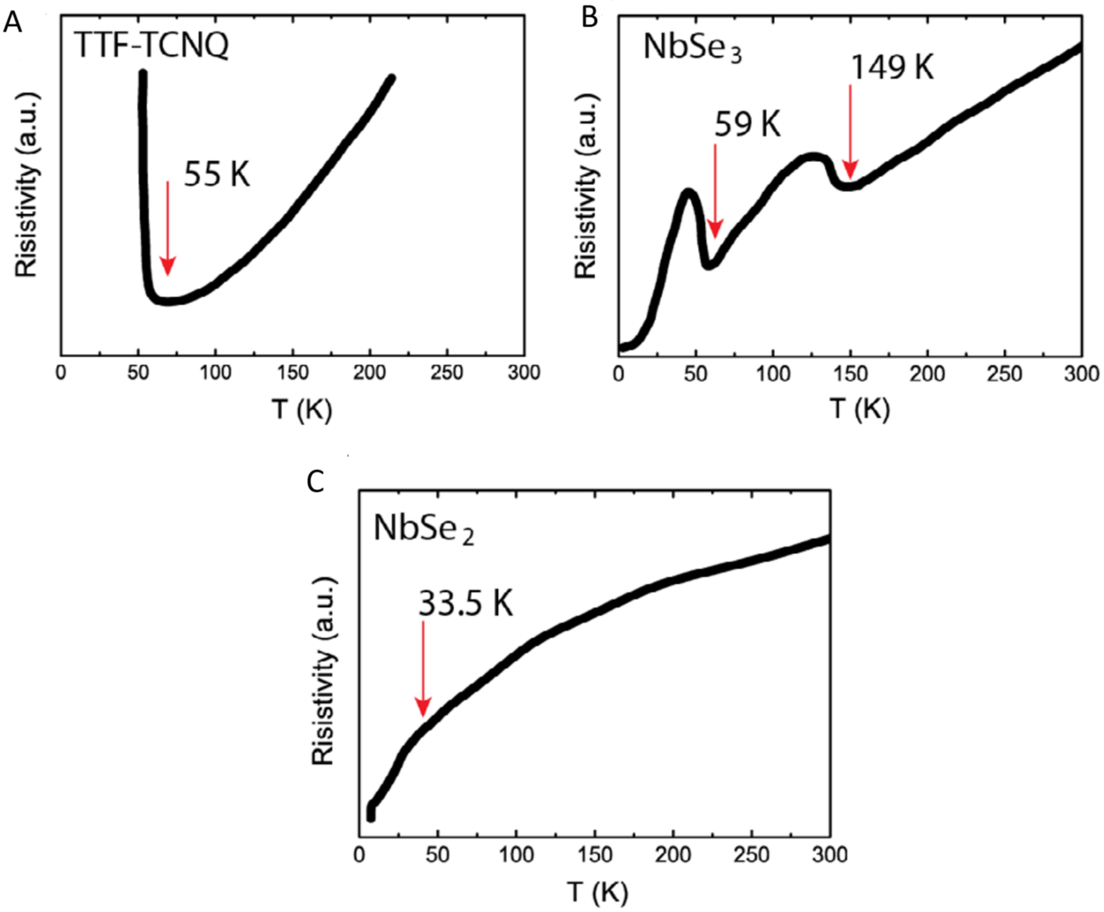

Figure 2.4: Resistivity vs. temperature measurements for typical CDW materials. (A) 1d chain TTF-TCQN (B) 1d chain NbSe$_3$ (C) 2d layered NbSe$_2$. Figure from reference [29].

an increase in electrical resistivity. However, post-transition, the material retains its metallic character, with $\rho(T)$ decreasing with temperature. A third example is the 2D-layered material $NbSe_2$, where the anomaly in resistivity is even smaller (Figure 2.4C). Thus, the way a CDW transition manifests in transport properties is strongly dependent of the Fermi surface topology.

In conclusion, the driven forces behind CDW instabilities are extremely material-dependent. Purely electronic Peierls-like CDW are the less common examples and the $e-ph$ coupling is widely accepted to play the major role in the CDW formation.

2.2 Thermodynamic signatures of CDW

In thermodynamic measurements like heat capacity and thermal expansion, the presence of a substantial change in system entropy during the transition manifests as a characteristic jump-like or step-like feature. These features are observed in many CDW systems [30, 31, 32, 33]. As a practical example, the figure 2.5A and B shows the heat capacity and linear thermal expansion measurements of the compound $LaPt_2Si_2$. Where a CDW transition is observed around $T_{CDW} = 80$ K [32].

One can use the Landau formulation for second-order phase transitions to describe a CDW phase transformation for $T < T_{CDW}$. The first terms of the Taylor's expansion of the Landau free energy can be written as:

$$F = F_0 + a(T - T_{CDW})\Phi^2 + b\Phi^4, \tag{2.7}$$

where, F_0 is the temperature dependence of the high temperature phase, a and b are positive phenomenological parameters which depend on the specific nature of the system and are continuous functions of thermodynamic parameters like the temperature and Φ is the CDW order parameter. Minimizing the energy with respect to the order parameter, i.e.,

$$\frac{\partial F}{\partial \Phi} = 0 = 2a(T - T_{CDW})\Phi + 4b\Phi^3, \tag{2.8}$$

and solving for Φ yields two solutions, the order parameter that minimizes the free

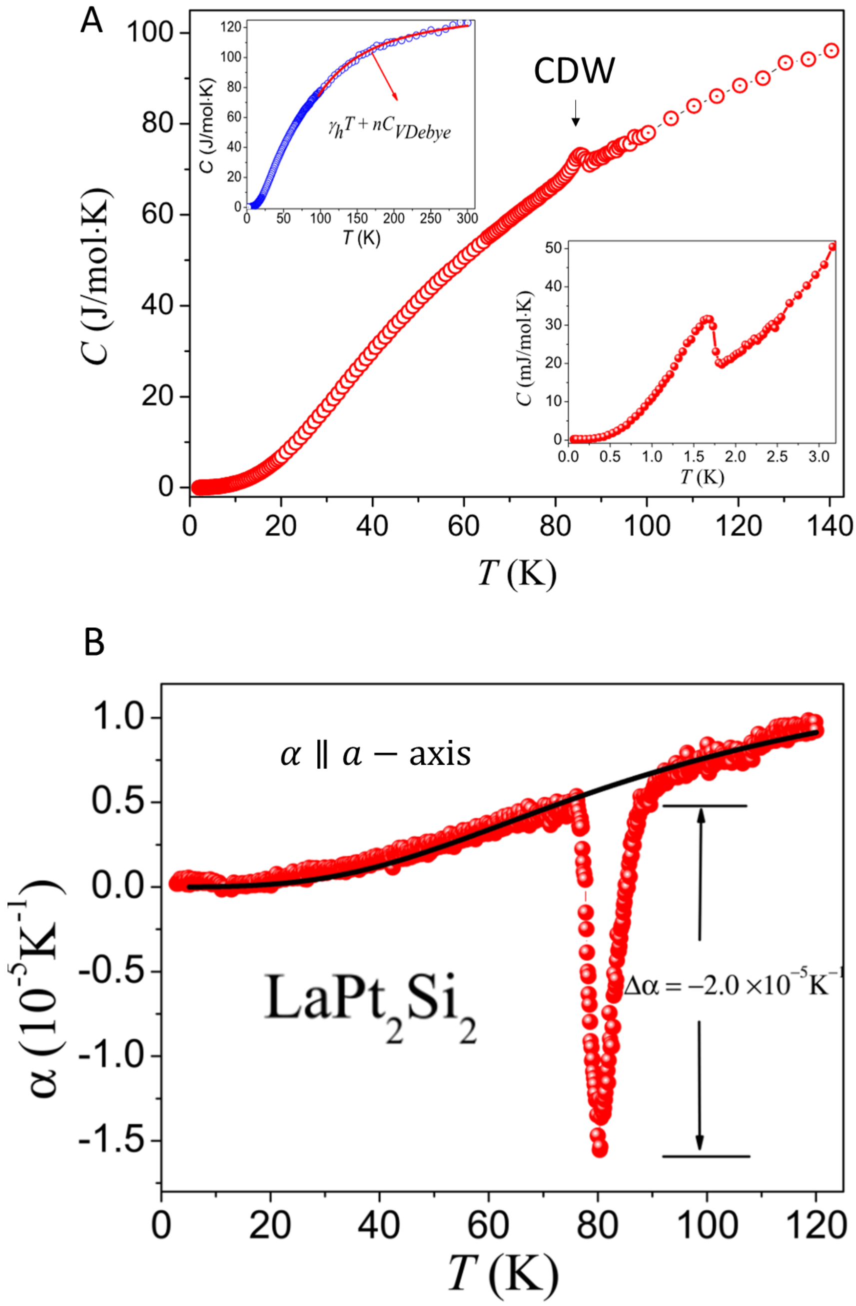

Figure 2.5: Heat capacity (A) and linear thermal expansion (B) measurement along the *a* axis of $LaPt_2Si_2$. Figure from reference [32].

energy is:

$$\Phi^2 = \frac{aT_{CDW}}{2b}\left(1 - \frac{T}{T_{CDW}}\right). \tag{2.9}$$

The entropy and the heat capacity can also be obtained:

$$\begin{aligned} S &= -\frac{\partial F}{\partial T}, & (2.10)\\ C_P &= T\left(\frac{\partial S}{\partial T}\right)_P. & (2.11) \end{aligned}$$

At $T = T_{CDW}$ there is a discontinuity in C_P:

$$\Delta C_P = \frac{a^2 T_{CDW}}{2b}. \tag{2.12}$$

Considering volume change in the phase transition, one can write the differential form of Gibbs free energy:

$$dG = VdP - SdT. \tag{2.13}$$

In a second order phase transition, theres no discontinuity in the frist derivative of the free energy:

$$dG_1 = V_1 dP - S_1 dT = V_2 dP - S_2 dT = dG_2. \tag{2.14}$$

Where 1 and 2 are the two phases, above and below T_{CDW}. Defining the volume thermal expansion β as:

$$\beta = \frac{1}{V}\left(\frac{\partial V}{\partial T}\right), \tag{2.15}$$

and using β and C_P in 2.14, one obtains:

$$V_1\beta_1 dP - \frac{C_{P,1}}{T_1}dT = V_2\beta_2 dP - \frac{C_{P,2}}{T_2}dT. \tag{2.16}$$

Rearranging this equation, using $\Delta\beta = \beta_1 - \beta_2$ and $\Delta C_P = C_{P,1} - C_{P,2}$.

$$\frac{\Delta C_P}{T}dT = V\Delta\beta dP. \tag{2.17}$$

At the phase transition, where there is a jump in the thermal expansion and heat capacity,

$$\frac{dT_{CDW}}{dP} = \frac{\Delta\beta T_{CDW} V}{\Delta C_P}. \tag{2.18}$$

This is the so called Ehrenfest relation. Where it relates the pressure dependence of the transition temperature with the jumps in β and C_P at the phase transition. This can be useful to determine the sensitivity of the phase transition with pressure. Moreover, unlike the ΔC_P, which is always positive. $\Delta\beta$ can have negative sign, which determines whether the rate dT_{CDW}/dP will be positive or negative, so that one can tell from heat capacity and thermal expansion measurements if the transition is suppressed or enhanced under pressure. Different authors commonly use the uniaxial pressure version of this equation, substituting the volume thermal expansion β by the linear thermal expansion α_i and the pressure P by the pressure applied in specific directions P_i (uniaxial). This gives:

$$\frac{dT_{CDW}}{dP_i} = \frac{\Delta\alpha_i T_{CDW} V}{\Delta C_P}, \tag{2.19}$$

where the index i denotes the direction. The relative jump sizes in the thermal expansion can be used to state which direction the transition temperature is more sensible to uniaxial pressure. To exemplify the situation where the thermal expansion step has two different sings depending on the crystallographic direction, see the thermal expansion curves for for LaAgSb$_2$ in figure 2.6. This material has two CDW transitions (marked by the vertical dashed lines). The thermal expansion feature at T_{CDW1} for α_a shows a positive step, while for α_c is negative. Since the jump feature in c is more pronounced than in a, it will dominate the volume thermal expansion β, shown in the green curve [33]. In conclusion, the thermal expansion and heat capacity measurements can be useful to determine the pressure sensitivity of CDW phase transitions [33].

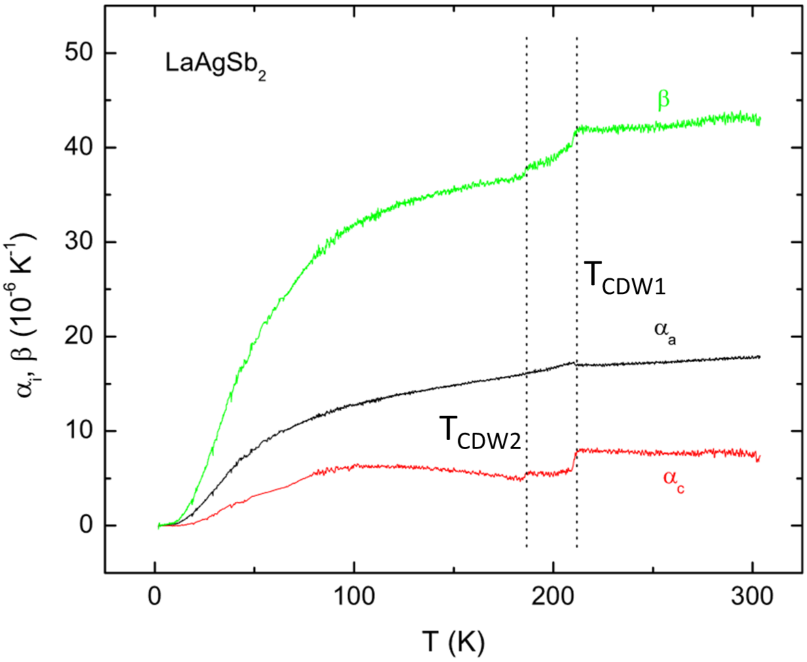

Figure 2.6: Temperature dependent linear thermal expansion measurements at different crystallographic directions a (black curve) and c (red curve) for LaAgSb$_2$. The green curve represents the volume thermal expansion β. Figure from reference [33].

2.3 Superconductivity

In 1913, the physicist H. K. Onnes made a significant discovery regarding Mercury (Hg) at low temperatures. When measuring the electrical resistivity as a function of temperature, he observed a remarkable phenomenon: the resistance of the element dropped to zero at $T_c = 4.2$ K [34], as illustrated in Figure 2.7A. Several years later, W. Meissner and R. Ochsenfeld uncovered another intriguing property. Within the superconducting state, the material exhibited the expulsion of magnetic flux (behaving as a perfect paramagnet), as depicted in Figure 2.7B. This phenomenon came to be known as the Meissner effect [35]. If the magnetic field is large enough, above a certain critical value H_c, the field is allowed to penetrate and the material recovers the normal state. These observations led to a crucial inference: the superconducting state constitutes a thermodynamic equilibrium state. Consequently, the state remains independent of the path that led to its realization. If alterations occur in the magnetic field or temperature, ultimately, the only conditions that must hold are $T < T_c$ and $H < H_c$.

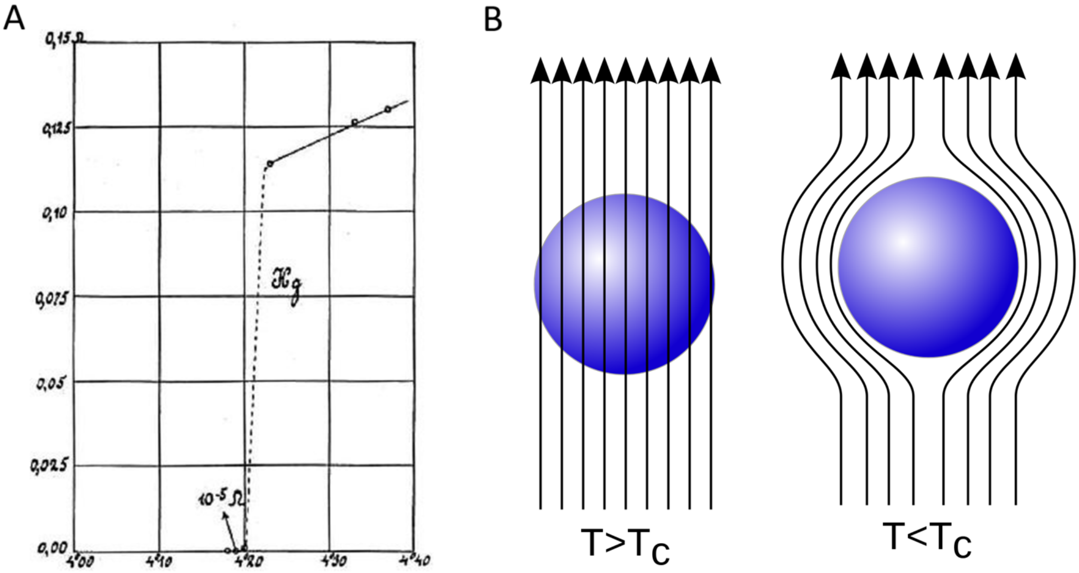

Figure 2.7: (A) Resistance vs temperature of Hg. Figure adapted from original plot of H. K. Onnes [34]. (B) Schematics of the Meissner effect (Author: Piotr Jaworski; PioM EN DE PL 22:10, 21 August 2005 (UTC); POLAND/Poznań)

The inaugural phenomenological theory explicating the observations of Onnes and Meissner was formulated by the London brothers [36]. They derived an equation to characterize the properties of superconductors:

$$\nabla \times \mathbf{J_s} = -\frac{n_s e^2}{mc}\mathbf{B}.$$

Here, $\mathbf{J_s}$ represents the supercurrent, $-e$ denotes the electron charge, and n_s is the density of superelectrons. This equation suggests that the application of an external magnetic field induces supercurrents, subsequently nullifying the flux within the material, explaining the Meissner effect. Despite the comprehensive phenomenological description, it falls short of explaining the underlying reason for the materials undergoing such a phase transition.

The resolution to this question came from Bardeen, Cooper, and Schrieffer, who, in 1957—46 years after Onnes' discovery—developed the BCS theory for superconductivity [37]. This theory relies on more rigorous quantum mechanical arguments and is grounded in the concept of the effective attractive interaction of electrons mediated by phonons. Despite the inherent repulsiveness of the direct electrostatic interaction between electrons, lattice vibrations can screen the Coulomb interaction, resulting in an attractive potential. In the second quantization, they have written the following Hamiltonian:

$$H = \sum_{\mathbf{k},\sigma} \varepsilon_{\mathbf{k}} c^{\dagger}_{\mathbf{k},\sigma} c_{\mathbf{k},\sigma} + \frac{1}{N} \sum_{\mathbf{k},\mathbf{k'}} V_{\mathbf{k},\mathbf{k'}} c^{\dagger}_{\mathbf{k}\uparrow} c^{\dagger}_{-\mathbf{k}\downarrow} c_{-\mathbf{k}\uparrow} c_{\mathbf{k}\downarrow}. \tag{2.20}$$

The first term is the kinetic energy of the electrons, $c^{\dagger}_{\mathbf{k},\sigma}$ and $c_{\mathbf{k},\sigma}$ are the creation and annihilation operators of an electron with momentum $\mathbf{k}$ and spin σ. The second term is the interaction between electrons mediated by phonons and the matrix element $V_{\mathbf{k},\mathbf{k'}}$ can be treated in mean field approximation as constant average $< V_{\mathbf{k},\mathbf{k'}} > = V$. From thermodynamic calculations, one can obtain a relation between the effective attractive potential V and the superconducting transition temperature T_c:

$$k_B T_c \approx 1.13 \hbar \omega_c e^{-\frac{1}{N_0 V}}. \tag{2.21}$$

Where N_0 is the density of states at the Fermi level and ω_c is the Debye phonon frequency. Another important relation is the ratio between the superconducting gap and the transition temperature:

$$\frac{\Delta(0)}{k_B T_c} = 1.76. \tag{2.22}$$

The theory also predicts the ratio between the jump in heat capacity ΔC and its value in the normal state C_n:

$$\frac{\Delta C}{C_n}|_{T \approx T_c} = 1.76. \tag{2.23}$$

This prediction agrees with the experiments to about 10 percent, the only exceptions are the strong-coupled superconductors, such as lead and mercury. All of these findings effectively characterized traditional type-I superconductors within the weak-coupling limit. However, there exists another category of superconductors, known as type-II superconductors, where a mixed phase between normal and superconducting states occurs. In this class, the applied magnetic field is permitted to partially penetrate the material volume, giving rise to a vortex state. A.A. Abrikosov employed the Ginzburg-Landau (GL) phenomenological theory to elucidate the characteristics of type-II superconductors [38]. And using the GL combined with the BCS theory, one can obtain an equation for the superconducting critical field:

$$H_c(T) = 1.74 H_c(0)\left(1 - \frac{T}{T_c}\right). \tag{2.24}$$

It is also noteworthy to mention the existance of the unconventional superconductivity. Unconventional superconductors represent a fascinating and complex area of condensed matter physics, characterized by their unique mechanisms of superconductivity that deviate from the BCS theory. Unlike conventional superconductors, where electron pairing (Cooper pairs) is mediated by phonons, unconventional superconductors often involve alternative pairing mechanisms such as spin fluctuations or electronic correlations. These materials exhibit a wide variety of exotic properties, including high-temperature superconductivity, as seen in cuprates and iron-based compounds, as well as the presence of unusual symmetries in their superconducting order parameters. The study of unconventional superconductors is driven by their potential applications in technology and their ability to provide deeper insights into quantum mechanical phenomena. Understanding the interplay between their electronic, magnetic, and structural properties remains a major scientific challenge, promising to unlock new principles of physics and paving the way for advancements in material science and quantum computing [39].

2.4 Strain and Stress

When a material undergoes a load, one can describe the deformation suffered using two quantities: The stress and strain within the material. The stress measures how the force is spread in the material in units of N/m^2. The strain is the dimensionless quantity that measures the displacement that occurred due to the applied stress relative to the material's original size. The strain within a material can be described as infinitesimal deformations represented by the deformation vector $\mathbf{u}$, relative to the object original coordinates $\mathbf{x}$. The strain tensor can be written as:

$$\varepsilon_{ij} = \frac{1}{2}\left(\frac{\partial u_i}{\partial x_j} + \frac{\partial u_j}{\partial x_i}\right), \tag{2.25}$$

where the indices i and j represent three orthogonal coordinates. One can explicitly write the six tensor components as:

$$\begin{aligned} \varepsilon_{xx} &= \frac{\partial u}{\partial x} & \varepsilon_{uv} &= \frac{1}{2}\left(\frac{\partial v}{\partial x} + \frac{\partial u}{\partial y}\right), \\ \varepsilon_{yy} &= \frac{\partial v}{\partial y} & \varepsilon_{yz} &= \frac{1}{2}\left(\frac{\partial w}{\partial y} + \frac{\partial v}{\partial z}\right), \\ \varepsilon_{zz} &= \frac{\partial w}{\partial z} & \varepsilon_{xz} &= \frac{1}{2}\left(\frac{\partial w}{\partial z} + \frac{\partial u}{\partial z}\right), \end{aligned} \tag{2.26}$$

where u, v and w are the three components of the deformation vector $\mathbf{u}$ and x, y and z are the coordinates. Therefore the full strain tensor is:

$$\varepsilon = \begin{pmatrix} \varepsilon_{xx} & \varepsilon_{uv} & \varepsilon_{xz} \\ \varepsilon_{yx} & \varepsilon_{yy} & \varepsilon_{yz} \\ \varepsilon_{zx} & \varepsilon_{zy} & \varepsilon_{zz} \end{pmatrix}. \tag{2.27}$$

The engineering definitions of normal and shear stress and strain are depicted in

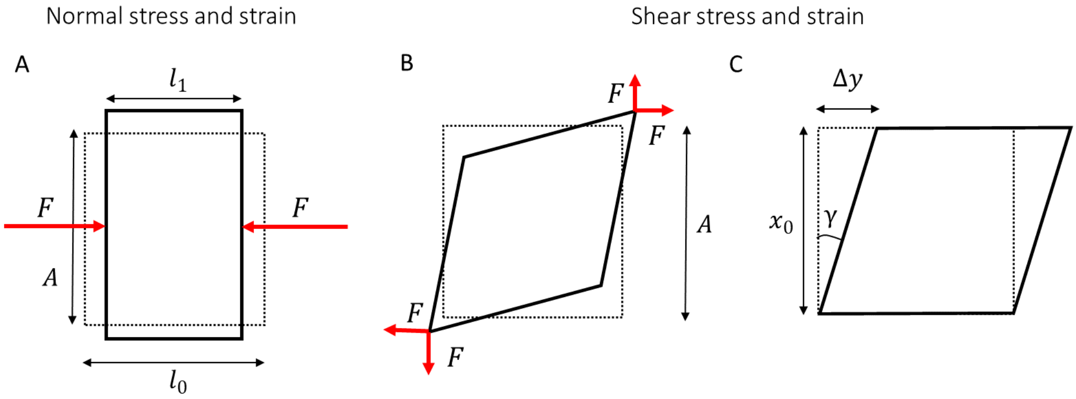

Figure 2.8: The engineering definitions of normal (A) and shear stress and strain (B and C.)

figure 2.8A, B, and C. The normal strain is defined as the uniaxial change of the material length in regarding the force applied in the same direction:

$$\varepsilon = \frac{l_1 - l_0}{l_0} = \frac{\Delta l}{l_0}, \tag{2.28}$$

and the stress in this case is simply:

$$\sigma = \frac{F}{A}, \tag{2.29}$$

where F is the applied force and A is the area. For the sear stress (τ) and shear strain (γ), the following relations are given:

$$\tau = \frac{F}{A}; \qquad \tan\gamma = \frac{\Delta y}{x_0} \approx \gamma. \quad . \tag{2.30}$$

For low pressures, *i.e.*, within the elastic region and uniaxially deformed material, the stress σ and strain ε are connected by the Hooke's law:

$$\sigma = E\varepsilon, \tag{2.31}$$

where E is the Young's modulus. Analogously, for the shear strain/stress $\tau = G\gamma$, where G is the shear modulus. Figure 2.9 shows how these two quantities are correlated for an ordinary metal.

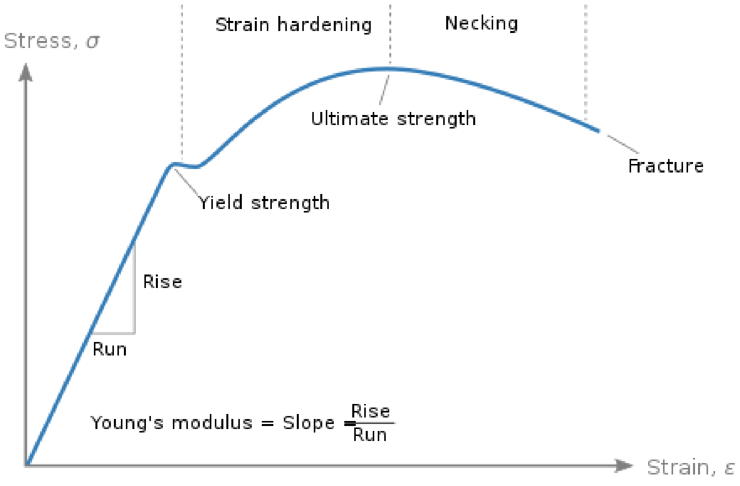

Figure 2.9: Stress vs strain curve for an ordinary metal. Figure adapted from reference [40]

More generally, in three dimensions, E and G are a 6 × 6 tensor, called stiffness tensor $\mathbf{C}$ and the relation between stress and strain become $\sigma_{ij} = C_{ijkl}\varepsilon_{kl}$. There are, at most, 21 independent components that can be reduced depending on other symmetry relations in the material. For instance, for a cubic material, there are only 3 independent components, and the Hooke's law matrix becomes:

$$\begin{pmatrix} \sigma_{xx} \\ \sigma_{yy} \\ \sigma_{zz} \\ \sigma_{yz} \\ \sigma_{xz} \\ \sigma_{uv} \end{pmatrix} = \begin{pmatrix} C_{11} & C_{12} & C_{12} & 0 & 0 & 0 \\ C_{12} & C_{11} & C_{12} & 0 & 0 & 0 \\ C_{12} & C_{11} & C_{12} & 0 & 0 & 0 \\ 0 & 0 & 0 & C_{44} & 0 & 0 \\ 0 & 0 & 0 & 0 & C_{44} & 0 \\ 0 & 0 & 0 & 0 & 0 & C_{44} \end{pmatrix} = \begin{pmatrix} \varepsilon_{xx} \\ \varepsilon_{yy} \\ \varepsilon_{zz} \\ 2\varepsilon_{yz} \\ 2\varepsilon_{xz} \\ 2\varepsilon_{uv} \end{pmatrix}. \tag{2.32}$$

The components of the stiffness matrix elements are the elastic constants, which will depend on the materials' microscopic properties, like chemical bounds, hybridization, etc. Another important quantity to be defined is the Poisson's ratio ν, which is the ratio between transverse and longitudinal strain for longitudinal loading. For example, for high symmetry directions one can have $\nu_{uv} = -\varepsilon_{yy}/\varepsilon_{xx}$ and $\nu_{zx} = -\varepsilon_{zz}/\varepsilon_{xx}$. These quantities can help determine the anisotropic properties of the materials for loadings applied uniaxially in different directions.

Sometimes is convenient to write the strain as a function of stress through the elastic compliance matrix S_{ij}. For a cubic material:

$$S_{ij} = \begin{pmatrix} S_{11} & S_{12} & S_{12} & 0 & 0 & 0 \\ S_{12} & S_{11} & S_{12} & 0 & 0 & 0 \\ S_{12} & S_{11} & S_{12} & 0 & 0 & 0 \\ 0 & 0 & 0 & S_{44} & 0 & 0 \\ 0 & 0 & 0 & 0 & S_{44} & 0 \\ 0 & 0 & 0 & 0 & 0 & S_{44} \end{pmatrix}. \tag{2.33}$$

For a cubic system, the compliance and stiffness matrix are related by the following relations:

$$S_{11} = \frac{C_{11} + C_{12}}{(C_{11} - C_{12})(C_{11} + 2C_{12})}, \tag{2.34}$$

$$S_{12} = \frac{-C_{12}}{(C_{11} - C_{12})(C_{11} + 2C_{12})}, \tag{2.35}$$

$$S_{44} = \frac{1}{C_{44}}, \tag{2.36}$$

This relations are useful to determine the dependency of the elastic properties with the crystallographic directions. For example, the Young's modulus is directional dependence and it is possible to write a relation for the dependence of E with the Miller crystallographic index (h, k, l) [41]. For cubic symmetry:

$$\frac{1}{E_{hkl}} = S_{11} - 2\left[(S_{11} - S_{12}) - \frac{1}{2}S_{44}\right]\frac{h^2k^2 + k^2l^2 + l^2h^2}{(h^2 + k^2 + l^2)}. \tag{2.37}$$

This relation provides valuable information and enables us to correlate the material stiffness with the crystallographic directions through symmetry assumptions. Even though is necessary the prior knowledge of the matrix elastic constants C_{ij}. One can use the equation 2.37 to obtain the ratio between the Young's modulus for the main crystallographic directions. A good reference on the mechanical properties of materials and the correlation with the crystal symmetry can be found in [42].

Chapter 3

Experimental methods

In this chapter we describe the main experimental techniques used for studying the physical properties of the compounds, as well as, the methods to obtain the samples.

3.1 Single crystal growth

In the field of condensed matter physics, a key aim is to procure excellent specimens to explore the physical properties of materials. This usually entails securing single-crystalline samples, inherently characterized by their superior quality. For instance, various microscopic probes apply exclusively to single crystals, including probes for Fermi surface and band structure analysis such as Quantum oscillations and ARPES measurements. Additionally, a structural and magnetic probe like Neutron diffraction is an example of a technique that is not limited to but preferred to use single-crystalline samples. Furthermore, due to the random distribution of particles in the formation of polycrystals, these samples frequently exhibit porosity and intergranular compositions, hindering meaningful measurements of anisotropy. Throughout the years, a variety of techniques have been developed to achieve such merit and have been successful in synthesizing different classes of materials. For intermetallic compounds, one of the most famous methods of obtaining single crystals is the metallic-flux method [43, 44]. The Materials Physics Group (MPG) at CBPF and the Strongly Correlated Electron Systems (SCES) team within the Materials Physics and Applications Division's Quantum Group (MPA-Q) at LANL have employed diverse growth methods to obtain high-quality single-crystalline samples. In this work, the molten metallic-flux method was employed to obtain single crystalline samples of the studied materials.

The metallic-flux growth method is based on the use of low melting point metals (such as Al, Ga, In, Sn, Pb, Sb, Bi and Zn) as a solvent medium (flux). This method offers two primary benefits: (1) The ability to grow samples well below their melting point, resulting in materials with fewer internal defects such as strain and inhomogeneities; (2) The molten flux provides a clean growth environment, as impurities in the metal flux are typically absent in the final material.

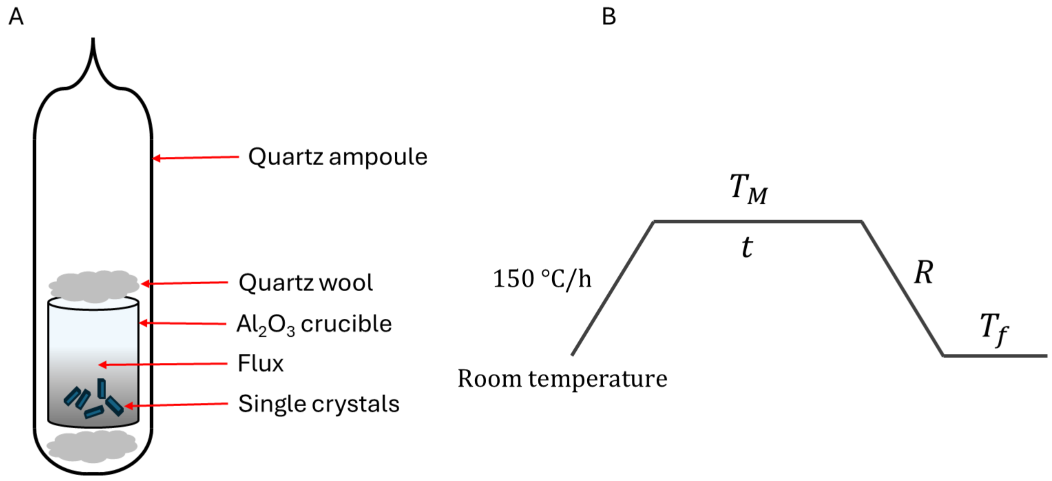

Figure 3.1: Illustration of the ampoule set (A) and an example of a temperature treatment ramp (B).

In our work, both samples ($La_3Co_4Sn_{13}$ and ScV_6Sn_6) share the Tin (Sn) in their compositions so that we were able to use this element as our flux (Sn has a melting point s low as ≈ 232 °C). The samples are weighted in the desired stochiometry with an excess of the low melting point material (Sn). For the 3-4-13 compound, we used a La:Co:Sn ratio of 1:1.3:20, and for the 1-6-6 1:6:30. The elements are then placed in an Allumina crucible (Al_2O_3) and subsequently sealed in a quartz ampoule, to avoid the components to oxide. Chunks of quartz wool are added at the bottom and top of the alumina crucible inside the quartz tube to serve as a base (preventing the ampoule from cracking) and as a filter for the flux during the centrifuging (see

Fig. 3.1A). Conventionally, the ampoules are placed in a resistance furnace and fast heated up to a temperature T_M, and maintained at this temperature by an amount of time t (usually hours), then slowly cooled down to a final temperature T_f at a rate R (Fig. 3.1B). The ampoules are inverted and centrifuged so that the flux excess is allowed to pass through the upper quartz wool, while the obtained single crystals remain inside the alumina crucible. The growth parameters necessary for producing single crystals of $La_3Co_4Sn_{13}$ using the metallic-flux technique are extensively documented in the literature and are available in other sources [18, 48, 49, 50].

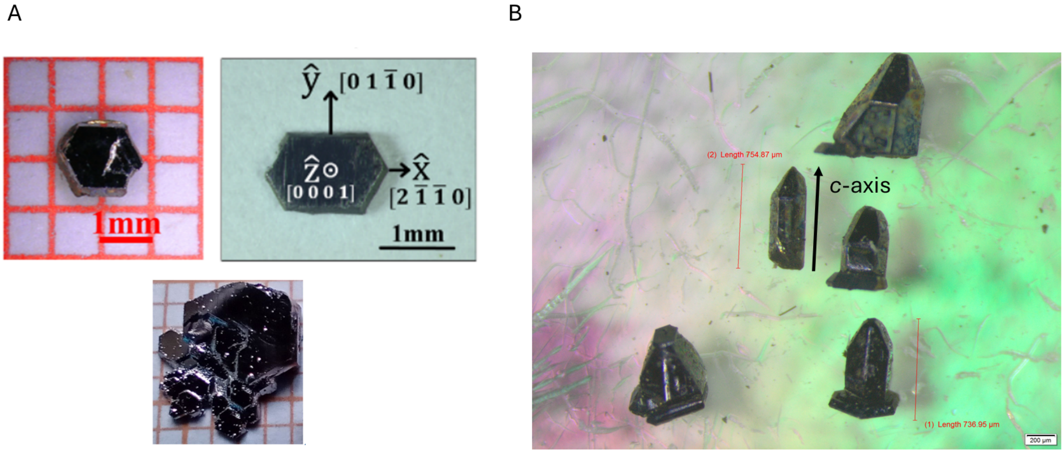

Figure 3.2: Typical single crystal habit for ScV_6Sn_6 obtained by other groups and reported in the literature [45, 46, 47] (A). Samples obtained in this work, using the adapted growth parameters (B).

Hexagonal systems often exhibit a crystal habit resembling hexagonal plates, with the *a* and *b*-axes lying in the plane and the *c*-axis having a thickness of a few micrometers. This trend holds for ScV_6Sn_6 crystals, as reported by various authors [45, 46, 47]. A noteworthy accomplishment of this thesis was the successful cultivation of ScV_6Sn_6 crystals that are elongated into rods along the *c*-axis, providing an ideal setup for conducting our studies under uniaxial pressure along the *c*-axis. This was achieved by adapting the growth parameters. While in the literature is commonly used 1:6:60, here we adopted the ratio 1:6:30, reducing the amount of flux. In the temperature treatment, the main differences were the cooling rate and the final temperature before centrifuging. In the literature, other groups usually removed the ampoules from the furnace at a temperature within T_f = 700-780 °C and used cooling rates of about R = 1-2 °C/h. In our case, the final temperature was chosen to be much lower T_f = 450 °C, while using a faster cooling rate of R = 5 °C/h. Fig. 3.2 shows the comparison between samples reported in the literature (A) and our samples obtained using the adapted growth parameters (B).

3.2 Specific heat measurements

The specific heat, denoted as c, is defined as the amount of heat energy needed to elevate the temperature of a unit mass of a substance by 1 Kelvin. Typically, it is expressed for a variable that remains constant. Under constant pressure conditions, it is given by:

$$c_P = \left(\frac{dQ}{dT}\right)_P . \tag{3.1}$$

This value is measured in units such as J/mol.K or J/g.K, depending on whether the mass or the number of moles of the substance is considered. The specific heat of a substance is contingent upon its molecular arrangement and composition. Variations in how heat energy is stored and released result in differing specific heat capacities among substances. Generally, materials with higher specific heat capacities needs more heat energy to elevate their temperature compared to those with lower capacities. In condensed matter physics, specific heat serves as a tool to investigate phase transitions, since it is sensible to changes in the entropy due to phase transitions.

The specific heat measurements in this thesis were performed in a commercially available Quantum Design PPMS (Physical Property Measurement System), using the calorimeter puck (Fig. 3.3A) available with the heat capacity option (HCO). The HCO system controls the provided and released heat to the sample, monitoring its temperature change. During a measurement, a known amount of heat is applied at constant power for a fixed time, and then this heating period is followed by a cooling period of the same duration. The underside of the sample platform features a platform heater and platform thermometer, as depicted in Figure 3.3B. Small wires serve to connect the platform heater and platform thermometer electrically while also offering thermal connection and structural support. Attachment of the sample to the platform is facilitated by a thin layer of grease, ensuring the necessary thermal contact.

The PPMS Turbo Pump or Cryopump High-Vacuum option establishes a vacuum substantial enough to render the thermal conductance between the sample platform and the thermal bath (puck) primarily reliant on the wires' conductance. This setup yields a consistent heat link to the bath, allowing ample time for both the platform and sample to attain thermal equilibrium for accurate measurements. Using this puck configuration one can measure the heat capacity of samples with typical masses of about 1 to 200 mg.

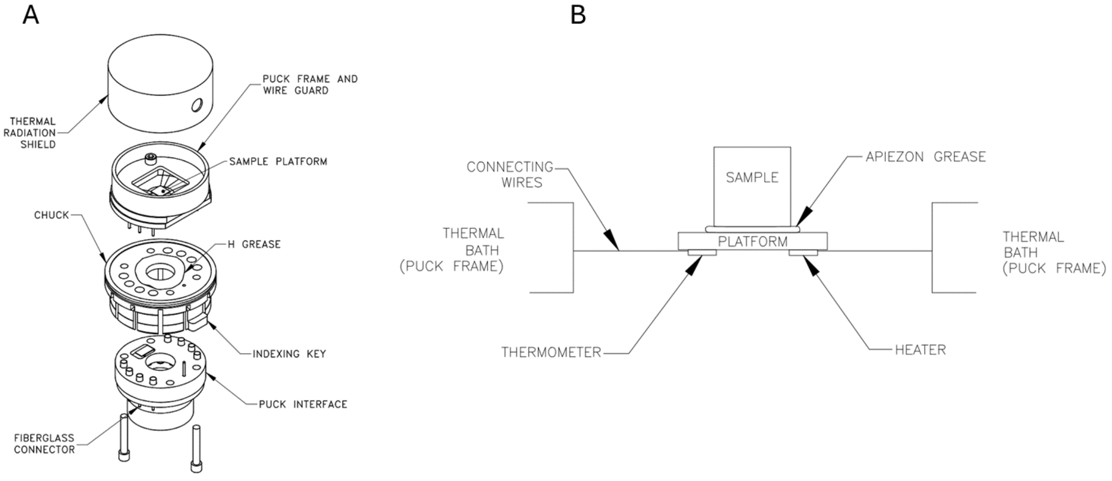

Figure 3.3: Calorimeter puck (A). Thermal connections to sample and sample Platform in PPMS HCO (B). Figures extracted from [51].

The measurements are fitted using a simple thermal relaxation model:

$$C_{total}\frac{dT}{dt} = -K_w\left(T - T_b\right) + P(t), \tag{3.2}$$

where C_{total} is the total heat capacity of the sample and the sample platform; K_w is the thermal conductance of the supporting wires; T_b is the temperature of the thermal bath; and $P(t)$ is the power applied by the heater. The solution to this equation is represented by an exponential function with a characteristic time constant denoted as $\tau = C_{\text{total}}/K_w$. Consequently, the total heat capacity can be determined. An initial measurement, referred to as addenda, is conducted to assess the heat capacity contribution originating from the puck. This value is subsequently subtracted from the total heat capacity to derive the sample's heat capacity, C_{P}. The subtraction process is automated within the PPMS measurement control software. The specific heat c_P of the sample is the measured heat capacity divided by the sample mass or the number of mols. This also can be automatically done by the software if the user inputs the sample's mass and molar mass before the measurement starts.

3.3 Thermal expansion measurements

In condensed matter physics, thermal expansion refers to the change in size, shape, or volume of a material in response to changes in temperature. It is known that the thermal expansion arises from third-order anharmonic effects in the lattice vibrations [52] and simply can be attributed to the enhancement of vibrational motion and the movement of atoms induced by increasing temperatures. Consequently, these atomic movements lead to changes in the average separation of atoms, culminating in the expansion or contraction of the solid.

The linear thermal expansion coefficient, α, can be written as:

$$\alpha = \frac{1}{L}\frac{dL}{dT}, \tag{3.3}$$

where L is material length, and T is the temperature. The volume thermal expansion is:

$$\beta = \frac{1}{L}\frac{dV}{dT}, \tag{3.4}$$

where V is the volume and for isotropic solids, $\beta = 3\alpha$.

Throughout this thesis, we have employed a high-resolution capacitive dilatometer (0.05 Å) to conduct thermal expansion measurements relative to temperature changes. In a capacitive dilatometer, the elongation ΔL of a sample with a length L results in a variation in the gap D between a set of capacitor plates. For an ideal capacitive dilatometer with parallel plates in a vacuum, the correlation between the measured capacitance C and D is defined by:

$$C = \frac{\epsilon_0 A}{D}, \tag{3.5}$$

where $\epsilon_0 = 8.854$ pF/m is the vaccum permittivity, and A is the area of the plates. Consequently, from D we were able to obtain the sample length variation ΔL. Figure 3.4A, shows the schematics of the dilatometer cell. For a detailed review of the cell functioning, see [53].

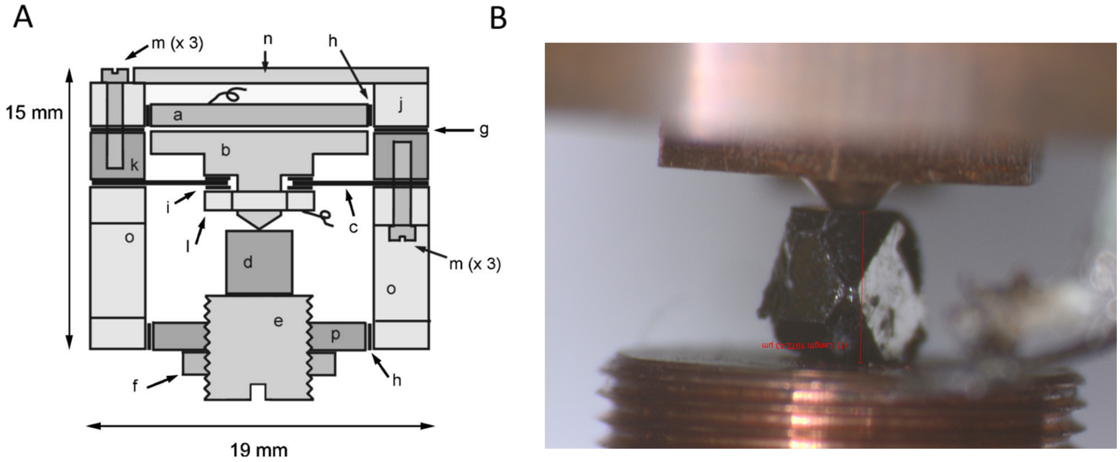

Figure 3.4: A schematic of the capacitive dilatometer. Figure extracted from [53] (A). Picture of a sample assembled in the dilatometer (B).

The following descriptions encompass the fundamental elements required for comprehending the measurement process:

(a) Upper fixed capacitor plate: Serving as the topmost plate of the capacitor, it remains stationary throughout the dilatometer operation.

(b) Lower movable capacitor plate: Positioned as the bottom plate of the capacitor, it can vertically move in response to alterations in the sample's dimensions.

(c) BeCu spring: This spring furnishes the requisite force to uphold constant pressure between the upper and lower capacitor plates.

(d) Sample;

(e) Sample platform/screw: This component houses the sample, with the screw being tightened to establish contact between the sample and the tip.

(f) Lock ring: Its purpose is to securely hold the screw in position.

(g) Copper shims: These thin copper pieces serve for electrical isolation and adjusting the sample's placement within the dilatometer.

(h) Electrical isolation: Incorporating Stycast 2850 FT, it is utilized to electrically isolate various dilatometer components.

(i) Electrical isolation: Consisting of 25 µm thick insulating washers, these are employed for insulation and spacing purposes.

The sample is affixed to the sample platform using a thin layer of grease to guarantee optimal thermal contact. The screw is adjusted until the sample makes contact with the tip of the movable lower capacitor plate. The initial capacitance C is selected to prevent the imposition of stress on the sample; typically, we ensure $C - C_0 < 5$ pF, where C_0 represents the bare capacitor capacitance value. An example of an assembled sample is shown in Fig. 3.4B.

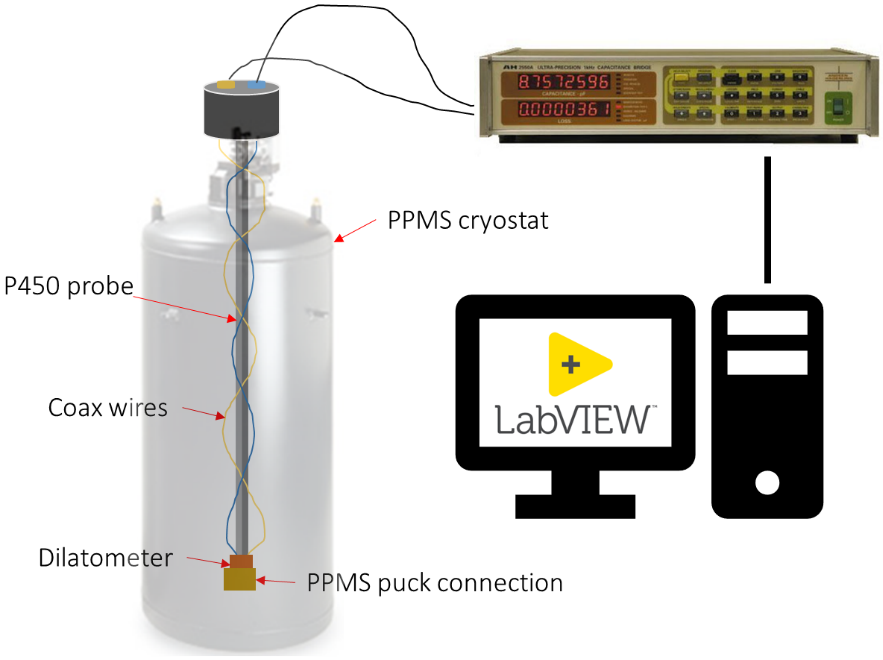

Figure 3.5: A schematic of the thermal expansion measurement setup.

To perform the measurements as a function of temperature, the cell is adapted in a Quantum Design multi-function probe P450 so that it can be loaded into a PPMS system. A pair of coaxial wires are soldered to the manganin wires (curled lines in Fig. 3.4A) attached to the capacitor plates in the cell. These internal coaxial cables are coiled throughout the probe, and connected to coax terminals on the top. The capacitance data acquisition is made by connecting an AH2550 capacitance bridge to external coaxial chords coming from the probe top. An example of this setup is given in Fig. 3.5.

In order to calculate the absolute value of the sample's thermal expansion coefficient $\alpha(T)$, it's necessary to consider the thermal expansion coefficients of the cell components, particularly Copper (Cu). The sample's thermal expansion curve can then be estimated by:

$$\alpha_{sample} = \frac{1}{L}\frac{dL}{dT}\bigg|_{cell+sample} - \frac{1}{L}\frac{dL}{dT}\bigg|_{cell} + \alpha_{Cu}. \tag{3.6}$$

The first term denotes the measurement conducted with the sample placed within the cell. The second term, known as the "cell effect," is determined by positioning the sample platform (e) against the tip of the lower capacitor plate (b) and executing temperature sweeps under identical parameters used in the samples' measurements (preferentially in the same cryostat). The coefficient α_{Cu} is the thermal expansion coefficient of copper, readily available in the literature.

3.4 Electrical transport measurements at ambient pressure

Resistivity measurements often reveal important information about critical phenomena in condensed matter systems. Sudden changes or anomalies in resistivity can indicate the occurrence of changes in the electronic structure due to phase transitions, such as the transition from a conductor to an insulator, or the onset of superconductivity. Due to its simplicity, it is widely spread in laboratories and can be done using simple electronics. The method utilized for these measurements is also applied for the measurements under uniaxial pressure.

All measurements in this thesis were performed using the 4-point probe method, to mitigate the internal contact resistance. The current leads are attached to the sample edges and the internal contacts are used to measure the voltage drop (See Fig. 3.6). The temperature sweeps were done using a PPMS system as a cryostat, with the electrical resistance measured by a Lake Shore 372 AC resistance bridge attached to it.

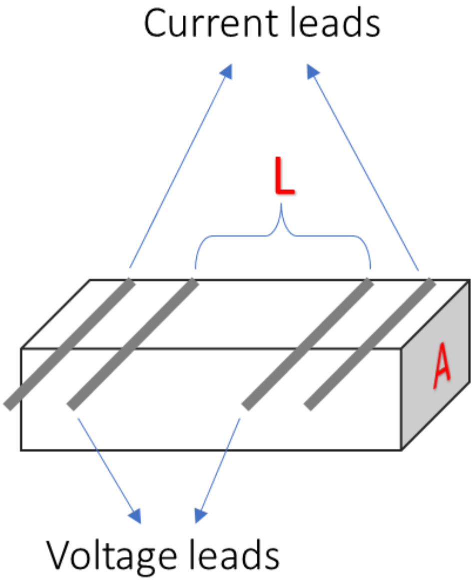

Figure 3.6: A schematic of the resistivity 4-point probe method.

The resistivity ρ of a material can be obtained by taking into account the geometric factors of the measured samples. For convenience, we commonly use a bar-shaped sample, where the cross-sectional area A and the distance between the voltage electrical leads L can be easily determined. Therefore, the resistivity of the material is given by:

$$\rho = \frac{V}{I}\frac{A}{L} = R\frac{A}{L}, \tag{3.7}$$

where I is the electrical current across the material and V is the voltage drop between the voltage leads so that, $R = V/I$.

3.5 Uniaxial pressure cells

The study of materials properties under different conditions is a central and general field in condensed matter physics. The development of experimental techniques is often connected to the necessity of creating specialized environments to study the properties of a particular material more effectively. Experimental techniques have been developed throughout the years to reach higher pressures, magnetic fields, and extremely low temperatures. One technique that has been underused for years in comparison with its hydrostatic counterpart is the uniaxial pressure. However, it was recently revived with the development of a new piezoelectric apparatus, achieving higher strain homogeneity and tunability [13]. Uniaxial pressure can drive anisotropic modifications in the overlap integrals between neighboring atomic sites, leading to significantly greater alterations in materials' electronic structure than hydrostatic pressure [13]. This section describes the state-of-the-art uniaxial pressure technique and its applications, as well as the types of uniaxial pressure experimental setup used in this work.

The uniaxial pressure cells used in this thesis are piezoelectric-based, where the load is applied to the sample by driving three lead zirconate titanate (PZT) stacks aligned in parallel. The two outer PZT stacks change the relative spacing between the main cell body and a metal bridge, while the third component (inner stacks) regulates the distance between the bridge and a movable sample plate. The sample plate is stabilized and restricted to linear movement by a pair of flexures, that support one end of a bar-shaped sample, with the other end connected to the main body. For example, the maximum tensile (compressive) stress on the sample can be achieved by expanding (contracting) the outer two stacks and contracting (expanding) the inner stack. The voltage connections for the two outer and the inner stacks are independent, enabling the control of the three stacks through two separate voltages. These control voltages are denoted as V_{outer} and V_{inner}. The PZT stacks are designed in such a way as to cancel the thermal contraction, making them suitable for low-temperature experiments and, with small-sized cells, fit in most of the cryostats.

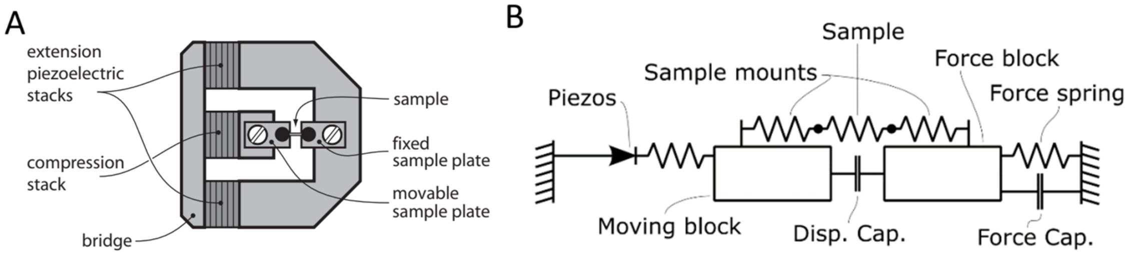

Figure 3.7: Schematics of a strain cell showing the PZT stacks configuration, valid for both cell models (A), figure from reference [13]. Functional diagram showing the cell sensors arrangement (B) figure from reference [54].

In this thesis, two types of cells were used, the strain cell CS130 and the stress cell FC100, both commercialized by Razorbill instruments. The loading mechanism is very similar for both cell models, as is shown in figure 3.7A. There are three sets of PZT stacks connected with fixed and movable sample plates. The main difference between the cells is the type of feedback sensor. In the case of the strain cell CS130, the sensor measures the displacement, which is proportional to the sample's strain, compressive, or tensile with respect to the zero-strain position of the PZT stacks. On the other hand, the FC100 model has an integrated force sensor built in series with the sample, so the force on the sensor is the same on the sample [55].

The feedback sensors rely on the variation in the capacitance of a parallel plate capacitor as the plates are moved towards and away from each other. The design of the capacitor varies slightly, but they typically have an area of a few square millimeters and an initial spacing of some tens of microns, leading to a nominal capacitance of around a picofarad (pF). Each cell comes with a calibration curve which relates the capacitance with the displacement or force in the sample. The capacitance of a parallel plate capacitor can be written as:

$$C = \frac{\varepsilon_0 A}{d}, \tag{3.8}$$

where C is the capacitance, ε_0 is the free space permittivity, A is the capacitor plate area and d is the distance between the plates. Usually the cells calibration are given by a slightly modified version of the above equation:

$$C = \frac{\alpha}{d + d_0} + C_p, \tag{3.9}$$

where, for the strain cells α is just the factor $\varepsilon_0 A$, d and d_0 are the gap between the capacitor plates and the gap at zero displacement. C_p is a capacitance term to account for imperfections in the capacitor. For the stress cells, the capacitance is proportional to the force applied to the sample then in this case:

$$C = \frac{\beta}{f + f_0} + C_p, \tag{3.10}$$

which is very similar to the later equation, however, β is the α factor multiplied by the stiffness of the spring, which converts the force applied to the sensor into a displacement for the capacitor to measure. Therefore, in the strain cells α has units of [μm.pF] and β [N.pF]. Therefore, f is the force to the sample and f_0 is the force at zero load.

Each cell is supplied with a calibration curve, with the equation fitted to experimental points. The cells can also be re calibrated as convenient, performed at the same system where the measurements will be done.

3.5.1 Sample mounting

The sample mounting is a key aspect of uniaxial pressure measurements. To achieve a good strain/stress homogeneity one must consider a good sample mounting. In this thesis, for both cells, the samples must be polished into a bar-shaped geometry, ideally with a constant cross-section. Also, high exposed length (L) to width (w) and w to thickness (t) aspect ratios helps to achieve higher strain homogeneity ($L/w \sim$ 3 - 7 and $w/t \sim 25$), and in the case of stress cells also higher applied stress to the sample. Based on the sample length, the gap between the mounting plates (exposed length L) must be determined in order to have enough epoxy length for transmitting the strain/stress to the sample [56]. Typically, an overlap between the sample and the sample plates of 200 μm is sufficient for a good mechanical contact, however, the elastic properties of the adhesive used for attaching the sample must be take into account. In this work, the epoxy used was the Locktite stycast 2850FT, hardened using Catalyst 9. The precise measurement of the elastic properties of Stycast

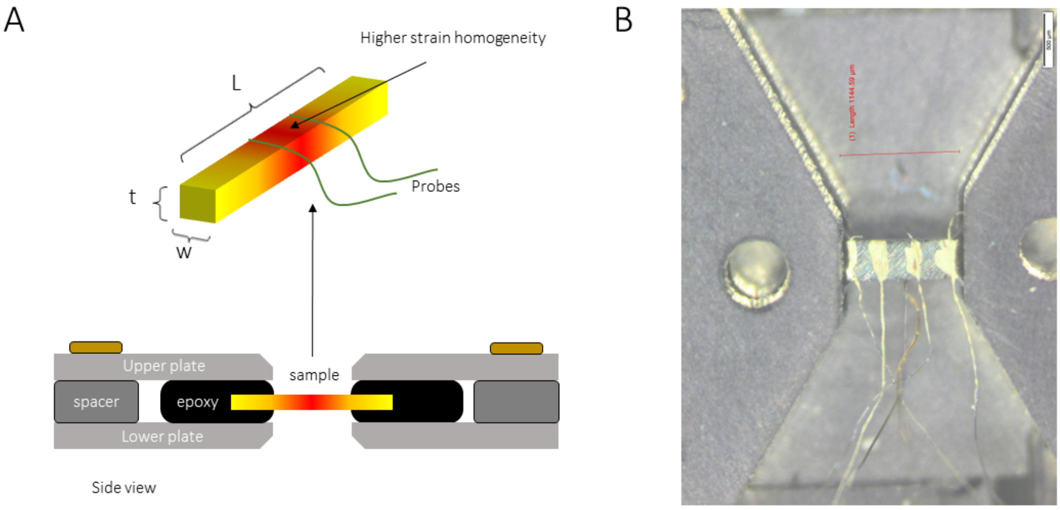

Figure 3.8: (A) Example of a sample with the $L \times w \times t$ dimensions, emphasized in the strain homogeneous part of a sample (upper image). The lower image shows the schematics of mounted sample in a strain/stress cell. (B) Image of a sample mounted in a CS130 strain cell.

2850FT at cryogenic temperatures seems to be lacking. In a technical analysis aimed at spacecraft applications, its Young's modulus was observed to incrementally rise with decreasing temperature, but seemed to stabilize below approximately 160 K. At 150 K, it was established as 11.5 GPa with Catalyst 24 LV and 16 GPa with Catalyst 9 [57]. This values are much smaller than typical sample's elastic constants, which lies about 80$\sim$100 GPa. Nonetheless, a softer epoxy can be beneficial for transmitting the strain as it deforms over a certain length of the sample, reducing stress concentration at the mounting points and hence minimizes the possibility of sample failure. Typical sample sizes are: L = 1 - 2 mm , w = 200 - 500 μm and t = 50 - 150 μm thick. Also, the higher homogeneous strained region will be concentrated at the middle of the exposed sample length. This region should be used to attach the desired probe, which will measure the physical property under investigation (voltage leads, thermocouple, susceptibility coil and etc.)

The preferred procedure for mounting the sample involves several key steps: Initially, 1 to 2 grams of epoxy are measured precisely using a scale. Then, 3.5% of the epoxy's mass is added with catalyst 9. After thorough mixing for approximately 5 minutes, the mixture is transferred to a vacuum chamber to eliminate any air bubbles, a critical step as trapped air bubbles can lead to failure points in the cured epoxy. Next, a thin layer of epoxy (approximately 25 μm thick) is applied to the lower sample mounting plate, onto which the sample is positioned. A spacer of appropriate thickness is inserted between the upper and lower mounting plates to prevent the sample from being crushed. The ends of the sample are sealed with another layer of epoxy (also about 25 μm thick), and the top plates are secured onto the sample assembly using M2 screws (refer to figure 3.8A). Curing of the epoxy can be achieved either over a 24-hour period at room temperature or by placing the cell in an oven (not exceeding 50 ° C) for a few hours. It is advised to limit heating the cell to avoid potential damage to the piezoelectric actuators. For non-urgent measurements, it is recommended to initiate the sample mounting process a couple of days before the measurements commence and allow 24 to 48 hours for the epoxy to fully cure. A detailed analysis on sample mounting and strain homogeneity can be found in [13].

3.6 Techniques under uniaxial pressure

The stress and strain cells are very versatile, the sample can be loaded in the cell with various probes on it. In this work, we focused on using electrical resistivity and the AC elastocaloric effect as transport and thermodynamic probes, respectively. The following sections describe the details of these measurements.

3.6.1 Electrical resistivity under uniaxial pressure

As mentioned in section 3.4, electrical resistivity is a world-spread characterization method in condensed matter laboratories. From now on, it is referred to as just "resistivity". The resistivity can be related to the material's quality and amount of defects in the structure, and it is sensitive to most of the phase transformations. Especially for the phase transitions studied here, charge density waves and superconductivity, the resistivity curves as a function of temperature usually present remarkable features. The gap or partial gap opened in a CDW transition appears as an upturn at T_{CDW} in the resistivity curve due to the decreasing of the density of states. Changes in ground states like CDW's usually are followed also by changes in the electron scattering rate, which will be important for the resistivity curves. In superconducting transitions, the well-known zero resistance is observed at T_c.

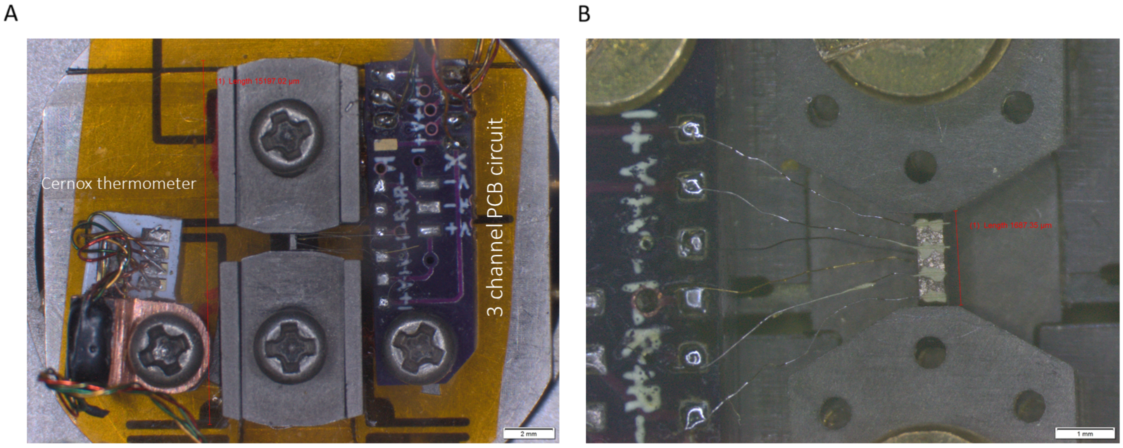

Figure 3.9: Example of mounted samples in FC100 stress cell (A) and CS130 (B).

The resistivity measurements here were done using the four-probe method described in section 3.4, where four platinum leads are attached with silver paint on the top of the sample. This method allows measuring the material's resistance without the circuit contribution and is suitable for low-resistance materials. The resistance × temperature curves were performed in a PPMS cryostat, and the resistance was measured using a Lakeshore AC370 resistance bridge. The temperature was measured using a Lakeshore AC350 temperature controller reading a Cernox thermometer attached to the strain/stress cell body. The sample is placed in the cell as described above, and the leads are connected to the PCB plate next to the mounting plates; see figure 3.9A, and B for examples of the mounting in a stress and a strain cell, respectively. Details on the electronic connections and the cell fittings in the PPMS are given in section 3.7.

3.6.2 AC elastocaloric effect

The elastocaloric effect (ECE) can be defined through either the adiabatic temperature change or the isothermal entropy change, both due to applied stress/strain. ECE is the mechanical analogous of the well-known magnetocaloric effect, where the tunning parameter is the applied magnetic field. The analysis of elastocaloric properties is commonly employed in the examination of shape memory alloys, where martensitic phase transformations can be used to induce cooling. Typically, the ECE is assessed through two methods: direct and indirect measurements. In the direct approach, measurements involve rapidly applying force to a material and observing the temperature response within time frames aligned with quasiadiabatic conditions. Conversely, the indirect method, as commonly employed in literature, entails isothermally gauging the elastocaloric entropy change by meticulously determining the stress-strain relationship of a specific material. More recently, the advent of piezoelectric-based uniaxial pressure cells has popularized the use of the AC version of ECE for investigating quantum materials [58], as will be described bellow.

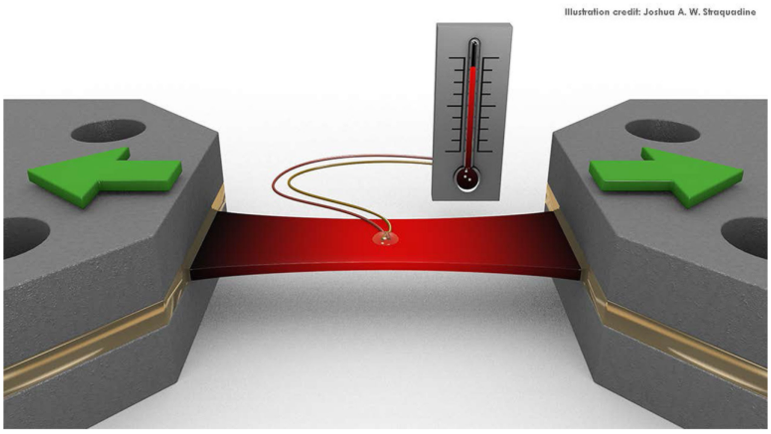

Figure 3.10: Illustration depicting the AC-ECE measurement. Figure extracted from reference [58].

Thermodynamic measurements under external conditions in which the sample must be attached to a massive body, such as hydrostatic and uniaxial pressure cells are quite challenging. Usually, this type of measurement requires the use of AC techniques, where the adiabatic (or more strictly, quasi-adiabatic) condition can be achieved by controlling the frequency of the oscillating excitation in the sample. For instance, AC calorimetry is performed by attaching a heater to the sample and applying AC power, tunning the frequency to avoid the sample falling off the adiabatic condition (see Fig. 3.6.2). The AC elastocaloric effect (AC-ECE) measurement can be used as a probe for critical degrees of freedom near phase transitions and has advantages against other AC calorimetry techniques due to its low signal-to-noise ratio and small sensibility to lattice contributions even at high temperatures [14, 16, 17]. Using uniaxial pressure cells, it is possible to apply oscillating (AC) strain/stress on top of a DC strain/stress offset and control the adiabatic condition by setting the ideal oscillation frequency. Applying uniaxial stress to a material under adiabatic condition ($dS = 0$), one can write:

$$dS = \left(\frac{dS}{dT}\right)_{\sigma} + \left(\frac{dS}{d\sigma_{ij}}\right)_{T,\sigma^1} = 0, \tag{3.11}$$

where $(dS/dT)_\sigma = C_\sigma/T$ and $(dS/d\sigma_{ij})_{T,\sigma^1} = \alpha_{ij}$. C_σ is the heat capacity at constant stress, T is the temperature, and α_{ij} is the thermal expansion coefficient. The index in σ^1 means that all the stress components are kept constant except for one. Since strain and stress are related by $\sigma_{ij} = C_{ijkl}\varepsilon_{kl}$, the elastocaloric change in temperature can be written as a function of different thermodynamic quantities.

$$dT = -\frac{T}{C_\sigma}\alpha_{ij}C_{ijkl}d\varepsilon_{kl}. \tag{3.12}$$

Now, C_{ijkl} is the elastic stiffness tensor.

This approximation requires the adiabatic condition to be fulfilled since the sample is not completely thermally isolated due to its mechanical coupling to the cell body. A quasi-adiabatic condition can be achieved by measuring the sample's thermal transfer function (TTF). This can be done by varying the strain frequency and measuring the amplified voltage signal in the thermocouple. This procedure will determine the regime in which the AC strain frequency is higher than the inverse of the relaxation time, which defines the heat exchange between the sample and its environment, and lower than the timescale, which promotes the decoupling between the sample and the thermometer.

A discretized thermal model can be used to qualitatively and semiquantitative understand the thermal experiment. Different models for the AC elastocaloric effect were proposed by M. S. Ikeda *et al.*, in [14]. Here, we briefly introduce the simplest model proposed, and for detailed review, one can look at [14]. Consider a sample with heat capacity C_S connected to the thermal bath with temperature T_B, with a path with thermal conductance K_i. A thermometer (with a heat capacity C_θ) is attached to the sample with a thermal path K_θ. From these quantities, one can define the characteristics time constants for the heat flow between the sample and the thermal bath $\tau_i = C_s/K_i$ and the heat flow between the sample and the thermometer $\tau_\theta = C_\theta/K_\theta$. Thus, for the oscillating uniaxial strain along an arbitrary direction ε_{xx}, one can write two differential equations to describe the time dependence of the sample $T_S(s)$ and thermometer $T_\theta(s)$ temperatures (a drawing of the discretized model is shown in figure 3.11A):

$$\frac{dT_s}{dt} = E_0\frac{d\varepsilon_{xx}}{dt} - (T_S - T_B)\frac{K_i}{C_S} - (T_S - T_\theta)\frac{K_\theta}{C_S}, \tag{3.13}$$

$$\frac{dT_\theta}{dt} = -(T_\theta - T_S)\frac{K_\theta}{C_\theta}. \tag{3.14}$$

Where, $E_0 = dT/d\varepsilon_{xx}$ (the elastocaloric signal!). Therefore, to introduce the elastocaloric effect one might consider:

$$T_S(t) = T_{S,0} + E_0\varepsilon_{xx}(t), \tag{3.15}$$

with $\varepsilon_{xx}(t) = \varepsilon_{xx,0}\sin(\omega t)$. This means that, in the absence of an oscillatory strain $\varepsilon_{xx}(t) = 0$, all temperatures tend toward T_B. Solving this equation for T_θ, which is the thermometer temperature measured in the experiment, one obtains:

$$T_\theta = T_B + \frac{E_0\varepsilon_{xx,0}}{\sqrt{a^2+b^2}}\sin(\omega t + \phi). \tag{3.16}$$

Where,

$$\phi = \arctan\left(\frac{a}{b}\right),$$

$$a = \frac{1}{\omega\tau_i} - \omega\tau_\theta,$$

and,

$$b = 1 + \frac{C_\theta}{C_S} + \frac{\tau_\theta}{\tau_i}.$$

The expected amplitude of the TTF is $E = E_0/\sqrt{a^2+b^2}$ and it will depend on the sample and thermocouple physical parameters, as well as, the oscilating strain frequency. In an ideal experiment $E/E_0 = 1$. In this case, the phase ϕ must reach zero (or 180°) around the region where E/E_0 plateaus. It is evident that the width of the plateau is determined by two time constants: that of the thermometer and the internal thermalization of the sample, denoted as τ_θ and τ_i respectively. Ideally, the condition $\tau_i > 100 \cdot \tau_\theta$ should be met for a reasonably wide plateau [14]. The maximum value of E/E_0 is determined by $b^{-1} = (1 + \frac{C_\theta}{C_S} + \frac{\tau_\theta}{\tau_i})^{-1}$. Hence, in addition to a small ratio $\frac{\tau_\theta}{\tau_i}$, a small ratio of heat capacities $\frac{C_\theta}{C_S}$ is required to ensure that the maximum of E/E_0 is approximately 1. This model is useful to determine the experimental conditions to achieve good results in AC-ECE measurements. For example, determining the appropriated thermocouple and its dimensions is important, and it will influence the C_θ and τ_θ in the model, which in turn will be reflected in width of the plateau. An example of a TTF (upper panel) and the phase between the components in the lock-in (bottom panel) is shown in figure 3.11B. As one can see, there is a plateau region in the normalized signal versus frequency, and this region is utilized to perform the experiments.

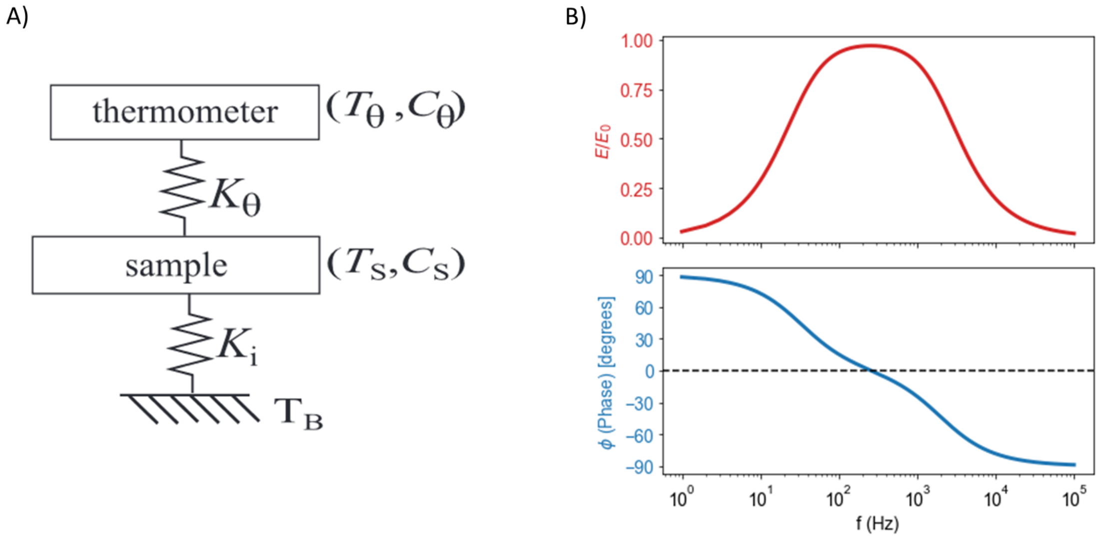

Figure 3.11: (A) Schematics of the discretized thermal model, figure adapted from reference [14]. (B) Example of the normalized AC-ECE signal (upper panel) and phase (bottom panel).

The elastocaloric signal is generated by applying an AC voltage to the inner stack of the Piezo actuators $V_{inner} = V_0 \sin(\omega t)$ and measured using the Chromel-$AuFe_{0.07\%}$ thermocouple attached to the sample with Stycast 2850FT (Figure 3.12A). If needed, the resistance can be measured simultaneously by attaching the leads on top of the sample, as described in the last section. The Stanford Research SR554 transformer preamplifier first amplifies the thermocouple voltage, and the Stanford lock-in amplifier SR860 is used to detect the signal and record it as temperature sweeps are performed. The cell outer stacks are used to apply DC strain/stress to the sample using a DC voltage source. A simplified drawing of the measurement is shown in 3.12B.

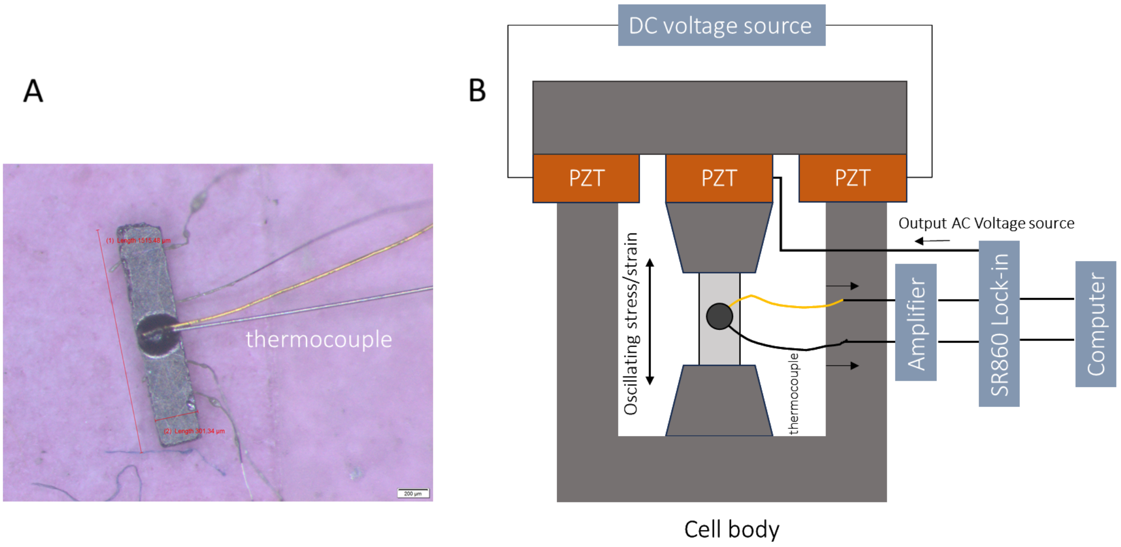

Figure 3.12: Sample prepared for simultaneous resistance and AC-ECE measurements, showing the thermocouple attached to the sample with Stycast (A). Schematics of the AC-ECE measurement method (B).

3.7 PPMS and strain/stress cells fitting

For the aforementioned measurements, the cells were integrated into a Quantum Design Physical Property Measurement System (PPMS) using the Razorbill PPMS Probe kit alongside the Modified P450 Probe, as illustrated in figure 3.13. Within the sample configuration, the voltage leads or the thermocouple are soldered to a PCB wiring platform, which is subsequently connected to the modified PPMS puck affixed to the bottom of the probe (refer to figure 3.14 for an expanded schematic of the wiring platform). This configuration enables simultaneous measurement, if required, of resistivity and the AC-ECE through the PPMS electronics. The DC voltage source and the capacitance bridge are linked via high-voltage wires and coaxial cables at the top of the probe, serving to drive the PZT stacks and measure capacitance.

The PPMS electronics feature 3 channels with 4-wiring connections, routed to a breakout box and segmented into various equipment, as depicted in figure 3.15. Users can designate a channel for resistivity measurement, another for thermocouple voltage leads, and a third for the thermometer attached to the cell body.

The DC voltage applied to the PZT stacks was regulated using a dual-channel Keithley 2064B sourcemeter, while capacitance was gauged via the high-precision capacitance bridge AH2700A. This apparatus is indispensable for controlling the cell and assessing the applied force or strain on the sample. Temperature measurement can be conducted utilizing either the auxiliary connection of the resistance bridge or separately, employing a dedicated temperature controller bridge. The data acquisition and cell operation can be performed using scripts in different programming languages (e.g., Python, LABview etc.).

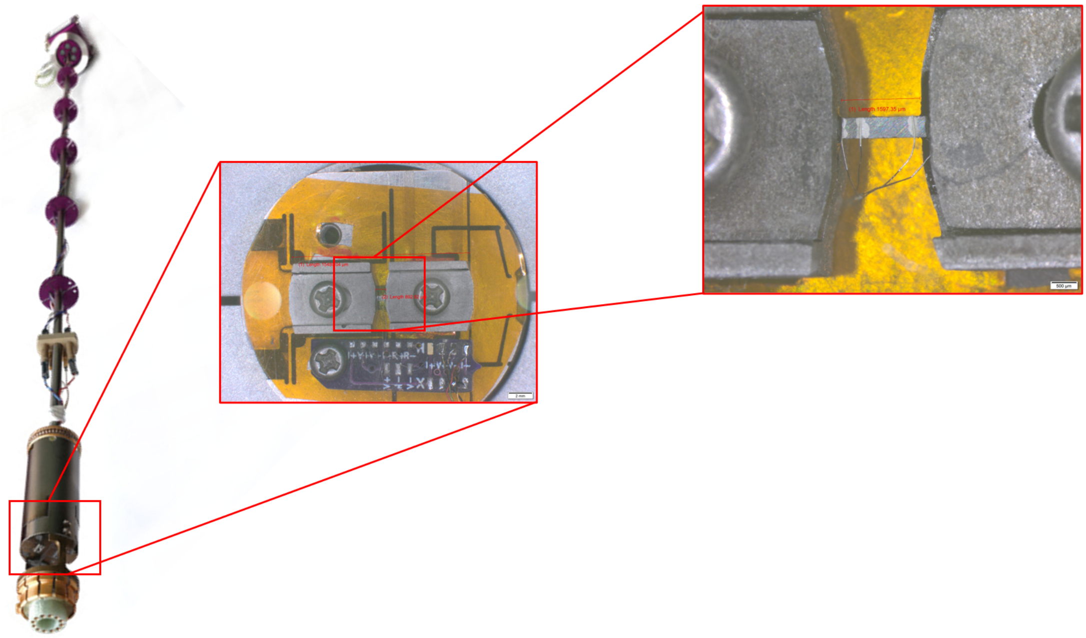

Figure 3.13: Example of a Razorbill PPMS probe with a FC100 cell attached to the end (this image was extracted from the Razorbill website). The zoomed regions show the sample mounted in the FC100 cell.

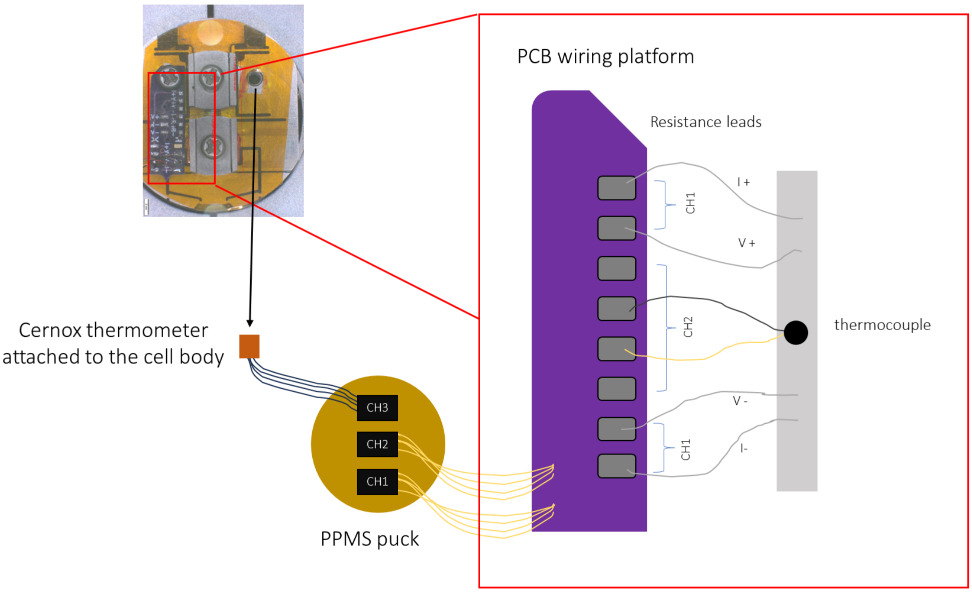

Figure 3.14: Schematics of the wiring platform suitable for Resistivity and AC-ECE measurements. This wiring platform was designed by the co-advisor Sean M. Thomas.

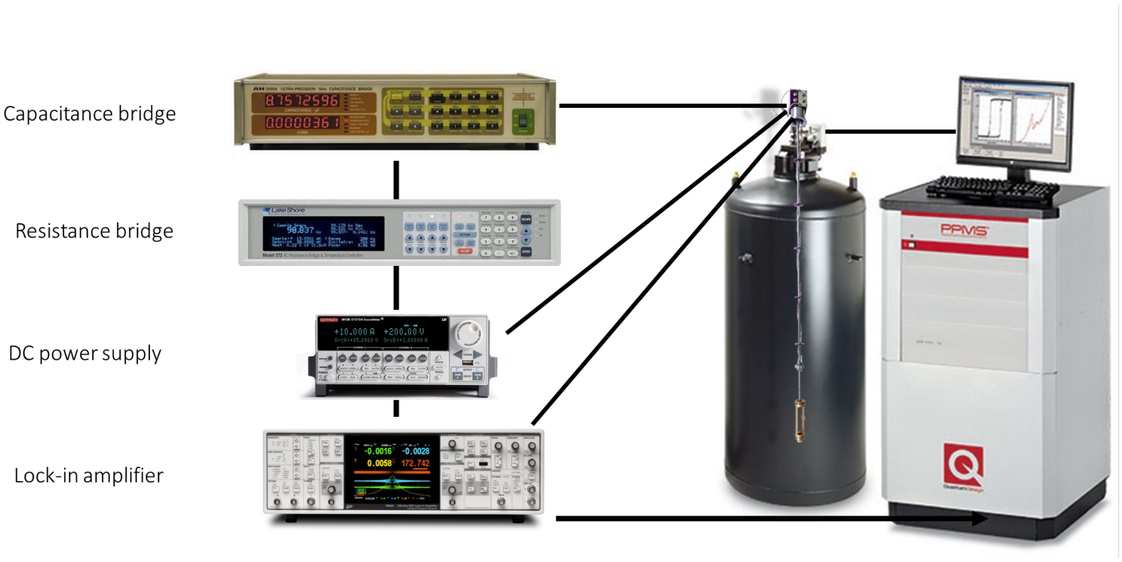

Figure 3.15: Schematics of the attached external equipment to a PPMS cryostat (the picture of the PPMS cryostat was extracted from the QD's web site and adapted to create this figure).

Chapter 4

Uniaxial pressure effect on superconducting and charge density wave transitions in $La_3Co_4Sn_{13}$

4.1 Introduction

The Remeika family $R_3M_4Sn_{13}$ (R = Rare earth/Alkaline metals, M = Transition metal) has been extensively studied in the literature due to the wide variety of interesting physical properties, including strong electronic correlation [18, 48], superconductivity [49], structural/CDW transitions [50]. Particularly, charge density waves and superconductivity are often observed in this family, such as in $(Sr,Ca)_3(Rh,Ir)_4Sn_{13}$, where anomalies related to the CDW can be seen in electrical resistivity, magnetic susceptibility, and single-crystal x-ray diffraction (SGXRD) [59, 60, 2]. Interestingly, the CDW phase can be suppressed by increasing Ca doping and/or hydrostatic pressure while the superconducting state is enhanced, leading to a quantum critical point at $T_{CDW} = 0$. However, the role of charge ordering in the stabilization of the superconductivity of these compounds remains in debate. The compound studied in this work is the $La_3Co_4Sn_{13}$ which crystallizes in a cubic structure with the space group $Pm-3n$ with lattice parameters $a = 9.64$ Å, and

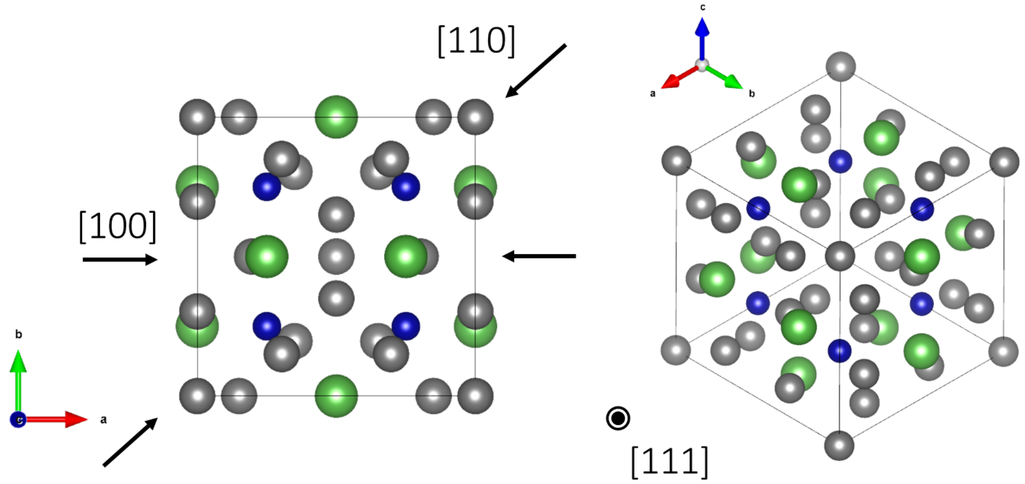

Figure 4.1: $La_3Co_4Sn_{13}$ crystal structure showing the high symmetry crystallographic directions.

undergoes a structural/CDW transition at $T_{CDW} \sim 147$ K, with a superconducting state emerging at $T_c \sim 2.7$ K [61]. Similarly to $(Sr,Ca)_3(Rh,Ir)_4Sn_{13}$, below the CDW transition, the lattice parameters have double its values with respect to the high-temperature phase, with a propagation vector of $\mathbf{q_{CDW}} = (0.5\ 0.5\ 0)$. Moreover, phonon spectra calculations revealed a softening and imaginary frequency branch in the low-temperature phase at the $\mathbf{M} = (0.5\,0.5\,0)$ point, coinciding with the observed propagation vector, indicating structural instability [62]. In our previous study of this compound, we observed a linear increase of T_c with hydrostatic pressure. At the same time, the CDW transition is suppressed, similar to its isostructural analogous $(Sr,Ca)_3(Rh,Ir)_4Sn_{13}$. The total suppression of CDW is placed around $P = 3.4$ GPa, where the superlattice peaks are no longer observed in low-temperature X-ray diffraction [3]. X-ray absorption sutudies using linear polarized light in $Sr_3Ir_4Sn_{13}$, performed with the polarization perpendicular and parallel to the [110] direction (CDW wave vector direction) have shown that there is a significant anisotropy in the electronic structure of the material [63]. This anisotropy was suggested to play important role in the anomaly observed in the electrical resistivity. This observation was one of the main motivations to study the effect of uniaxial pressure in $La_3Co_4Sn_{13}$, since the same kind of anisotropy is expected due to the shared similarities with $(Sr,Ca)_3(Rh,Ir)_4Sn_{13}$.

In order to explore the possible anisotropic response of the CDW and its relation with the superconductivity we perform electrical resistivity measurements under uniaxial stress along the high symmetry crystallographic directions [100], [110] and [111] in the cubic compound $La_3Co_4Sn_{13}$(see figure 4.1). Additionally, to unveil a possible domain physics along the CDW propagation vector direction [110] we use AC-ECE effect measurements.

4.2 Experimental results

4.2.1 Electrical resistivity

In temperature-dependent resistivity measurements the superconducting and charge density wave have characteristic features around their transition temperatures. One property of the material upon entering the superconducting state is the zero resistance below T_c. On the other hand, the CDW transition in most of the materials is characterized by an increase of the resistance at T_{CDW} due to changes in the electronic structure and scattering rates. In order to evaluate the effects of uniaxial pressure on the CDW and superconducting transition in $La_3Co_4Sn_{13}$, electrical resistivity measurements were performed with uniaxial stress applied along different high symmetry crystallographic directions [100], [110], and [111]. For all measurements, the excitation electrical current is along the same direction of applied stress. First, we show our resistivity *versus* temperature curves around the superconducting transition for different pressures, along the chosen crystallographic directions. Figure 4.2 shows the electrical resistivity curves around the superconducting transition for various applied stress along the [100] direction. The black arrow indicates the direction of the increasing stress. As one can observe, T_c decreases upon applying compressive stress, which is in contrast to the hydrostatic pressure case, where it increases [3]. The transition temperature were determined using the mid point of the resistance drop. Interestingly, for pressures applied along the [110] and [111] directions, the superconductivity is also suppressed. The curves around the T_c for [110] and [111] are depicted in figures 4.3 and 4.4, respectively. To compare the rates at which the transitions are suppressed, the superconducting temperature transitions were plotted as a function of pressure for each measured direction. Figure 4.5 illustrates the pressure *versus* normalized temperature phase diagram for the superconducting transition of $La_3Co_4Sn_{13}$ at different crystallographic directions. Normalizing T_c by its value at $\sigma = 0$ GPa provides a clearer visualization of the differences in suppression rates $dT_c/d\sigma_{[hkl]}$. Importantly, $dT_c/d\sigma_{[hkl]}$ was found to vary among the directions. Specifically, T_c is suppressed faster for pressure along the [100] direction with $dT_c/d\sigma_{[100]}$ = -0.23 K/GPa, and it remains almost unchanged along [111] with $dT_c/d\sigma_{[111]}$ = -0.04 K/GPa, while the [110] direction takes an intermediate value with $dT_c/d\sigma_{[110]}$ = -0.14 K/GPa. For the later, two samples were measured and the same suppresion rate was obtained, different samples are labeled as open triangles (S1) and closed diamonds (S2). For both samples, the measurements were taken around the CDW and superconducting transition as will be shown below. The obtained $dT_c/d\sigma_{[hkl]}$ from the linear fits in Figure 4.5, are summarized in table 4.1.

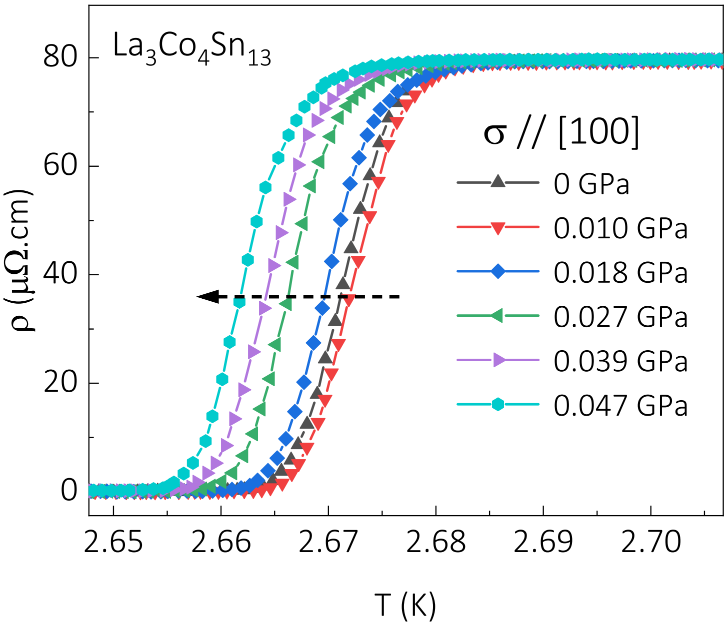

Figure 4.2: Resistivity measurements around the superconducting transition at different compressive stress values along [100].

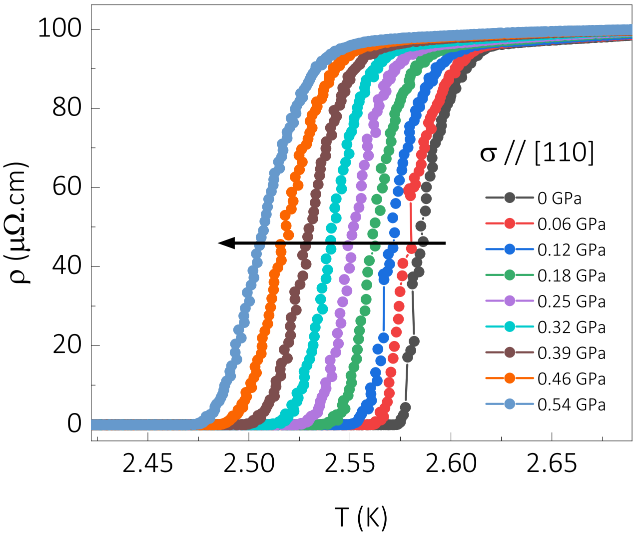

Figure 4.3: Resistivity measurements around the superconducting transition at different compressive stress values along [110].

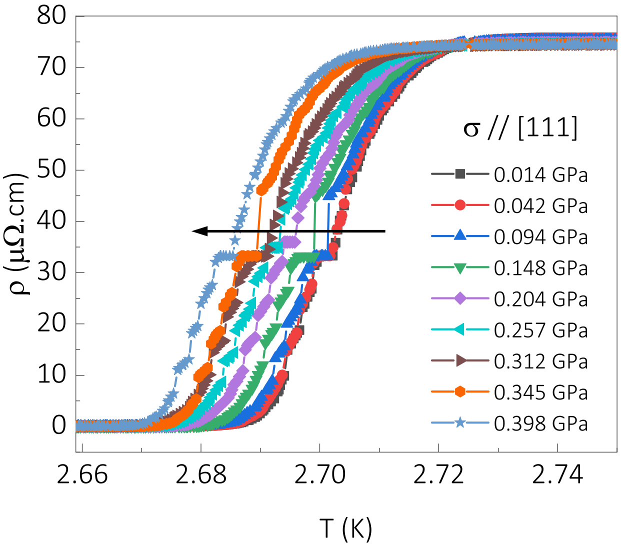

Figure 4.4: Resistivity measurements around the superconducting transition at different compressive stress values along [111].

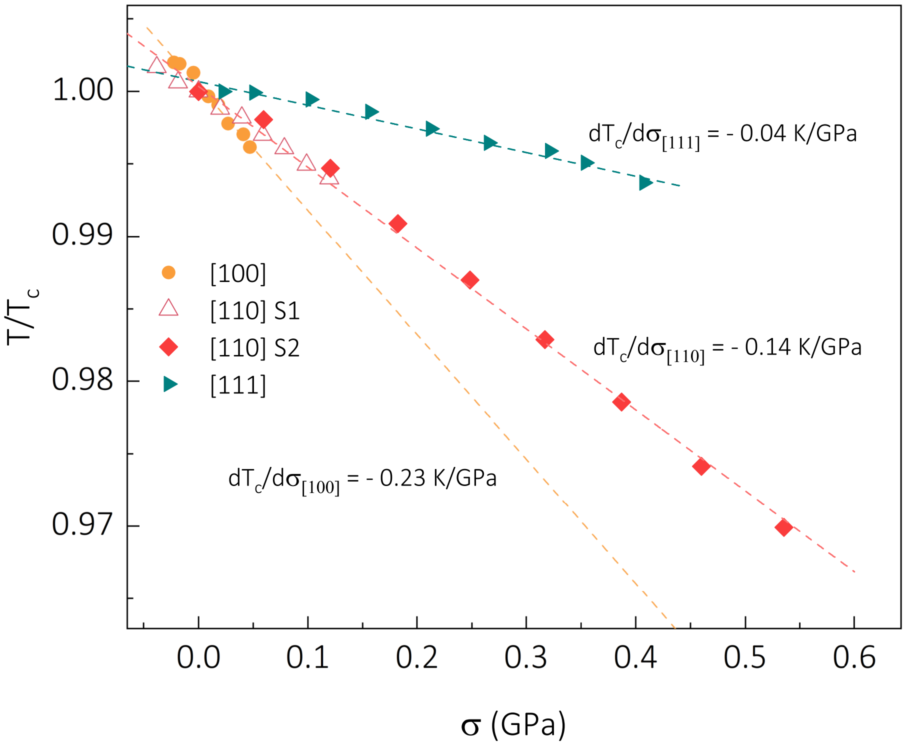

Figure 4.5: Phase diagram $T_c \times \sigma$ comparing the suppression of the superconducting transition for stress applied along different crystallographic directions. For the [110] direction, two samples were measured. Since the suppression rate observed for both samples was the same, both data were used to perform the linear fit.

Direction	$dT_c/d\sigma_{[hkl]}$ K/GPa
[100]	-0.23
[110]	-0.14
[111]	-0.04

Table 4.1: Summary table of the superconducting transition suppression rate for pressure applied along different directions.

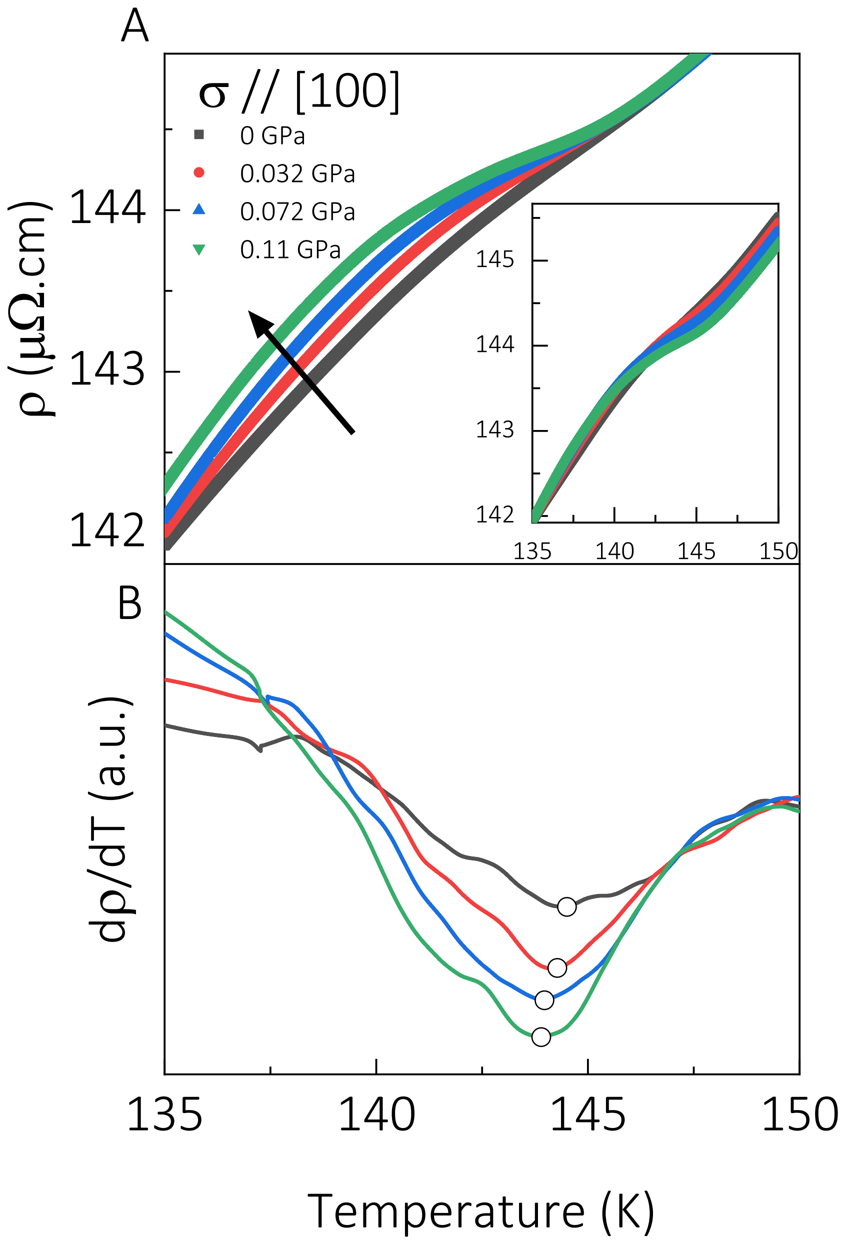

Figure 4.6: (a) temperature-dependent resistivity measurement for many applied uniaxial stress along the [100] direction. (b) Derivatives of the resistivity curves of panel (a). Both panels share the same temperature scale to facilitate the visualization of the features.

To establish a possible correlation between the observed superconductivity behavior under uniaxial stress, resistivity measurements were conducted around the CDW transition in the same samples. The measurements along the [100] direction around the CDW transition are depicted in figure 4.6A, with their corresponding derivatives in the lower panel B. Along this direction, a noticeable increase in the electrical resistivity jump is evident within the stress range of 0–0.11 GPa, while the temperature transition T_{CDW} appears to remain almost temperature-independent. To aid visualization of the pressure-dependent jump increase, the $\rho \times T$ curves for non-zero pressures were adjusted to align with the resistivity above the CDW transition at zero pressure, as illustrated in the inset of figure 4.6A. The determination of T_{CDW} was based on the peak-dip observed in the derivatives shown in figure 4.6B (open circles). This rise in resistivity at the CDW transition is commonly associated with a decrease in the density of states (DOS) of the Fermi surface due to the opening of the CDW gap. ^{59}Co Nuclear Magnetic Resonance (NMR) findings unveiled a 7.7% reduction in the Co-3d density of states across the CDW phase transition in this compound [62]. This minor reduction suggests that certain segments of the Fermi surface become gapped for $T < T_{CDW}$. Consequently, the heightened jump could be linked to the reinforcement of the CDW gap along this direction, potentially elucidating the decrease in the superconducting transition temperature owing to its dependence on the density of states. According to conventional BCS superconductors, $T_c \propto \hbar\omega_c e^{-\frac{1}{N(E_F)V_{eff}}}$ (equation 2.21), where $N(E_F)$, V_{eff}, and ω_c respectively denote the density of states at the Fermi level, the effective attractive electron coupling, and the Debye phonon frequency. However, pressure may influence other factors in this equation, such as the electron-electron effective coupling and the phonon frequency, as will be discussed later.

The resistivity curves plotted against temperature for measurements conducted with uniaxial stress applied along the [110] direction are depicted in Figure 4.7A-D. In panel A, the curves illustrate various applied pressures for the sample 1 (S1) and its corresponding derivatives in Figure 4.7C. When measuring along the [110] direction, the resistivity curve manifests the CDW transition as a broader feature, which gradually narrows with increasing pressure. At $\sigma = 0$ GPa, the CDW transition initiates at $T_{CDW} = 145$ K, evidenced by the rise in resistivity. Subsequently, the curve maintains metallic characteristics, with a slight drop in resistivity occurring around $T = 125$ K. With rising pressure, the CDW transition is suppressed, yet the anomaly appears to sharpen, tending towards a singular jump. This distinct characteristic is more pronounced in the derivative curves (Fig. 4.7C). To validate this peculiar behavior of the resistivity anomaly around T_{CDW} and exclude possible sample-dependent factors, a second sample (S2) was examined, and its resistivity curves along with their derivatives are presented in figures 4.7B and D, respectively. The observed qualitative behavior remains consistent for the second sample. The CDW transition temperature T_{CDW} at zero pressure aligns with that of S1. It is intriguing to note that these distinctive characteristics are observed along the same axis as the CDW wave vector $\mathbf{q}_{CDW} = (0.5\ 0.5\ 0)$ within this material.

One potential explanation for the broadening of this feature, which narrows under increased pressure, could be attributed to the presence of diverse CDW domains. In this cubic compound, the commensurate CDW can, in principle, generate distinct twin domains. Due to the symmetry of the structure, a $\mathbf{q}_{CDW} = (0.5\ 0.5\ 0)$ wave vector may give rise to varied domains within the crystal along equivalent crystallographic directions without a preferred orientation. Since the measurements are conducted with the current flowing along the same direction as the applied stress and $\mathbf{q}_{CDW}$, it renders the resistivity measurements more sensitive, at least, to variations in electron scattering due to the domain distribution along this direction.

To elucidate the broad feature along this direction, where the transition initiates with an increase in resistivity at T_{CDW} and further declines at lower temperatures, one could consider that as the CDW phase begins to form, domain distribution within the material takes place. The population of domains at different equivalent directions contributes to the scattering rate as the temperature decreases. Hence, it's plausible that the CDW domain distribution reaches completion at $T = 125$ K, corresponding to the slight drop in resistivity. However, for the stressed sample along the [110] direction, the domain population tends to adopt the most energetically favorable configuration. As the sample cools under stress, the anomaly in resistivity at T_{CDW} becomes narrower because the degeneracy in domain distribution is lifted, leading the domains to preferentially align along specific directions. Figure 4.8 shows an schematic example of a sample cooled under zero stress and a sample cooled stressed along the [110] direction. The behavior of ferromagnetic domains offers a compelling analogy for understanding the dynamics of CDW do-

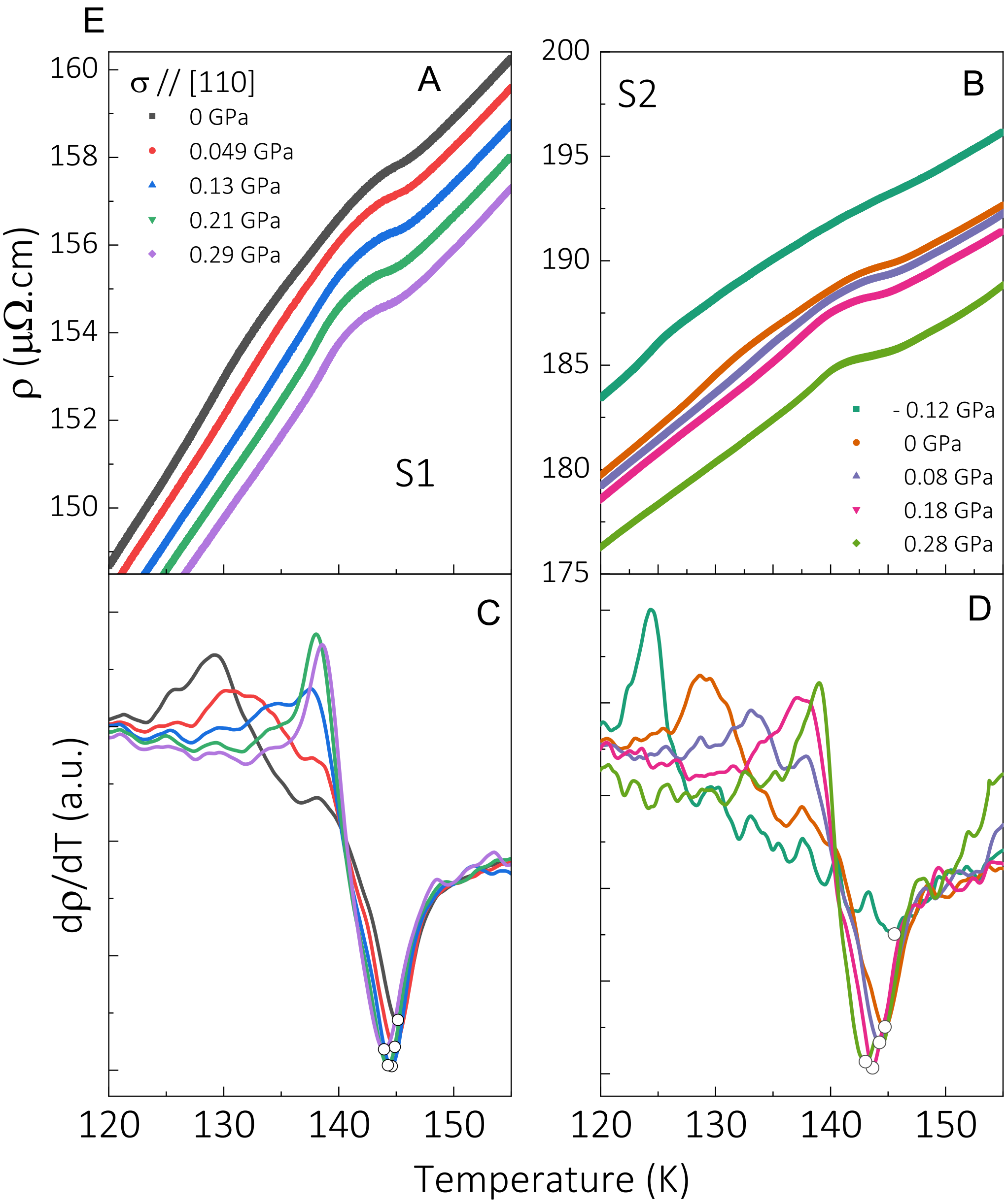

Figure 4.7: temperature-dependent resistivity measurement for many applied uniaxial stress along the [110] direction for sample 1 (A) and sample 2 (B). Derivatives of the resistivity curves of the upper panels for sample 1 and 3, respectively (C, and D).

mains in materials. In ferromagnetic systems, the alignment of magnetic domains under an applied magnetic field is a familiar phenomenon. When a ferromagnetic material is field cooled, at the transition temperature it will tend to form a single domain aligned with the applied magnetic field direction. In a similar manner, our resistivity curves were taken with the material being ”stress-cooled”, therefore, the domains will preferentially take the most favorable direction constrained by the uniaxial stress as an external stimuli. A similar behavior is observed in the La-based cuprates with stripe CDW orders [64], in such case, the system has a $C4$ symmetry, where two possible domain degeneracy can be observed, with domains aligned along the a, or b axis. As the material is strained along one of the directions (a or b) the degeneracy of the in-plane striped CDW domains is lifted, and the domains align along a preferential direction, with the propagation vector perpendicular the direction of applied strain.

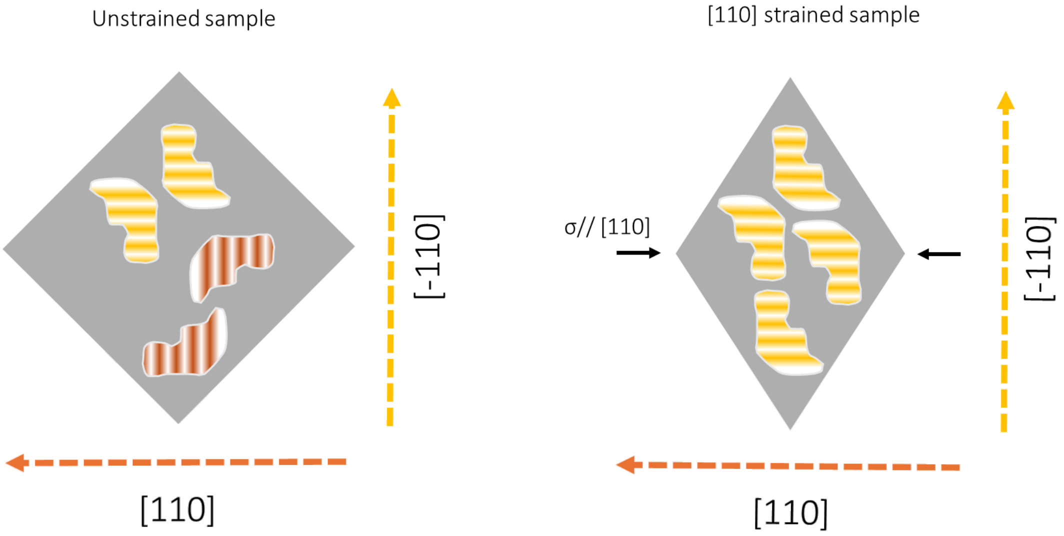

Figure 4.8: Schematics of a possible CDW domain distribution related to the $\mathbf{q}_{CDW}$ = (0.5 0.5 0) for a cubic material. In the left panel, the material is unstressed-cooled, giving rise to an equally distributed domain configuration along the equivalent directions [hh0]. In the right panel, the material is cooled under uniaxial stress along the [110] direction, favoring the domain distribution to be aligned.

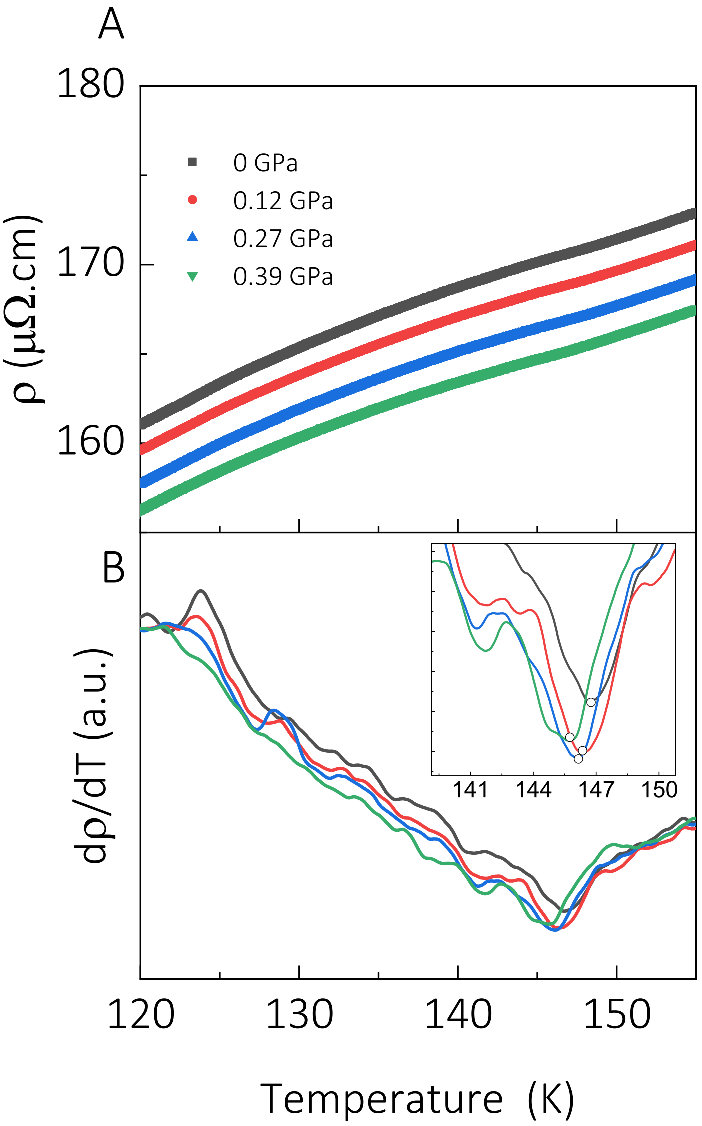

Figure 4.9: (A) temperature-dependent resistivity measurement for many applied uniaxial stress along the [111] direction (B) Derivatives of the resistivity curves of panel A. Both panels share the same temperature scale to facilitate the visualization of the features.

Now, we direct our attention to the stress applied along the [111] direction. Similar to the procedures followed for the [100] and [110] orientations, measurements were conducted on a bar-shaped sample that was carefully aligned and polished with its length oriented along the [111] direction. The electrical current flows parallel to the direction of stress application. The resistivity curves around the CDW transition are illustrated in figure 4.9A, alongside their corresponding derivatives in B. A notable observation regarding pressures exerted along this direction is that, in contrast to CDW measurements along [110], the transition feature appears weaker even at zero applied pressure, and the variation of T_{CDW} demonstrates less sensitivity to pressure compared to compression along the [110] direction. In the derivative curves $d\rho_{[111]}/dT$, the T_{CDW} feature presents as a shallow peak-dip, distinguishing it from the sharper features observed in $d\rho_{[100]}/dT$ and $d\rho_{[110]}/dT$ curves.

As observed before, the onset of the CDW transition in resistivity measurements is usually marked by an upturn in the $\rho \times T$ curves, which is usually correlated to the opening of the CDW gap in the electronic band structure. Therefore, the relative size of the upturn anomaly is roughly related to the CDW gap. In order to gain insights on how the uniaxial pressure affects the CDW gap, the relative size of the upturn was estimated for all $\rho \times T$ curves at each uniaxial stress direction. The method used for the estimation is shown in figure 4.10A. A linear fit was performed at the linear region of the $\rho \times T$ above the CDW transition (red dashed line in fig. 4.10A). The fit was shifted to match the tangent point of the maximum in resistivity during the transition (blue dashed line in fig. 4.10A). The jump size $\Delta\rho$ was defined as the distance between the lower red dashed line fit and the upper blue dashed line at $T = T_{CDW}$. The values of T_{CDW} used were the ones obtained from the peak dip of the derivative curves in figures 4.6B, 4.7(C,D), and 4.9B. In figure 4.10B the pressure evolution of $\Delta\rho$ is given. The values obtained from the method in 4.10A were normalized by the resistivity value at T_{CDW} in order to mitigate effects of different resistivity values between the samples. The values are plotted as a ratio between the $\Delta\rho/\rho_{T_{CDW}}$ and $[\Delta\rho/\rho_{T_{CDW}}]_{0\ \mathrm{GPa}}$ at zero pressure. Also, the non-normalized relative jump $\Delta\rho/\rho_{TCDW}$ is shown in panel C. From 4.10B, it is clear that the upturn increases more rapidly for uniaxial stress along the [100] direction than the other directions. Again, $\Delta\rho/\rho$ as function of pressure along [110] direction was estimated for S1 and S2 and it is noteworthy that, like $dT_c/d\sigma_{[110]}$, they roughly

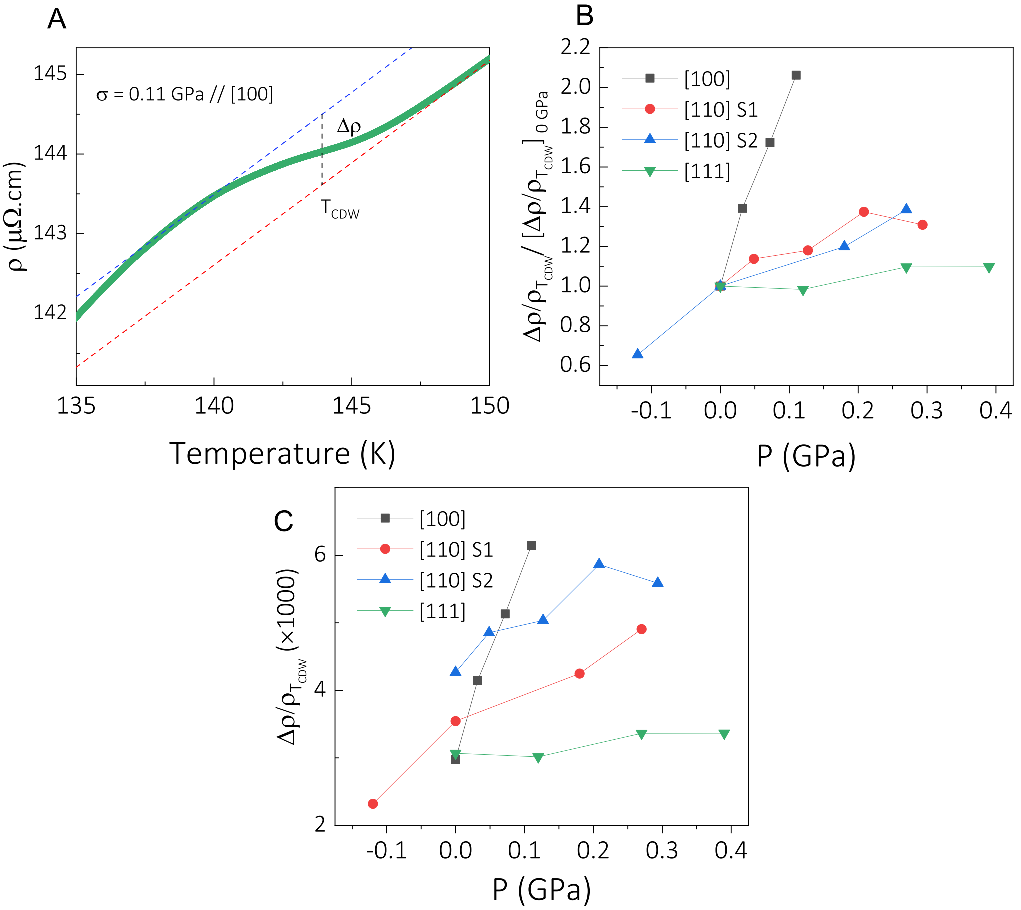

Figure 4.10: Protocol used to determine the upturn relative size $\Delta\rho$ at T_{CDW} (A). Pressure evolution of the relative jump size $\Delta\rho$ normalized by the value of resistivity at T_{CDW} divided by its value at zero pressure (B) Non-normalized ratio curves (C).

share the same increasing rate as a function of pressure, which builds confidence in the data.

To understand how the observed results are connected to the elastic properties of the material one can make use of the relation between the elastic constants for materials in the Remeika family (3-4-13). In the literature the elastic constants for $Yb_3Rh_4Sn_{13}$ and $Ca_3Rh_4Sn_{13}$ were determined from measurements of sound velocity and ultrasonic attenuation [65]. The values obtained are shown in the table 4.2 below. Although the exact values of the elastic constants cannot be used directly

Elastic constant	$Yb_3Rh_4Sn_{13}$	$Ca_3Rh_4Sn_{13}$
C_{11} (GPa)	126.2	139.1
C_{12} (GPa)	67.7	73.3
C_{44} (GPa)	20.5	18.86

Table 4.2: Elastic constants obtained for two members of the Remeika family $Yb_3Rh_4Sn_{13}$ and $Ca_3Rh_4Sn_{13}$ [65].

for the studied compound $La_3Co_4Sn_{13}$, one can use this values make the following assumptions about the compounds in this family: The elastic constants follow the relation $C_{44} < C_{12} < C_{11}$. Moreover, the ratio between the elastic constants are roughly the same, where $C_{11} \approx 7 \times C_{44}$ and $C_{12} \approx 4 \times C_{44}$. One can use this ratios to estimate the compliance matrix elements in terms of the elastic constant C_{44} for $La_3Co_4Sn_{13}$ using the equations,

$$S_{11} = \frac{C_{11} + C_{12}}{(C_{11} - C_{12})(C_{11} + 2C_{12})}, \tag{4.1}$$

$$S_{12} = \frac{-C_{12}}{(C_{11} - C_{12})(C_{11} + 2C_{12})}, \tag{4.2}$$

$$S_{44} = \frac{1}{C_{44}}. \tag{4.3}$$

From the compliance matrix elements, we estimate the the Young's modulus anisotropy for different directions in the crystal using the relation:

$$\frac{1}{E_{hkl}} = S_{11} - 2\left[(S_{11} - S_{12}) - \frac{1}{2}S_{44}\right]\frac{h^2k^2 + k^2l^2 + l^2h^2}{(h^2 + k^2 + l^2)}. \tag{4.4}$$

Imputing the compliance elements into these equations with the condition $C_{44} < C_{12} \approx 4 \times C_{44} < C_{11} \approx 7 \times C_{44}$ reveals that the maximum value of E occurs along the [100] direction, while the minimum occurs along [111]. By utilizing the values of the ratios C_{11}/C_{44} and C_{12}/C_{44}, we model the anisotropy in the Young's modulus (E) with respect to the crystal directions [hkl].

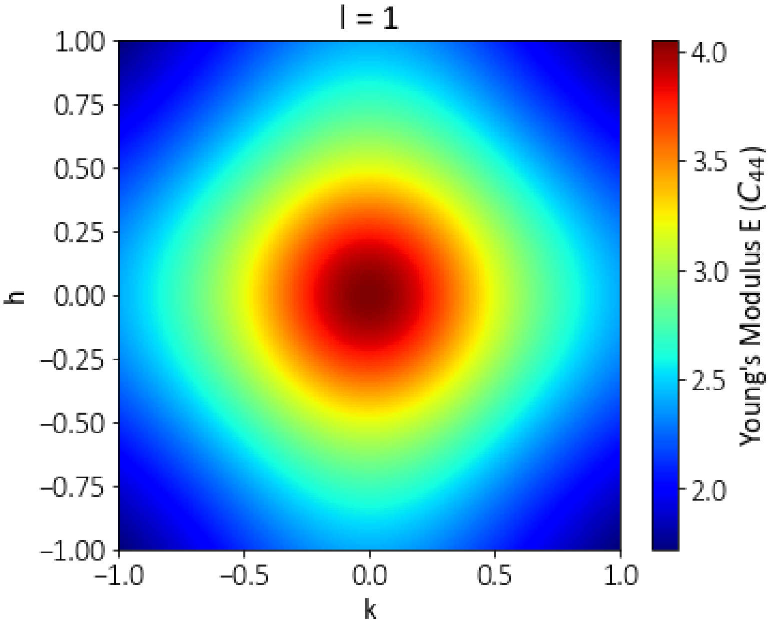

Figure 4.11: Simulated values for the Young's modulus for the [$hk1$] directions.

The results of the simulation are depicted in figure 4.11. The color map represent the values of E in terms of the elastic constant C_{44}. The axis are representative of the crystallographic directions, where h =[-1,1], k = [-1,1] and l = 1. The maximum value of E is situated at the center of the graph, specifically along the [100] direction. The minimum value achieved is at the corners, representing the [111] direction and its equivalents. Intermediate values were obtained for the [110] direction. These values are summarized in the table 4.3, given in terms of the elastic constant C_{44}. We employ these values to establish a correlation between the anisotropic mechanical properties of the material and the observed responses to uniaxial stress of the CDW and superconductivity along different crystallographic directions.

Young's modulus E serves as a metric for a material's ability to withstand changes in length when subjected to tension or compression along its length. Conse-

Direction	$\times C_{44}$
[100]	≈ 4.09
[110]	≈ 2.43
[111]	≈ 1.73

Table 4.3: Young's modulus estimated from the elastic constant ratio given in terms of the elastic constant C_{44}.

quently, a higher E indicates lesser susceptibility to changes in length due to applied mechanical stress. As previously discussed, the anisotropy of elastic constants C_{ij}, linked to microscopic properties, can render an anisotropic E, even in cubic materials. Leveraging this information, we construct a plot illustrating the suppression rates $dT_c/d\sigma_{[hkl]}$ and the enhancement rates of resistivity jump $d[\Delta\rho/\rho_{T_{CDW}}]/d\sigma_{[hkl]}$ as functions of estimated $E_{[hkl]}$ along the corresponding $[hkl]$ direction, given in terms of the C_{44} elastic constant. The results are depicted in figure 4.12A. Intriguingly, there is an ambiguous relationship between the measured rates and the material's stiffness. For stress applied along the [100] direction, the material exhibits greater stiffness, conversely displaying maximum suppression of T_c and a more rapid increase in the resistivity jump attributed to the CDW transition. Along the [111] direction, where the material is softer, the pressure dependence of T_c and $\Delta\rho$ is minimal. In figure 4.12B we show a comparison between the rate at which the CDW anomaly increases and the suppression rate of T_c. Interestingly, for higher increase of the CDW jump, which occur at the [100] direction, the superconductivity is suppressed faster. Meanwhile, for the [110] direction where the $\Delta\rho$ is almost pressure-independent, $dT_c/d\sigma_{[111]}$ is smaller.

This is an interesting result, since it suggest an anisotropic response of the CDW which is reflected in the superconductivity due to a possible competition between these two states. Moreover, the ambiguous results obtained in the analysis of the anisotropy in the Young's modulus, may suggest that the coupling of the phase transitions with the lattices degrees of freedom are likely smaller. In general, applying external pressure to superconductors can influence their behavior by altering key parameters governing their superconducting properties, including the electronic density of states at the Fermi energy, the characteristic phonon frequency, and the coupling constant between electrons and phonons [66]. This can effectively adjust

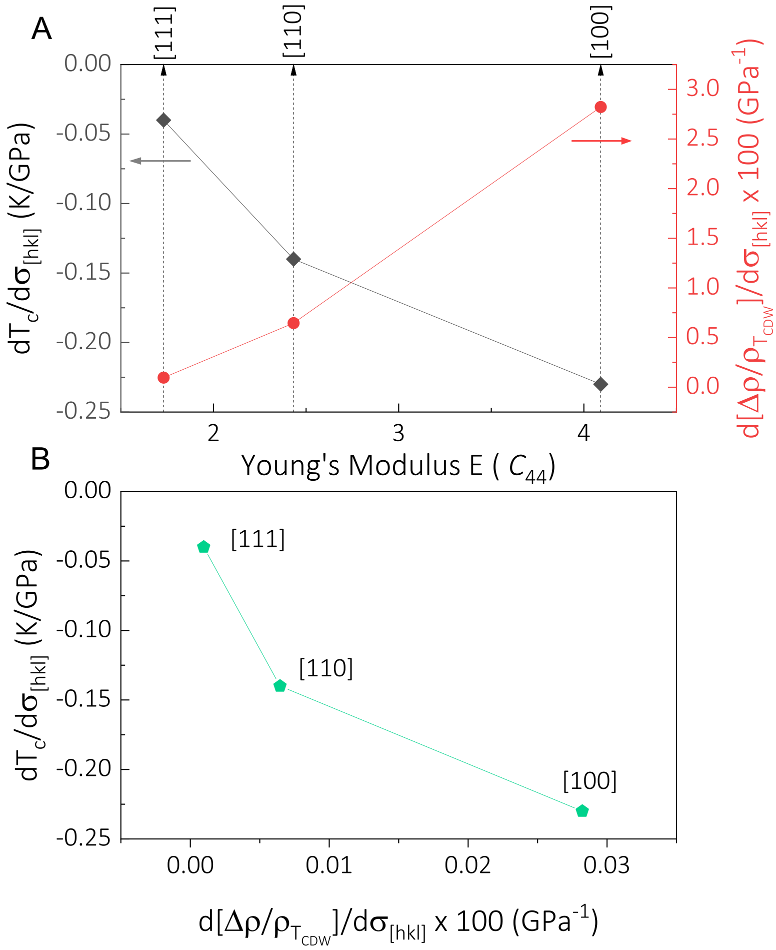

Figure 4.12: (A) Suppresion rate of T_c for different crystalographic directions (left) and rate of enhancement of the CDW upturn (right) plotted as a function of the estimated Young's modulus for each direction. (B) Correlation between the T_c suppresion rate and the rate of enhancement of the CDW upturn.

the critical temperature and other superconducting characteristics. It's noteworthy that most metallic superconducting elements exhibit a reduction in T_c under pressure. This decline in T_c is commonly attributed to the volume-dependent nature of $N(E_F)$ and the effective electron-electron interaction mediated by electron-phonon coupling. Looking back to the BCS equation for the superconducting transition temperature, $k_B T_c \approx 1.13\hbar\omega_c e^{-\frac{1}{N(E_F)V}}$, ω_c commonly increases with pressure, which is called phonon hardening, which would enhance T_c. Therefore, the decrease of T_c with pressure, is attributed to the parameter $\lambda = N(E_F)V$. Therefore, the anisotropic pressure dependence observed for T_c is likely related to anisotropic changes in the electron-phonon coupling and/or density of states.

4.2.2 AC-Elastocaloric effect

In order to explore in more details the possible domain physics observed in resistivity measurements under uniaxial stress along the [110] direction we perform AC Elastocaloric effect measurements under uniaxial strain. AC-ECE measurements have been used lately as a thermodynamic probe of the entropic landscape in the temperature-strain space [15, 14, 16, 17]. There have been evidence that the AC-ECE signal is sensible to realignment of the CDW wave vector in rare-earth tellurides such as $ErTe_3$ and $SmTe_3$ [15]. AC-ECE was also used to unravel domain physics in the DyB_2C_2 antiferroquadrupolar order [16]. Here we made use of the AC-ECE measurements to gain insights on the uniaxial pressure effect on the thermodynamics of the CDW transition. Specifically, we perform measurements under uniaxial strain along the [110] direction, where the broadening of the transition was observed. As mentioned in the section above, the broadening observed in $\rho \times T$ curves, which gets narrow with applied stress, might be related to the existence of different CDW domains degenerated with the same $\mathbf{q}_{CDW} = (0.5\ 0.5\ 0)$ wave vector. In figure 4.13A, we show the AC-ECE measurements as a function of temperature around the CDW transition at different applied strains. In figure 4.13B, their respective derivatives are shown in the same scale in temperature. When working with strain instead of stress, negative values means compression. As the transition temperature is approached the elastocaloric signal sudden increases, and an anomaly resembling the heat capacity jump-like feature is observed. The peak dip in the derivatives in

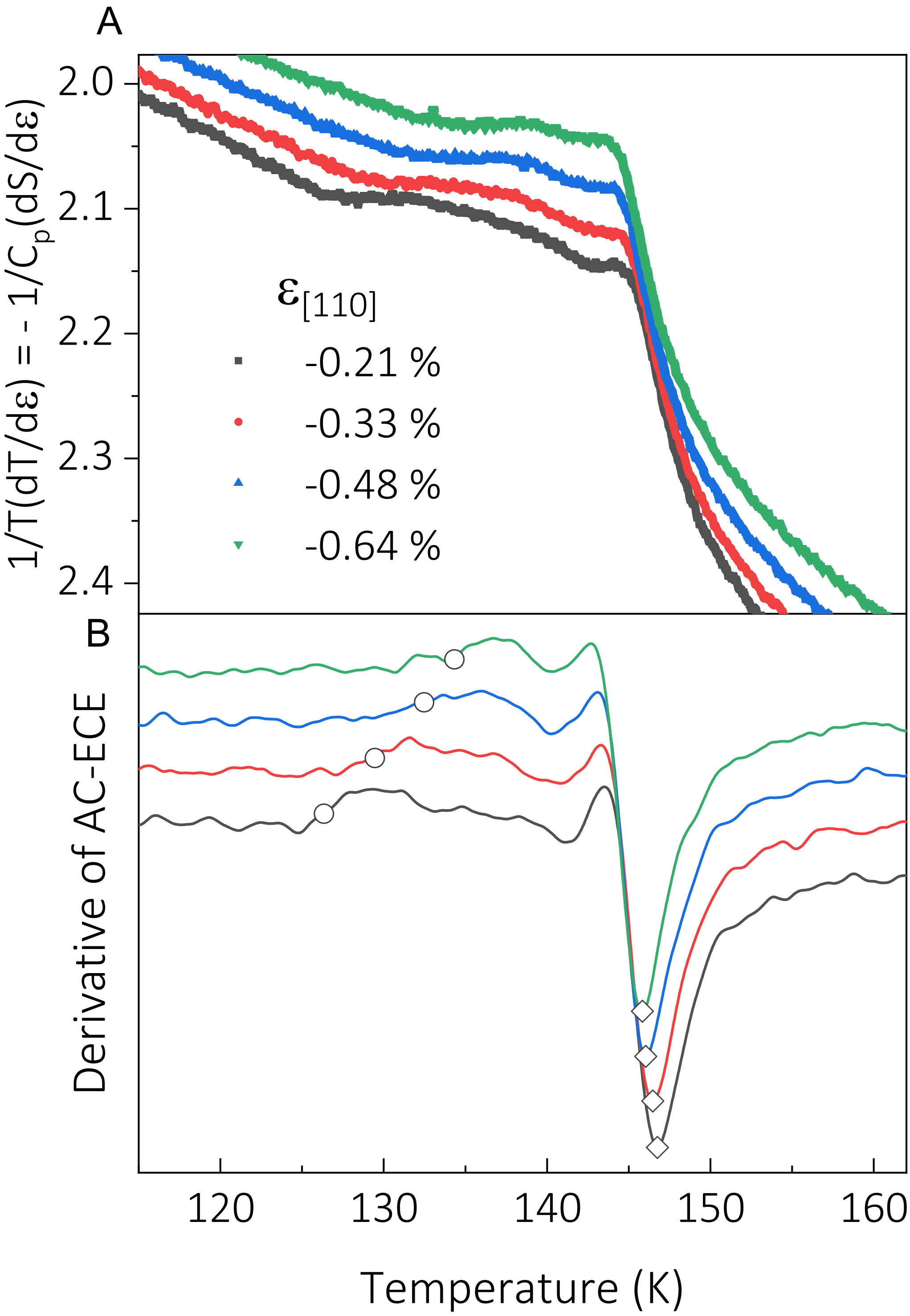

Figure 4.13: (A) AC-ECE curves as a function of temperature for different strain compressive values. (B) The respective derivatives of the AC-ECE signal showd to enhance the features observed. The open diamons are $T1$ and the open circles are $T2$.

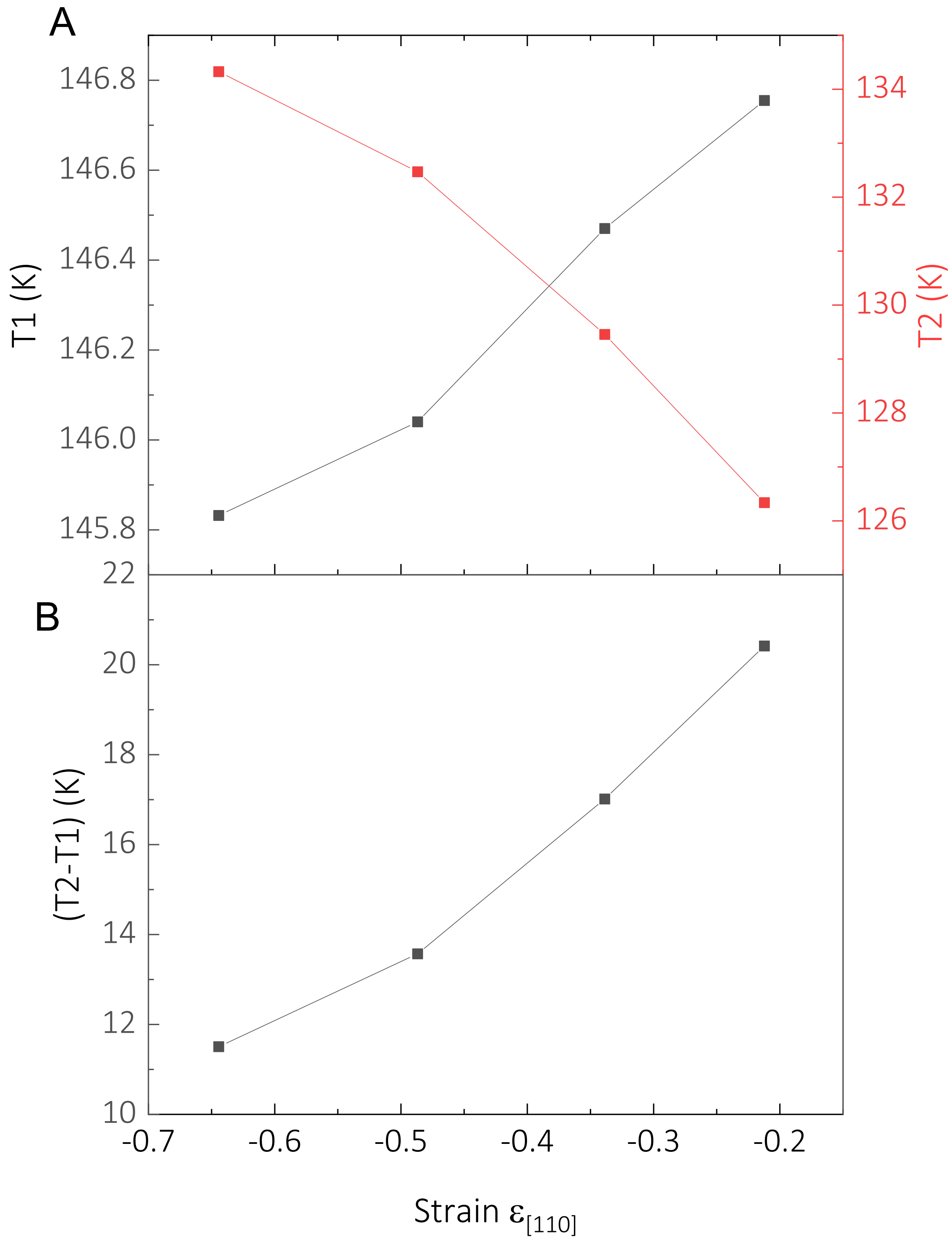

Figure 4.14: Here $T1$ and $T2$ were quantified to define the width of the transition. (A) $T1$ and $T2$ as a function of compressive strain along the [110] direction. (B) The difference between $T1$ and $T2$ as a function of [110]strain.

B were used to determine the transition temperature, which we call here $T1$, and it is labeled with open diamonds. The derivative curves were shifted vertically for a better observation of the features in the curves. For our lower strain value, $T1 = 147$ K, which is good agreement with the values obtained in previous resistivity measurements under small stress. Also, at lower temperatures, a second kink is observed in the signal, which is at the same region as the drop observed in the resistivity after the first upturn, which we address as the temperature were the CDW domains are fully formed. Interestingly, the same qualitative behavior is observed as the sample is compressed. At $\varepsilon_{[110]} = -0.21\%$ the transition is broader and the second kink in the AC-ECE signal is observed around $T2 = 125$K. As the sample is compressed, $T1$ decrease and the second kink at $T2$ move towards $T1$. In the derivatives $T2$ is labeled as the open circles. In figure 4.14A, the temperatures $T1$ and $T2$ are depicted as function of the applied strain $\varepsilon_{[110]}$, and it is possible to observe that the $T1$ and $T2$ have opposite behavior, as observed in the resistivity curves under stress. This is also shown in panel B, where the distance between $T1$ and $T2$ is plotted as a function of strain. This help us to infer that the transition also gets sharper under compression in thermodynamic measurements, showing the same qualitative behavior as in electrical transport measurements.

4.3 Conclusions

Here, we found an interesting response of the charge density wave and superconducting states upon uniaxial pressure applied along the [100], [110], and [111] crystallographic directions. We observe an important difference between hydrostatic and uniaxial pressure effects on the CDW and SC transitions. First, the SC is suppressed for all directions of applied stress, while in the hydrostatic pressure case, we observe the SC being slightly enhanced and the CDW being suppressed. The suppresion rates for the superconducting transition is different for stress along [100], [110] and [111] being suppressed more rapidly along the more rigid direction [100]. However, we observe a possible correlation between the suppression rates of superconductivity and the enhancement of the CDW hump-like feature in resistivity, where the feature increases faster along the direction where the SC is more rapidly suppressed. On the other hand, in the [111] direction, where the T_c is almost pressure-independent the CDW anomaly also shows a very weak pressure dependence. This suggest that the reduction of the density of states due to the CDW gap is playing a role in the suppression of T_c. Moreover, since the hump feature evolve differently at different directions, there might be an anisotropy in the CDW gap, as suggested for the isostructural CDW compound $Sr_3Ir_4Sn_{13}$, revealed by polarized X-ray absorption measurements [63].

Another interesting result was found for measurements along the [110] direction. The anomaly in the resistivty shows a broader feature with an upturn starting at the known transition temperature $T_{CDW} = 147$ K and drop further down in temperature, at around 125 K. As the sample is compressed, the transition sharpens, tending to a single peak-like feature. This was associated to a possible CDW domain degeneracy which may show up for measurements along this direction, the CDW wave vector direction $\mathbf{q}_{CDW} = (0.5\ 0.5\ 0)$. As the the sample is compressed and cooled, this degeneracy might be lifted, and the domains tend to align perpendicular to the direction of the stress application. Similar behavior is observed in Cu-based superconductors with striped CDW orders [64]. Here, the same qualitative behavior was observed using the AC Elastocaloric effect measurements, which we used as a thermodynamic indicator for the CDW phase transition.

Chapter 5

Tuning the charge density wave correlations in ScV_6Sn_6 by c-axis stress

5.1 Introduction

Kagome metals are an ideal platform for investigating the interplay between electronic correlations, lattice instability, and non-trivial band topology [71, 72, 73, 74, 75, 76]. Kagome lattices are a special type of geometrically frustrated atomic configuration with corner-sharing triangular lattices. Its unique electronic structure features have attracted much attention due to the presence of Dirac-like bands, van Hove singularities (vHS), and a flat band resulting from destructive interference of the Bloch electrons wave functions [72]. These features may give rise to non-trivial topology, strong correlations, and charge instabilities. In particular, the van Hove electron filling near the Fermi surface creates a divergent density of states (DOS) which is highly suitable for the emergence of exotic ground states, such as unconventional superconductivity [77], electronic nematicity [78], charge stripes [79, 80, 81], spin and charge density waves [82, 83].

The recently discovered bilayered Kagome metal ScV_6Sn_6 (Fig. 5.1) has garnered significant attention in the scientific literature owing to its potential as a platform for investigating the interplay between charge correlations and non-trivial band topology

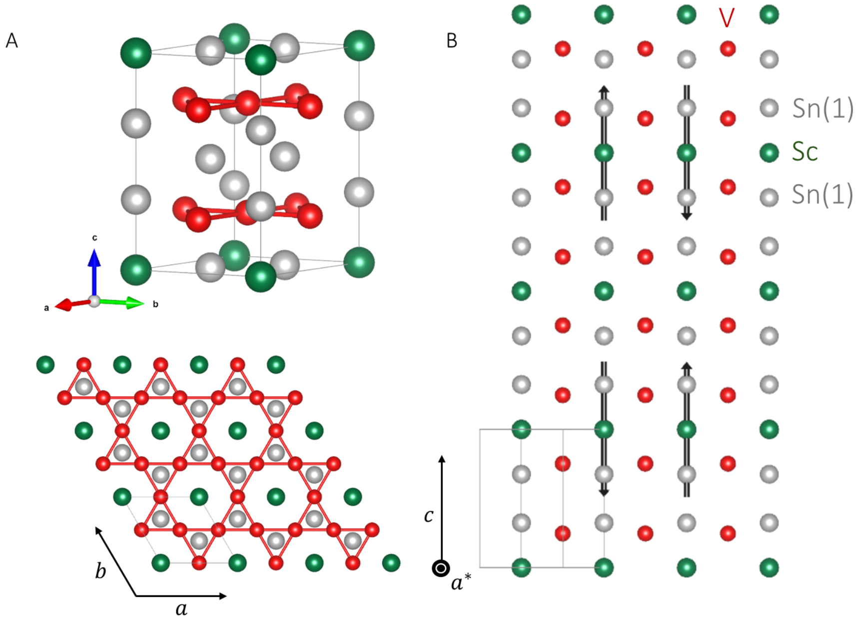

Figure 5.1: (A) Crystal structure of ScV_6Sn_6, visualized using *VESTA* [111]. (B) Side view of the expanded structure ScV_6Sn_6, the black arrows are used to depict the frustration of the Sn(1)-Sc-Sn(1) chains along the c-axis, as proposed in [114].

[19, 84]. This material is a member of the RT_6X_6 family (R = rare earth; T = V, Cr, Mn, Fe, Co; X = Ge, Sn), which has been extensively used as the landscape for the exploration of magnetism and non-trivial electronic properties [85, 86, 87, 88, 89, 90, 91, 92, 93, 94].

Unlike other V-based Kagome compounds such as AV_3Sb_5 (A = K, Rb, Cs), where the CDW state precedes the superconducting state [95, 96, 97, 98, 99, 100], ScV_6Sn_6 exhibits a CDW state without concurrent superconductivity. The CDW transition in ScV_6Sn_6 occurs at $T_{CDW} \sim 85$ - 90 K with a wave vector $\mathbf{q}_{\frac{1}{3}}= (\frac{1}{3}\frac{1}{3}\frac{1}{3})$ [19]. Under hydrostatic pressure, the CDW can be suppressed at $P = 2.4$ GPa, with no observable superconductivity down to 80 mK [101], likely related to the 3D nature of the structure of this compound.

Electrical resistivity measurements exhibit remarkable anisotropy between ρ_c and ρ_{ab}. In addition, upon applied magnetic fields along the a axis, the ρ_{ab} temperature dependence changes from a metal-like to insulator-like behavior above the CDW transition [102]. Hall effect measurements reveal a large anomalous component (AHC) that disappears above the CDW transition temperature, attributed to time-reversal symmetry breaking (TRSB) due to CDW looping currents [103]. Recent muon spin relaxation (μSR) measurements below the charge ordering temperature suggest TRSB, intensifying under an external magnetic field [104], though the existence of loop currents and TRSB in charge-ordered systems remains contentious [105, 106].

Another notable feature in in ScV_6Sn_6 is the significant out-of-plane component of the charge order, resulting in a larger displacement of Sc and Sn(1) atoms compared to the minor V in-plane distortion [19]. Both experimental [107] and theoretical [108] investigations have elucidated that the CDW order in ScV_6Sn_6 primarily stems from the *c*-axis motion of the Sc and Sn(1) atoms. Interestingly, the vHS originating from the V Kagome lattice remains unaffected by the onset of the CDW order [109, 110], which is in contrast to the behavior observed in the Kagome system AV_3Sb_5, where the vHS bands become gapped across the CDW transition [112, 113].

Various studies [20, 107, 114] have reported the presence of short-range correlations persisting at high temperatures $T > 200$ K, with a $\mathbf{q}_{\frac{1}{2}}= (\frac{1}{3}\frac{1}{3}\frac{1}{2})$ wave vector. These short-ranged instabilities appear to compete with the $\mathbf{q}_{\frac{1}{3}}= (\frac{1}{3}\frac{1}{3}\frac{1}{3})$ charge order that emerges at $T_{CDW} \sim 85$ K, and the superlattice peak intensities for $\mathbf{q}_{\frac{1}{2}}$ are partially suppressed upon entering the CDW state. In one scenario, the formation of the CDW order is attributed to the frustration of Sn(1)-Sc-Sn(1) chains in the Kagome lattice (See Fig. 5.1B), leading to the establishment of long-range order at $\mathbf{q}_{\frac{1}{3}}$ [114]. Conversely, Density Functional Theory (DFT) calculations predict soft phonon modes at the $\mathbf{q}_{\frac{1}{2}}$. Above T_{CDW}, inelastic x-ray scattering measurements observe a dominant dynamic short-range $\sqrt{3} \times \sqrt{3} \times 2$ CDW, in agreement with first-principle calculations. Below T_{CDW}, however, ScV_6Sn_6 orders in the competing channel $\sqrt{3} \times \sqrt{3} \times 3$, which is arguably driven by electron-phonon coupling [20].

In this thesis, we use hydrostatic and uniaxial pressure to explore how the CDW order responds to lattice compression in all directions, while specifically examining changes along the *c* axis. This has previously been done to study the interplay between electronic and lattice degrees of freedom in various types of orders [117, 118, 119, 120, 121]. In CsV_3Sb_5, uniaxial pressure experiments unveiled that variations in the *c* axis lattice parameter significantly influence T_c and T_{CDW}, regardless of whether the system is compressed under hydrostatic or uniaxial pressure [122]. Such findings indicated that the explicit breaking of lattice symmetry has minimal impact compared to alterations in the *c* axis lattice parameter. In the case of ScV_6Sn_6, the decision to apply uniaxial pressure along the *c* axis is grounded in prior investigations where the presence of Cr on the V site was found to suppress the CDW order, and structural analysis indicated that higher Cr content corresponds to a reduction in the *c*-axis, suggesting it may act as the main driving force for the suppression of charge order [109].

In this work, dilatometry measurements reveled a strong out-of-plane component of the thermal expansion coefficient, displaying a jump with a negative sign at T_{CDW}. We observe the suppression of the CDW order for both hydrostatic and *c*-axis uniaxial stress, with the CDW being suppressed more rapidly in the later case. We found an important qualitative change in the shape of the CDW order anomaly in the resistivity measurements under uniaxial stress, changing its character from a drop to a hump-like feature. Moreover, in isothermal resistivity measurements under uniaxial *c*-axis stress, a secondary anomaly is developed at lower temperatures. Finally we suggest to different potential scenarios to explain the data. One based on the competing CDW correlations and the second based a possible Lifshitz transition of the vHS.

5.2 Experimental results and discussion

5.2.1 Specific heat and thermal expansion

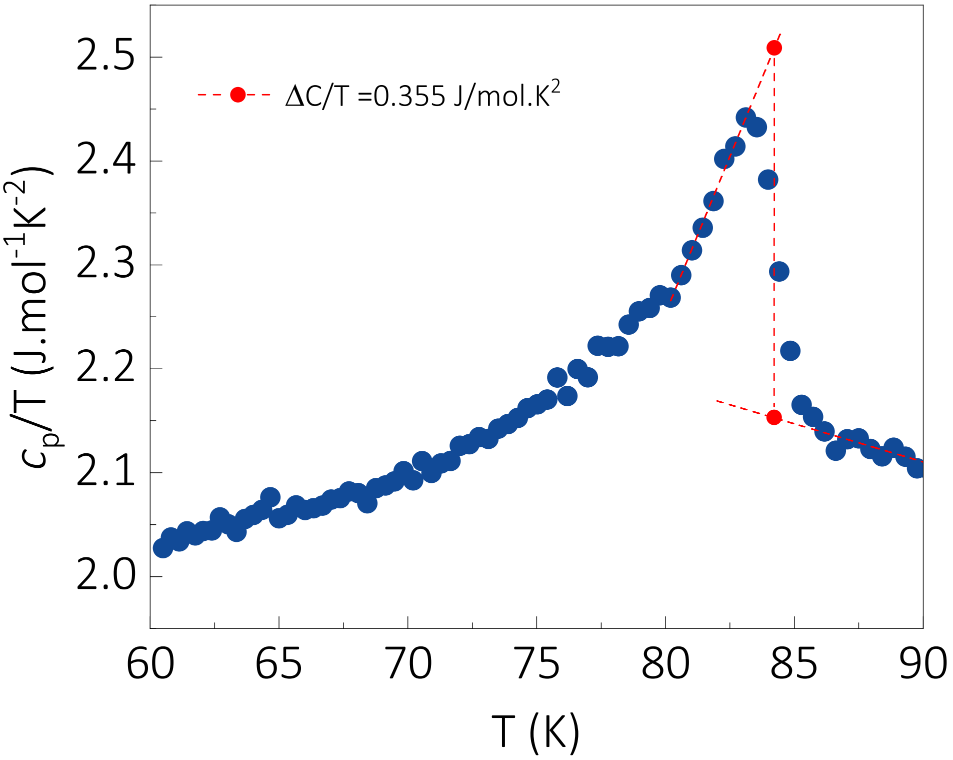

Figure 5.2: Heat capacity measurement as a function of temperature around the CDW transition. The red dashed lines were used to estimate the jump at T_{CDW}.

To gain insight into the thermodynamic characteristics of the CDW phase transition and evaluate its strain sensitivity, temperature-dependent heat capacity $C_P(T)$, and linear thermal expansion $\alpha(T)$ measurements were conducted.

Figure 5.2 shows the heat capacity measurement taken in a temperature range from 60-90 K, around the CDW ordering temperature. A jump-like feature is observed in the heat capacity curve around $T_{CDW} = 85$ K, marking the transition temperature. The size of the jump was estimated to be $\Delta C_P = 0.355$ J/mol.K^2, determined using the criteria shown in the curve. Figure 5.3A shows the $\Delta L/L$ curve as a function of temperature measured along the a^*-axis (blue dotted curve) and c-axis (red dotted curve). The temperature dependence of the linear thermal expansion $\alpha(T)$ is obtained from the derivative of $\Delta L/L$ and the coefficients measured along a^* (in plane direction perpendicular to a axis) and c are shown in figure 5.3B. The CDW transition is marked by a jump in $\alpha(T)$, which is agreement with the T_{CDW} observed in heat capacity. The inset in Fig. 5.3B shows the $\alpha(T)$ curves zoomed in around the CDW transition and the criteria used to determine T_{CDW} and the size of the jumps for c and a^*. Linear fits were performed below and above the jump and a vertical line is traced to determine the jump size. Importantly, there is a small offset in T_{CDW} between α_c and α_{a^*} (about 2 K). Since the curves were measured in the same sample, this offset is likely due to the induced strain in the sample when it is attached in the capacitance cell. As will be shown next, the sign of the jump in thermal expansion measurements are related to the pressure dependence of the transition temperature, therefore since the sample is slightly compressed upon attaching it to the dilatometer cell along the direction in which the $\alpha(T)$ will be measured, this can affect the transition temperature by an small amount.

From the measurements it is clear that the jumps along the a^*-axis and c-axis have opposite signs, *i.e.,* $\Delta\alpha_c < 0$ and $\Delta\alpha_a^* > 0$ meaning that there is an expansion of the unit cell along c and a contraction of the a^*, as the sample is cooled through T_{CDW}. Moreover, the relative sizes of the jumps are significantly different, $\Delta\alpha_c =$ -116$\times10^{-6}$ K^{-1} and $\Delta\alpha_a^* = 42.1\times10^{-6}$K^{-1}, showing that the structural change is strongly anisotropic. This is partially in agreement with temperature-dependent X-ray diffraction measurements. While c increases by 0.04%, no noticeable change occurs in a [19]. This jump indicates a higher strain sensitivity of the phase transition along the c axis. Thermal expansion measurements on CDW systems have previously been done [30, 31, 32]. For example, in $LaAgSb_2$, a comparable trend was noted at T_{CDW}, wherein the magnitudes and signs of the relative jumps differ: $|\Delta\alpha_c| > |\Delta\alpha_a|$, with $\Delta\alpha_c < 0$ and $\Delta\alpha_a > 0$ [33]. It was recently reported a preprint showing thermal expansion measurements on the related compound CsV_3Sb_5, and a similar behavior was observed in the coefficients along a and c [123]. The out-of-

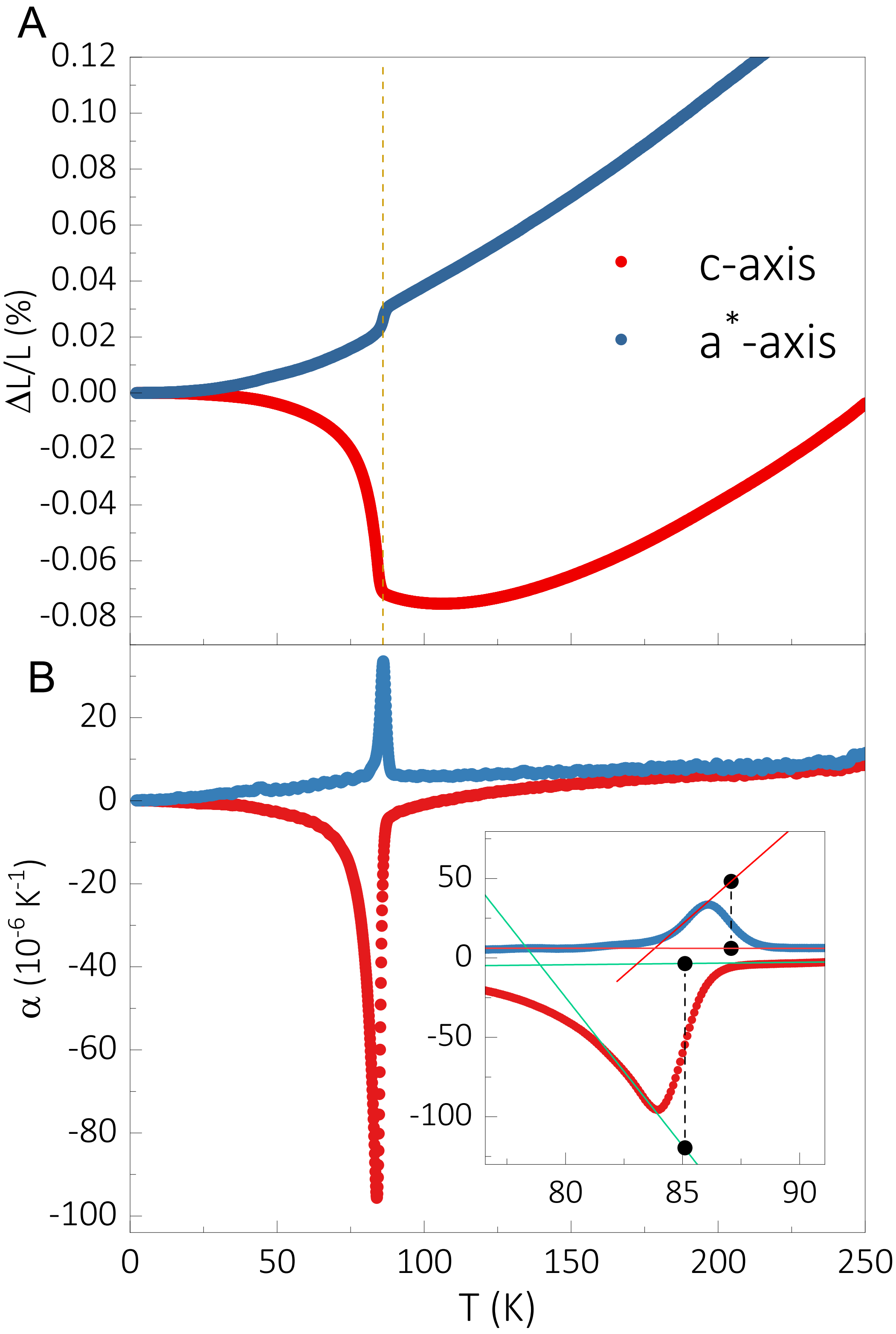

Figure 5.3: (A) $\Delta L/L$, (B), and thermal expansion measurements as a function of temperature. The thermal expansion measurements were done along the a^* and c crystallographic axis.

plane coefficient α_c showed a strong negative jump at T_{CDW}, while a smaller but positive jump was found in α_a. This results corroborates with our finds, due to the similar nature of these two compounds. Using the Ehrenfest equation (Eq. 5.1) one can correlate the jumps in heat capacity and thermal expansion coefficient with the pressure dependence of the transition temperature, as discussed below.

$$\frac{dT_c}{dP} = V_m \frac{\Delta\beta}{\Delta C/T_{CDW}}. \tag{5.1}$$

Here, P is pressure, $\Delta\beta$ is the volumetric thermal expansion jump, V_m is the molar volume and ΔC is the heat capacity jump. Since ΔC is always positive, the sign of the thermal expansion jump defines if the transition temperature is suppressed or enhanced upon pressure. The relative jump sizes suggest that a larger effect is expected for pressures along the c-axis. Moreover, according to Eq. 1, the relative size and negative sign of $\Delta\alpha_c$ dominates the pressure dependence of the transition temperature, which should be suppressed under hydrostatic pressure, in agreement with the previous report [101]. A more detailed analysis will be done later in text, once we show the measurements under hydrostatic and uniaxial pressure. Using the jumps obtained in heat capacity and thermal expansion one can estimate the suppression rate for T_{CDW} using the Ehrenfest relation and compare with the direct measurements of dT_{CDW}/dP under uniaxial pressure. For now, one can say that the anisotropy in thermal expansion and the high jump value for measurements long c motivated us to study this sample by applying uniaxial pressure along the c-axis.

5.2.2 CDW under Uniaxial and hydrostatic pressure

After the evaluation of the potential strain sensibility of the c axis, we turn to the electrical resistivity measurements under c-axis uniaxial stress, to understand how the CDW order is affected by this tuning parameter. The measurements were performed by applying stress on a bar-shaped sample along the c-axis with the electrical current along the same direction. In figure 5.4A we show the electrical resistivity curves as a function of temperature for many stress values as well as the respective derivatives $d\rho/dT$ in 5.4B. The CDW transition temperature has a strong sensitivity to c-axis stress, being suppressed with compression. The CDW transition

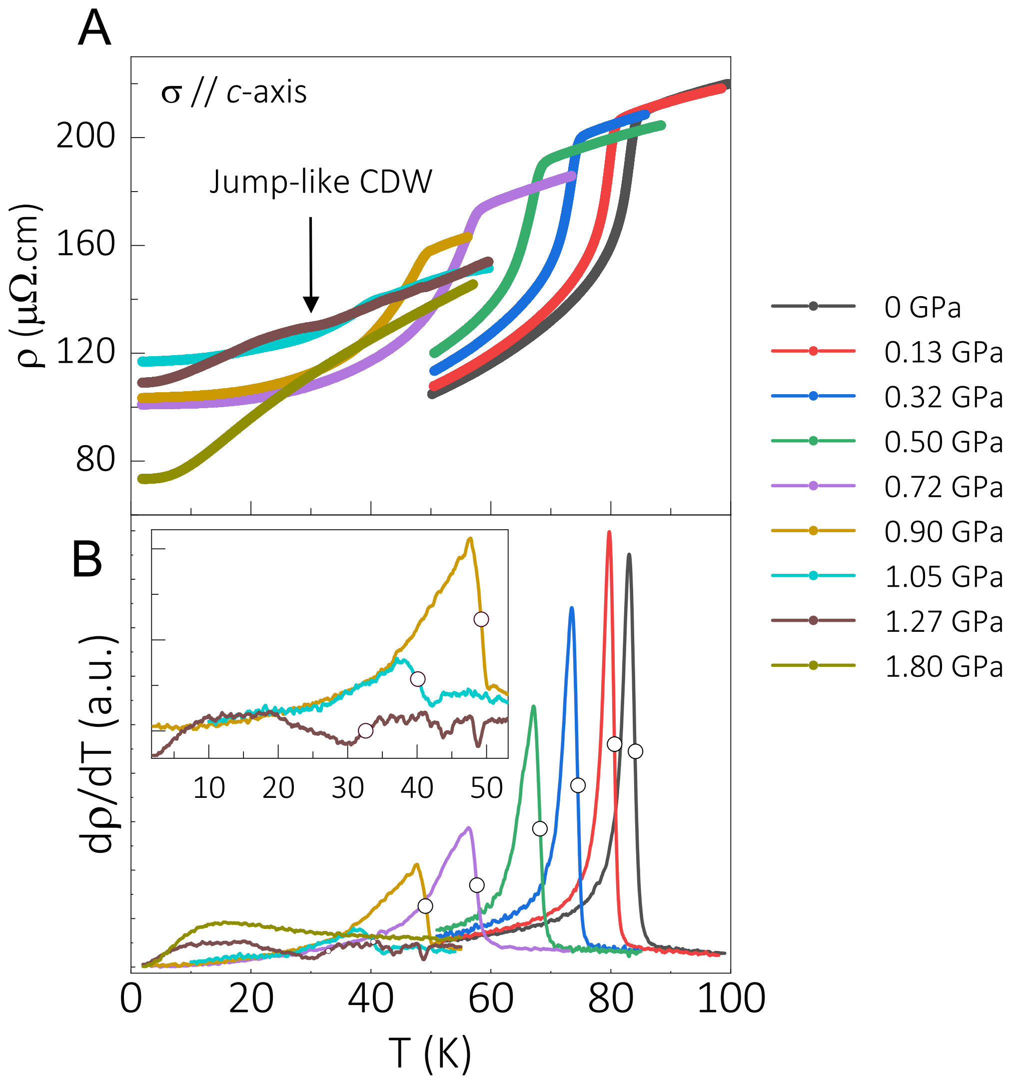

Figure 5.4: (A) Temperature-dependent resistivity curves for different applied *c*-axis uniaxial stress. The black arrow indicates the change in CDW anomaly character from drop to upturn. (B) The respective derivatives $d\rho/dT$. The open circles represente the criteria used to determine T_{CDW} (mid-point of the rising edge). The inset is zoomed region for pressures σ = 0.90 - 1.27 GPa, where the change in the character is observed. The derivatives evolve from a jump-like (cyan curve) to a peak-dip (brown curve) feature.

decreases and gets broader as the pressure increases, keeping the same characteristic up to $\sigma_c = 1.05$ GPa. At higher pressures, the anomaly changes shape, and a small upturn appears around $T \sim 30$ K (marked with a black arrow in Fig. 5.4A). This change in the transition character, from drop-like to hump-like feature is a strong indication of a change in the CDW wave vector, which generates a change in the scattering rates and is reflected in the electrical resistivity.

At $\sigma_c = 1.8$ GPa no feature is observed in the resistivity curve and the system recovers Fermi-liquid behavior ($\rho \propto T^2$) at lowest temperatures. The transition temperatures were determined by the mid-point of the rising (dropping) edge of the derivatives (open black circles). The inset in figure 5.4B is used to show the higher pressure $d\rho/dT$ curves, detailing the region around T_{CDW} for $\sigma_c = 0.90$, 1.05, and 1.27 GPa. We see that at $\sigma_c = 1.05$ GPa the derivative rises, while for $\sigma_c = 1.27$ GPa a drop is observed, featuring the change in the shape of the anomaly at T_{CDW}.

To compare to our uniaxial pressure data, we also made measurements of temperature -dependent electrical resistance under hydrostatic pressure[1]. The resistance curves as a function of temperature (R×T) are shown in figure 5.5A for many applied pressures. As one can see, the R×T curves are qualitatively similar to those obtained in *c*-axis uniaxial stress measurements. However, the transition broadens more rapidly compared to the uniaxial pressure case, and a discernible shoulder emerges for pressures exceeding $P > 0.18$ (marked as black arrows in Fig. 5.5B). The widening of the transition becomes more apparent in the derivative curves depicted in Figure 5.5B. One conceivable reason for the emergence of this shoulder around the transition zone could be attributed to sample inhomogeneity. As in the uniaxial pressure, the mid-point of the rising edge was used to determine the transition temperature.

In comparison with the previous measurements under hydrostatic pressure, our

---

[1] Electrical resistivity measurements under hydrostatic pressure were conducted using a piston-clamp pressure cell with Daphne 7373 oil as the pressure medium. Resistivity measurements employed a standard four-point technique with the current along the [001] direction (*c*-axis). The pressure within the sample space was determined using the shift in the superconducting transition temperature of Pb. For temperature sweeps, the hydrostatic cell were loaded into a Quantum Design Physical Property Measurement System (PPMS). The hydrostatic pressure measurements were performed by Dr. M.O. Ajeesh, postdoc at the time in the SCES team in MPA-Q, at Los Alamos National Laboratory. My sincere acknowledgments to Ajeesh for this contribution.

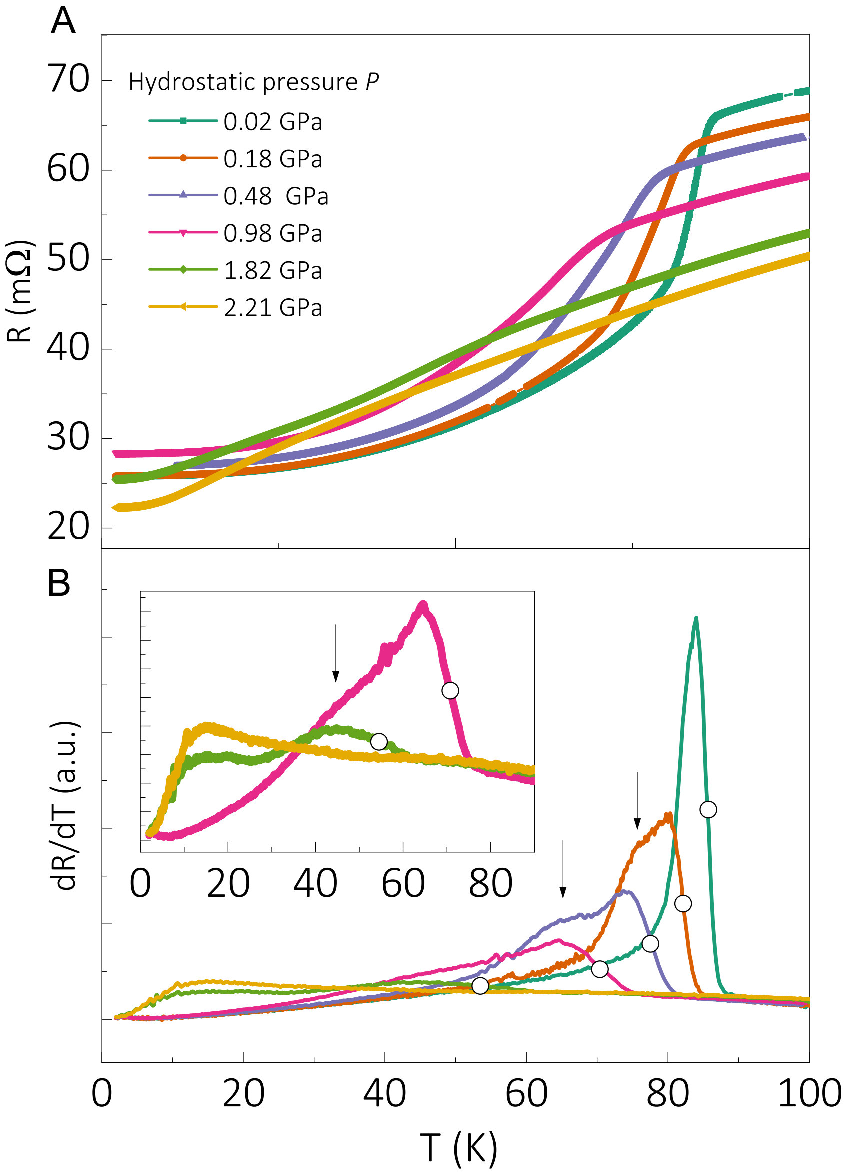

Figure 5.5: (A) Temperature-dependent resistance curves for different applied hydrostatic pressures. (B) The respective derivatives $d\rho/dT$. The open circles represente the criteria used to determine T_{CDW} (mid-point of the rising edge). The inset is zoomed region of the derivative curves for pressures σ = 0.98 - 2.21 GPa.

results are qualitatively different. In X. Zhang *et al.* [101], the broadening of the transition is less evident, and the transition remains well defined until reaching a pressure of $P = 2.04$ GPa. The alteration in the anomaly's shape is only observed as a minor kink beyond $P = 2.19$ GPa, a value close to our upper-pressure limit of 2.21 GPa. This proximity likely explains why this feature is not discernible in our measurements. Also, their resistivity measurements were performed with the electrical current in the ab-plane, while our measurements were done in a bar-shaped sample with $I//c$. Even though the pressure is equally distributed, the current is along the [001] direction, which makes our measurements more sensitive to changes in the scattering rate along the c-axis.

To better understand the effects of uniaxial pressure, resistivity was measured as a function of applied uniaxial pressure at fixed temperatures. The $\mathrm{R}\times\sigma_c$ curves are shown in figure 5.6A, and their derivatives are shown in figure 5.6B and C. Since the CDW is suppressed with the c-axis compression, the pressure P_{CDW} (at fixed temperature) at which the system goes from CDW ordered to the normal state is marked as a change in the inflection of the curves, indicated by the red arrows for different temperatures. These points are also shown as open red symbols in the derivative curves. As we decrease the temperature a second nearby feature, which we call hereafter P^{*}(or T^{*}), starts to appear at slightly lower pressure (black arrows) regarding to the main transition and becomes more noticeable at lower temperatures. In figure 5.6A, B, and C one can notice that the P_{CDW} and P^{*} are continuously moving upwards in pressure, which means that the associated transition temperatures T_{CDW} and T^{*} are being suppressed. Interestingly, at $T = 25$ K, the $\mathrm{R}\times\sigma_c$ form a plateau, where both features are seemly close in the resistance axis. For $T < 25$ K, the anomaly in P_{CDW} (or T_{CDW}) is suppressed, the curve is dominated by the lower-pressure secondary feature, and the inflection change mainly occurs at P^{*}. As T_{CDW} gets weaker, T^{*} seems to be slightly enhanced. The nature of this second feature is not clear from our measurements, nevertheless, we discuss two possible scenarios later in the text. One is based on the reinforcement of the short-ranged CDW correlations with a different wave vector and another based on a possible stress-induced Lifshitz transition of the vHS.

The pressure-temperature phase diagram show in figure 5.7 was constructed to compare the suppression rate between hydrostatic and uniaxial pressure along the

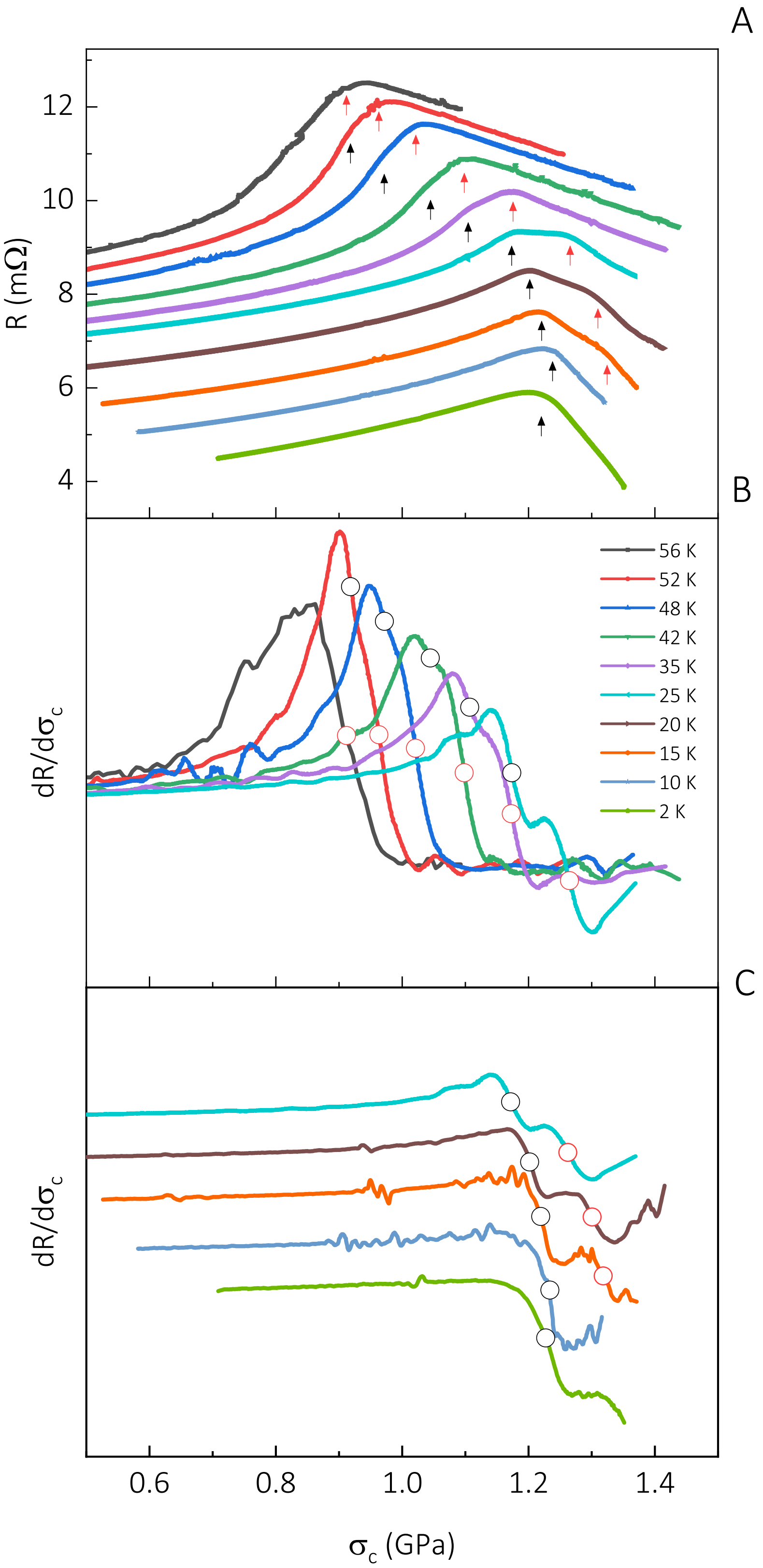

Figure 5.6: R×σ_c curves at fixed temperatures (A); The red and black arrows show the transition points defined as P_{CDW} (T_{CDW}) and P^*_{CDW} (T^*_{CDW}), respectively. In the derivatives of the R×σ_c curves (B, C) the open red (black) symbols show the T_{CDW} (T^*_{CDW}) transition temperature, defined as the mid-point of the dropping edge. The data in A and C for temperatures below 25 K is shifted vertically for clarity.

c-axis. The yellow triangular symbols represent the main transition temperatures from our hydrostatic pressure data. The red squared symbols are the T_{CDW} temperatures taken from the resistivity measurements as a function of temperature. T_{CDW} (blue squares) and $T^*(P^*)$ (light green diamonds) were obtained from the isotherm measurements of $R \times \sigma_c$. The first noticeable feature of the phase diagram is the difference between T_{CDW} under hydrostatic (HP) and *c*-axis uniaxial pressure (UP) measurements. While in the HP case the transition temperature is linearly suppressed under compression, the UP dependence of T_{CDW} shows a approximately linear behavior up to $\sigma_c \approx 1$ GPa. For higher pressures, looking at the points from $R \times \sigma_c$, a stronger non-linar behavior is observed. This change in slope at around $\sigma_c \approx 1$ GPa might be related to the destabilization of the main CDW transition, since it is around this pressure value where the transition gets weaker and the lower pressure secondary anomaly T^* sets in. Moreover, for $\sigma_c > 1$ GPa we observed shape change of the CDW transition in the resistivity curves as a function of temperature, from drop-like to a hump-like feature (Fig. 5.4A). In the lower temperature curves P^* seems to become almost temperature-independent, as can be seen in the phase diagram and from Figure 5.6.

As the thermal expansion measurements indicate, a positive peak in $\Delta\alpha_{a^*}$, counteracts the suppression of the phase transition under hydrostatic pressure, thereby reducing the rate of suppression. Conversely, for the *c*-axis UP the suppression is expected to be strong due to the lack of the in-plane component, as stated here. From the linear fit in HP dependence of T_{CDW} (yellow dashed line in Fig.5.7) we obtain a suppression rate of dT_{CDW}/dP = -17.5 ± 0.5 K/GPa. While for uniaxial pressure, we perform a linear fit from σ_c = 0 - 1 GPa (linear region), obtaining a dT_{CDW}/σ_c = -41.2 ± 2 K/GPa, which is roughly the double of the rate for hydrostatic pressure compression, confirming the stronger strain sensibility of the *c* axis. Using the Ehrenfest relation given in equation 5.1, one can estimate the pressure dependence of the CDW transition. For this, one must calculate the jump in the volume thermal expansion $\Delta\beta$, which for this hexagonal system will be given by $\Delta\beta = \Delta\alpha_c + 2\Delta\alpha_{a^*} = -74 \times 10^{-6}\ \mathrm{K}^{-1}$. Using the molar volume $V_m = 14.34 \times 10^{-5}\ \mathrm{m^3 mol^{-1}}$. This values yields to a $dT_{CDW}/dP \approx$ - 29 K/GPa, which is higher than the obtained from the linear fit. This overestimation can be related to errors associated to the determination of the heat capacity and thermal expansion jumps.

Conversely, by using the data from [101], we obtain $dT_{CDW}/dP \approx$ - 36 K/GPa. Although this value seems to be closer to the estimated by using the equation 5.1, they reported a first increase in T_{CDW} followed by a decrease under hydrostatic pressure. This first increase followed by a decrease in T_{CDW} is not expected due to the large out-of-plane component observed in our thermal expansion measurements, which will dominate the hydrostatic pressure-dependence. Therefore, they most likely obtained wrong values for the pressure and/or the temperatures in their measurements. Another study was recently published on arxiv (March 04 2024) [124], where is also reported resistivity measurements under hydrostaic pressure on this system. From their data we obtained $dT_{CDW}/dP \approx$ - 26 K/GPa, which is close of our estimated from the equation 5.1. In contrast to the data from [101], they do not observe the rise in T_{CDW} prior to the suppression, in agreement to our data. The figure 5.8 show a phase diagram comparing our hydrostatic pressure data and both studies cited above.

Another interesting result from our resistivity measurements is the behavior of the residual resistivity with pressure. In figure 5.9A-C, we show the variation of the resistance with pressure, plotted as $\Delta R/R_{\mathrm{min}}$, where ΔR = R - R_{min}. R_{min} is the resistance at the minimum pressure measured. In the case of the hydrostatic pressure this is close to 0 GPa. For the *c*-axis uniaxial stress, it is around $\sigma_c \approx 0.7$ GPa, which was the minimum measured due to our measurements limitations. In the uniaxial pressure, the maximum voltage one can apply to the piezo stacks is temperature-dependent. At T = 2 K one can use the full voltage range, therefore, in order to reach higher pressures, the measurements for low temperatures were done using a secondary DC source to reach voltages up to 300 V, and the minimum voltage was 100 V, which give us a initial pressure of 0.7 GPa. Although we cannot compare quantitatively the $\Delta R/R$ for different measurements, it is possible to se the qualitative changes. The curve in figure 5.9C is the $R \times \sigma_c$ taken at T = 2 K, which we can used as a residual resistivity. The data points in A and B, are from the $R \times T$ curves for hydrostatic and uniaxial pressure, respectively. The residual resistivity increases, reaching a maximum at around $P \approx$ 1 - 1.2 GPa for all curves. For uniaxial pressure, the subsequent drop is much sharper than in the hydrostatic case, this is expected since the sample is more sensible to the *c*-axis stress.

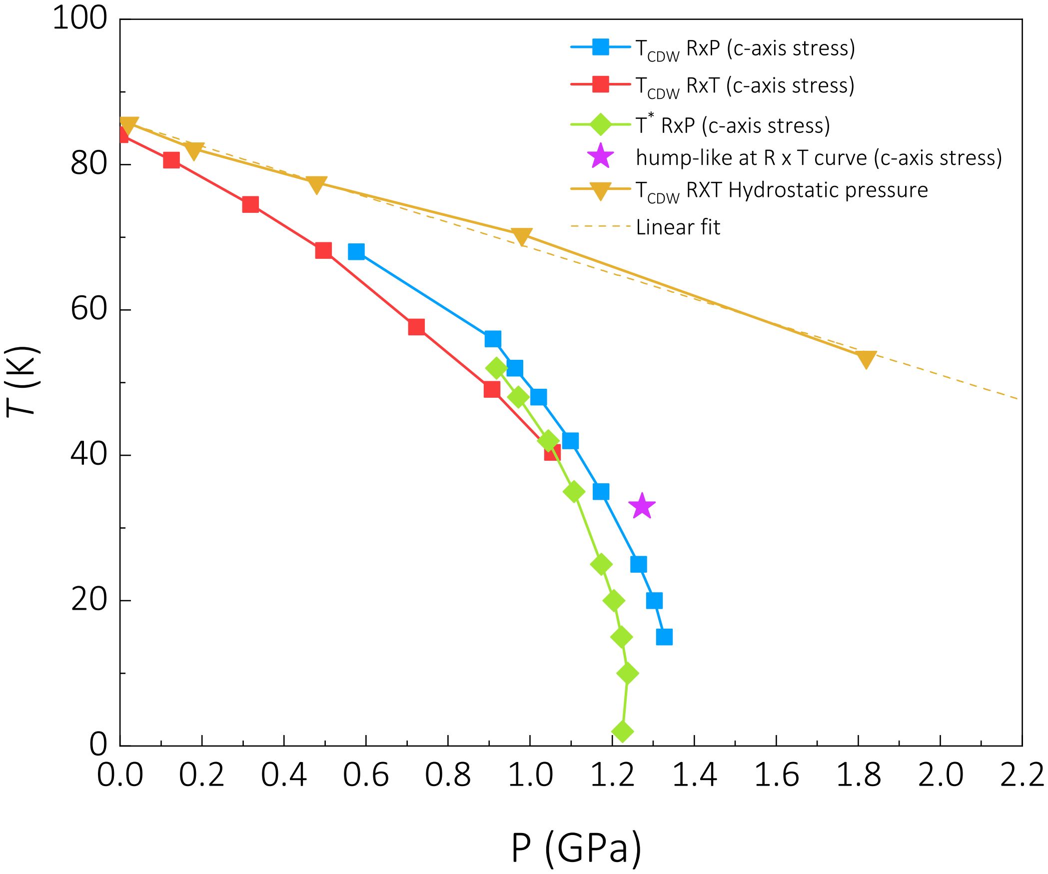

Figure 5.7: Pressure-temperature phase diagram produced using the electrical resistivity measurements under uniaxial and hydrostatic pressure.

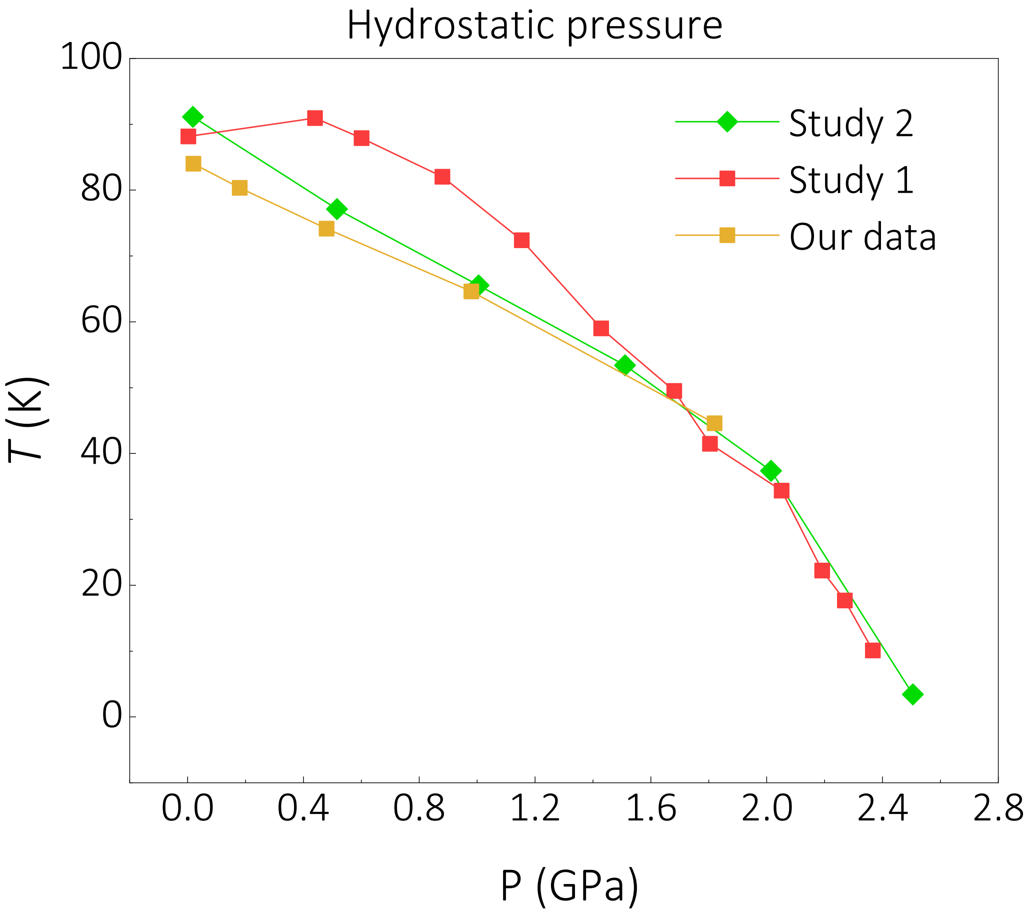

Figure 5.8: Pressure-temperature phase diagram comparing different studies on ScV_6Sn_6 under hydrostatic pressure. Study 1 is the data from reference [101] and study 2 is the data from [124].

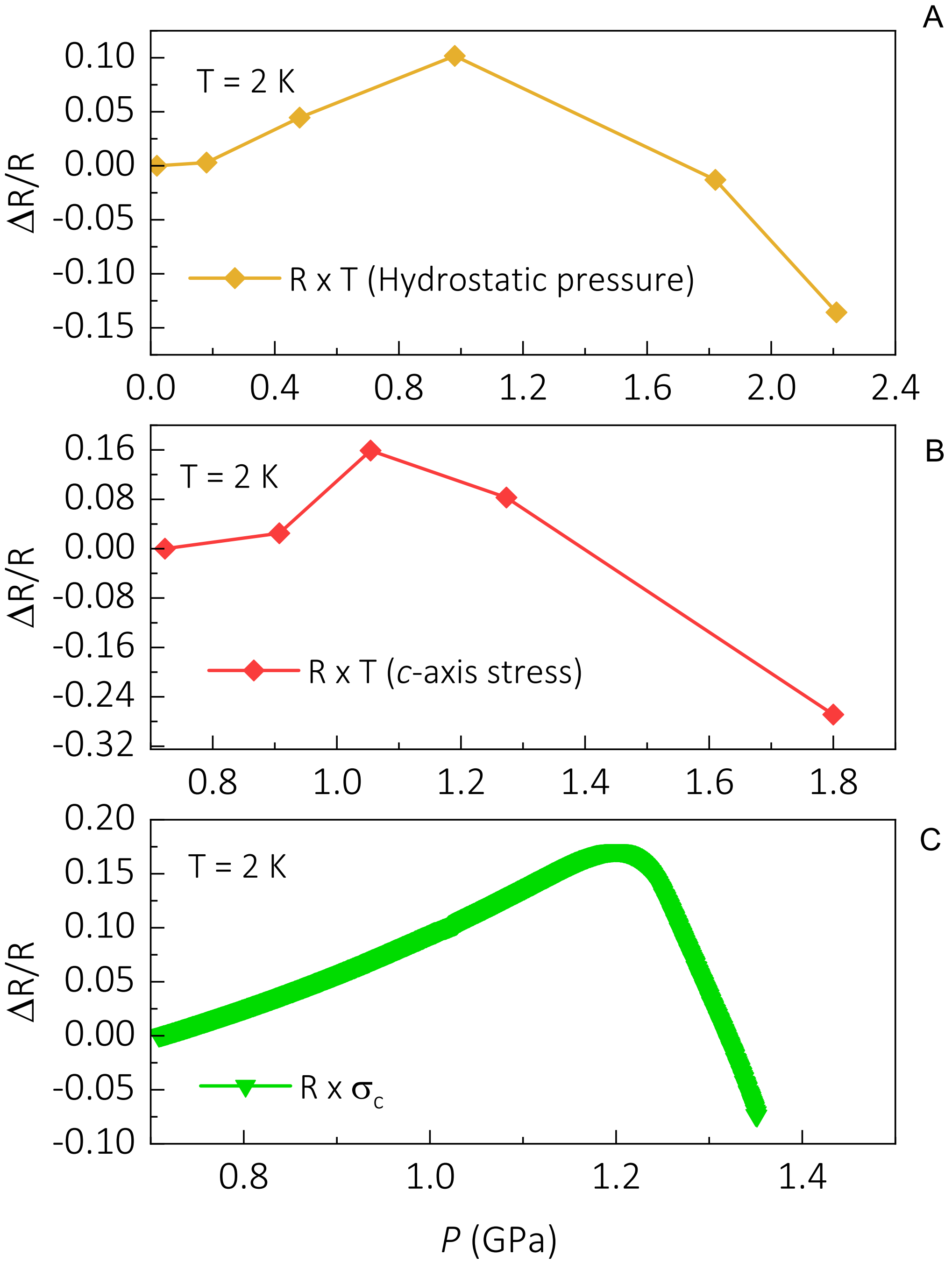

Figure 5.9: Pressure-dependent resistance variation $\Delta R/R$. (A) Hydrostatic pressure, (B) Uniaxial pressure, from $R \times T$ curves and (C) $R \times \sigma_c$ at 2 K.

5.3 Discussion

To explain our data, we propose two possible scenarios: i) Our resistivity curve as function of temperature for c-axis stress between 1.05 and 1.27 GPa, demonstrated a change in the character of the CDW transition, which is an indication that the CDW wave vector has changed. A second kink at (T^* or P^*) was observed at lower pressures in the isotherm $R \times \sigma_c$ curves, which evolves as the temperature is lowered and we address this second kink with a possible reinforcement of the $\mathbf{q}_{\frac{1}{2}}$ short range correlations, corroborating with the observations in $\rho \times T$. ii) In the second scenario, T^* could be addressed to a totally different phenomena, where the c-axis uniaxial stress could induce a Lifshitz transition due to the Van Hove singularities transverse the Fermi surface. Both scenarios are explained in more details below:

Scenario i):

The proposed $\mathbf{q}$-dependent driven $\mathbf{q}_{\frac{1}{3}}$ order explains the previously observed drop in the resistivity measurements at T_{CDW} [20], and our pressure-dependent measurements align with this scenario. Upon suppressing the transition, the scattering is reduced causing the inflection change in the $\mathrm{R}\times\sigma_c$ curves at the transition. In addition, we observe that even the secondary transition is also suppressed upon compression, which also can be explained if one considers this feature to be correlated to the $\mathbf{q}_{\frac{1}{2}}$ state; if the latter is developed by phonon softening of out-of-plane modes, the pressure along c crystallographic axis can promote the hardening these soft phonons [125], suppressing the transition. Therefore, the suppression of the $\mathbf{q}_{\frac{1}{3}}$ order may be, on one hand, enhancing the $\mathbf{q}_{\frac{1}{2}}$ correlations, promoting a change in the most favorable ground state, and meanwhile $\mathbf{q}_{\frac{1}{2}}$ is also suppressed through phonon hardening.

Our results also corroborate with the order-disorder scenario proposed by G. Pokharel *et al.* [114]; The compression along the c-axis could lead to the stabilization of the frustrated Sn-Sc-Sn chains which makes the onset of long-range order $\mathbf{q}_{\frac{1}{3}}$ no longer necessary to minimize the system energy, pushing the transition down to the energy scale where the short-range correlations $\mathbf{q}_{\frac{1}{2}}$ become the main ground state. Interestingly, we see that the $\Delta R/R_{\mathrm{min}}$ peaks out at the same region in phase diagram where the CDW anomaly in $R \times T$ changes from drop to hump-like and at around where T^* appear in $R \times \sigma_c$. Considering this scenario, the competition between the two ordered states may be enhancing the scattering in this region, due to the destabilization of the main CDW order. Although the long range CDW stabilizes at $\mathbf{q}_{\frac{1}{3}}$, the observed phonon softening mainly occur in the $\mathbf{q}_{\frac{1}{2}}$ channel [107], which is counter intuitive.

Interestingly, A. Subedi performed first principle calculations to map the energy landscape of the structural distortion associated to the CDW transition in this material [115]. Its results are in agreement with the previous DFT calculations [108], showing that the dominant phonon instability occur at $\mathbf{q}_{\frac{1}{2}}$. However, he found that despite the instability at $\mathbf{q}_{\frac{1}{2}}$ causes the largest energy gain, only two distinct structures occur due to this stability, separated by 6 meV/f.u., while for the $\mathbf{q}_{\frac{1}{3}}$, there are six possible distorted structures lying within 2 meV/f.u. of each other. Therefore, since there are more nearly-degenerated distinct structures, the emergence of the $\mathbf{q}_{\frac{1}{3}}$ the energy gain due to this larger multiplicity might be favoring $\mathbf{q}_{\frac{1}{3}}$. He argue that this is a analogue to the order-by-disorder mechanism discussed for frustrated magnetic systems [116]. In the context of our measurements, since the $e-ph$ coupling is strong in this material, tuning the lattice by *c*-axis stress may disrupt the balance between the multiple instabilities associated to different CDW wave vectors, causing a change in the most favorable ground state.

Scenario ii): This scenario is based on the rich nature of the electronic band structure in ScV_6Sn_6. As mentioned before, the geometrically frustrated triangular lattice of this compound features Dirac bands, Van Hove singularities and flat bands (See figure 5.10A). Multiple Kagome-derived vHS are observed near the Fermi surface at **M** point of this compound [109, 110, 127], as revealed by ARPES measurements. The vHS bands are two-folded, having bands with two opposite concavities, classified as electron-like vHS1 and hole-like vHS2. The figure 5.10B show the band structure along the $\mathbf{\Gamma}-\mathbf{M}-\mathbf{\Gamma}$ path reported in [127], obtained from DFT calculations (uper panel) and ARPES measurements (lower panel), showing that the theorectical prediction is in good agreement with the experiments. The vHS1 and vHS2 bands are marked with pink arrows. The vHS1 band has its maximum slightly above the Fermi surface, while vHS2 is slightly below. This observation is very similar to the case of AV_3Sb_5 [112, 113]. However, in contrast to the AV_3Sb_5 system, the VHs in ScV_6Sn_6 do not become gapped across the CDW transition and, therefore, it is argued that it should play a marginal role in the formation of the charge ordered state. Nonetheless, in ScV_6Sn_6 the vHS are still there and even though the CDW and vHS seem to be uncorrelated, the an external stimuli like *c*-axis stress might be acting on changing the Fermi surface topology, bringing the vHS to play a role in the physical properties of ScV_6Sn_6 as we discuss below. It is noteworthy that Mozaffari *et. al.* [128] suggested that the sublinear behavior observed in the resistivity measurements at temperatures above T_{CDW} is derived from the contribution of the thermally activated vHS to the scattering rate.

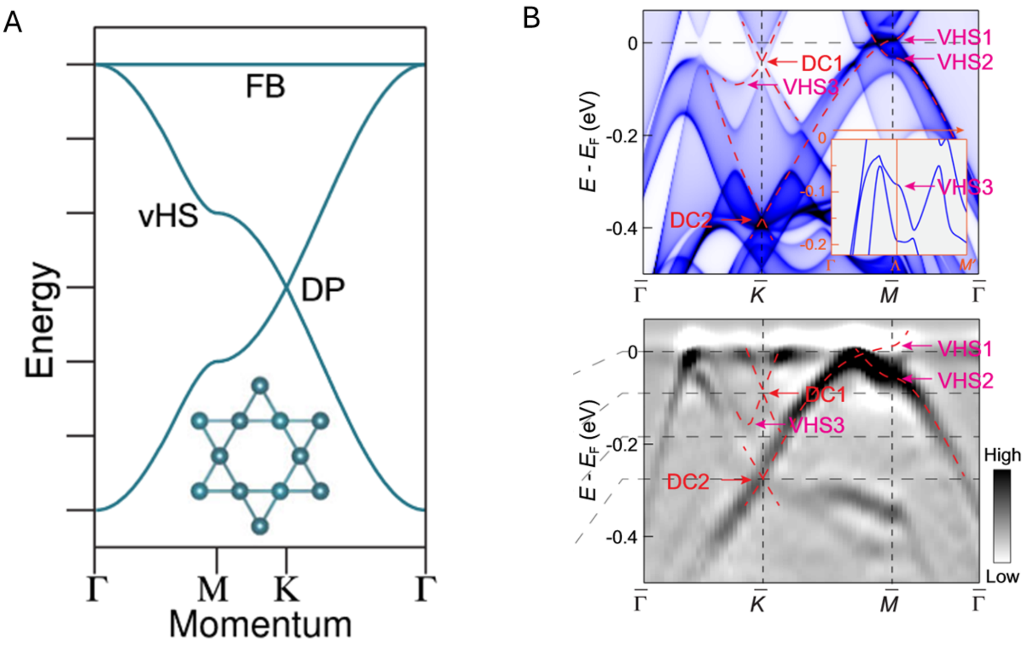

Figure 5.10: (A) Band structure of a Kagome lattice (Figure from reference [109]). (B) Calculated band structure (upper panel) and measured dispersion (lower panel) along the $\mathbf{\Gamma} - \mathbf{M} - \mathbf{\Gamma}$ path. Dirac cone and vHS are indicated by red and pink arrows, respectively. (figure from reference [127]).

The vHS are characterized by a minimum, maximum or a saddle point in the electronic dispersion $\varepsilon(\mathbf{k})$, and this has a strong consequence in the density of states $N(\varepsilon)$. The $N(\varepsilon)$ is the number of allowed wave vectors per unit energy at each energy of the system. Mathematically we can express as the following:

$$N(\varepsilon) = \frac{1}{4\pi^3} \int \frac{1}{|\nabla\varepsilon(\mathbf{k})|}. \tag{5.2}$$

Therefore, since it inversely depends on the divergence of the electron dispersion $\nabla\varepsilon(\mathbf{k})$, for a dispersionless band, like in the saddle point of the vHS, the $N(\varepsilon)$ is strongly enhanced. This enhanced density of states will influence the physical properties of the material depending on the proximity to the Fermi surface. In systems such as in the unconventional superconductor Sr_2RuO_4, the vHS are located above the Fermi surface. However, upon applying uniaxial strain along the [100] direction the filling is raised bringing the Fermi level to higher energy, traversing the vHS and inducing the so-called Lifshitz fransition [129]. At the same time, the superconducting transition is strongly enhanced due to the increase in the density of states. This was first reported by measuring the resistivity curves as a function of temperature for different applied strains and using elastoresistance measurements [130], similar to those $R \times \sigma_c$ we report here for ScV_6Sn_6. The Lifshitz transition was further confirmed by ARPES measurements under uniaxial strain. This transition identified by Lifshitz cannot be described by the common knowledge Landau theory of continuous phase transition, since there is no symmetry broken or long-range order associated to it. Instead, the Lifshitz transition is characterized as a topological transition, where the two different states (above and below the transition) maintain the same symmetry but with different Fermi surface topology.

In ScV_6Sn_6, whether the *c*-axis stress moves the Fermi level up or down (or do not move it at all) it is not known. However, if it does move, in any direction, there are two vHS which can be traversed, vHS1 which is above the Fermi level and vHS2, which its maximum is below the Fermi level. Considering one of these two cases, we can suggest another interpretation for our data. For all measured temperature range the resistance increases and peaks, followed by an abrupt decrease. Before the P^* appear, the inflection change occurs when we cross the CDW phase boundary. This is expected since the resistivity is smaller below CDW transition as seen in the $\rho(T)$ curves (Fig. 5.4A). In our measurements presented in figure 5.6A, the kink observed at P^* is very weak at higher temperatures and become more pronounced as we decrease the temperature. In ScV_6Sn_6, this enhanced scattering might be consistent with the Lifshitz transition scenario, since at higher temperatures the Fermi level may cross the vHS, but since the band is thermally activated the transition is smoothed. As we decrease the temperature, the CDW transtion is suppressed and inflection change in the $R \times \sigma_c$ mainly occur at P^*. Moreover, the P^* is almost temperature-independent for $T < 25$ K, which is expected since the thermal energy start to become much smaller and the transition will appear more sharply at the same pressure value. The enhancement of the $\Delta R/R_{\mathrm{min}}$ around $P \approx = 1$-1.2 GPa at low temperatures coincides with the emergence of P^* and it is a possible indication for a Lifshitz transition, such as observed in CsV_3Sb_5, where the superconductivity presents two domes in the pressure-temperature phase diagram, and the second dome is possibly associated to a Lifshitz transition enhancing the superconductivity [131, 132]. Similarly, in Sr_2RuO_4, the elastoresistance behavior in the normal state, show a peak at the Lifshitz transition, coinciding with the maximum of T_c [130]. in ScV_6Sn_6 the increase of the density of states containing Fermions with slow velocity or higher effective masses m^* produces a similar behavior. At low temperatures, $\rho_0 \propto m^*$, therefore, as the vHS is traversed by the Fermi level, the Fermions of the flat band will enhance the scattering rate.

In the second scenario T^* would be associated to a Lifshitz transition and not to the onset of the short-ranged CDW correlations. In such case, T^* and T_{CDW} would likely be uncorrelated, since the vHS seem to not be affected by the CDW at all. It is important to mention that either case one must to consider strain/stress inhomogeneities to play a degree of a role in those measurements. Thus, to confirm or rule out these scenarios different analysis must be done, such as new elastoresistance measurements, i.e., new $R \times \sigma_c$ curves in different specimens, to observe if the results are reproducible. First principles calculations for the electronic band structure considering the c axis reduction are also desirable. Additionally, structural measurements under c-axis uniaxial stress would be helpful to understand the evolution of the $\mathbf{q}_{\frac{1}{3}}$ and $\mathbf{q}_{\frac{1}{2}}$ correlations under this condition and confirm if the structure does not change abruptly at higher pressures.

5.4 Conclusion

In summary, our study revelaed that the out-of-plane component of the charge order dominates the phase transition and plays a crucial role in the CDW phase transition of ScV_6Sn_6. Thermal expansion measurements show a strong anisotropy among in-plane and out-of-plane coefficients. Applied uniaxial pressure along the c-axis rapidly suppresses the CDW transition, altering its characteristics from drop to hump-like feature at pressures $\sigma > \sigma_c = 1.05$ GPa. In comparison with the hydrostatic pressure the uniaxial pressure along the c-axis tune the CDW transition more rapidly, which is consistent since with the thermal expansion measurements, that revealed a higher strain sensitivity along c. The c-axis elatoresistance measurements exhibit two kinks, which we propose two potential scenarios to explain it. One associated with the competition between $\mathbf{q}_{\frac{1}{2}}$ and $\mathbf{q}_{\frac{1}{3}}$ CDW correlations and the second due to a putative Lifshitz transition, likely uncorrelated to the CDW transition. Further experiments using different specimens must be carried out to confirm these results. For example, X-ray diffraction experiments are highly desirable to fully comprehend the structural changes under c-axis stress. In this work, we explore for the first time the uniaxial pressure effect on the newly discovered CDW Kagome system ScV_6Sn_6. Moreover, we were able to successfully grow single crystals showing a rod-shape along the c-axis, which is an uncommon for hexagonal systems. We expect to explore this unique growth characteristic for future uniaxial pressure studies, probing the material properties beyond the electrical transport measurements, using this compound as a prototype to explore the interplay between CDW and nontrivial topology.

Chapter 6

Final considerations and perspectives

The uniaxial pressure technique has proven to be a powerful tool on unraveling the physics beyond the isotropic compression. The newly developed strain/stress apparatus, which nowadays is commercially available, can bring a whole new perspective on studying quantum materials, and the implementation of such field in laboratories here in Brazil is highly desirable. This technique has been already widely used by strong groups around the globe, in institutions such as Max-Planck-institut (Germany), Stanford University (USA) and the Los Alamos National Laboratory (USA), among others.

In this work, we explore the physical properties of two intermetallic compounds using uniaxial pressure as external tuning. On the $La_3Co_4Sn_{13}$, the axis selectivity of this technique revealed unusual behavior of the CDW and superconducting states for pressures applied along different directions. The superconducting state is suppressed at different rates depending on the direction of applied pressure. This is in contrast with the studies under hydrostatic pressure. The effects observed on the CDW transition is also intriguing. The upturn anomaly observed in resistivity measurements due to the CDW transition develops differently along the different directions, which might be correlated to the different suppresion rates observed for the superconductivity. Moreover, along the [110] direction, we observe a broader feature in $\rho(T)$, which is narrowed as the sample is compressed. This feature was confirmed by measuring two different samples. Since this direction is related to the CDW wavevector $\mathbf{q}_{CDW} = (0.5\ 0.5\ 0)$ in this compound, we proposed a possible scenario in which the change in the shape of the upturn could be correlated to different CDW degenerated domains that become aligned as the sample is cooled under stress. The same qualitative behavior is observed using the AC-ECE measurements as a thermodynamic probe.

Another part of this work was on exploring the CDW Kagome system ScV_6Sn_6. Using a capacitance dilatometer we measured linear thermal expansion measurements and we found a significant anisotropy between the in-plane and out-of-plane component of coefficients across the CDW transition. This suggested that the CDW should have a strong stress/strain sensitivity for pressures applied along the *c*-axis. We were able to successfully growth single-crystals of ScV_6Sn_6 with an unusual crystal shape for such hexagonal systems, displaying a long-rod along the *c*-axis, which makes the crystals highly suitable for measurements under uniaxial pressure. We perform electrical resistivity measurements under *c*-axis uniaxial stress, which rapidly suppresse the CDW transition and revealed a change in the CDW anomaly, from drop to hump-like in the temperature-dependent resistivity curves for pressures $\sigma_c > 1.05$ GPa. A second feature was also observed to develop in isotherm elastoresistance measurements, which become more pronounced at lower temperatures. We suggest two scenarios to explain the observed results, where this change in shape could be related to an alteration of the CDW wave vector, due to the highly unstable nature of the long-range CDW correlation in this material. On the other hand, we note that these results might also be consistent if the secondary feature is considered to be related to a Lifshitz transition, driven by the *c*-axis stress.

In summary, our results have shown that the uniaxial pressure tuning can reveal intricate physics and help us to understand possible hidden mechanisms in the materials. We have studied specifically systems displaying charge density waves, however, the uniaxial pressure approach can go much beyond charge order. It can give insight on diverse physics, such as magnetic and topological materials. It can be used beyond tuning parameter but also to investigate the coupling between lattice and electronic degrees of freedom.

As a future perspective, for $La_3Co_4Sn_{13}$ is desirable a comprehensive study to explore the domain physics of the CDW in this material. Techniques such as Dark-field X-ray Microscopy, can be useful to map the domains in a mesoscopic scale (see appendix A).

The compound ScV_6Sn_6 was discovered very recently, and became an ideal platform to study the interplay between CDW and nontrivial topology. There is a long path to completely unravel the origin of the CDW in this material. We expect to perform future investigations in this compound exploring the “out-of-plane growth” characteristic of this system found in this work.

Bibliography

[1] N. N. Wang, K. Y. Chen, Q. W. Yin, Y. N. N. Ma, B. Y. Pan, X. Yang, X. Y. Ji, S. L. Wu, P. F. Shan, S. X. Xu, et al., Competition between Charge-Density-Wave and Superconductivity in the Kagome Metal RbV_3Sb_5, Phys. Rev. Res. **3**, 043018 (2021).

[2] L. E. Klintberg, S. K. Goh, P. L. Alireza, P. J. Saines, D. A. Tompsett, P. W. Logg, J. Yang, B. Chen, K. Yoshimura, and F. M. Grosche, Pressure- and Composition-Induced Structural Quantum Phase Transition in the Cubic Superconductor $(\mathrm{Sr}, \mathrm{Ca})_3\mathrm{Ir}_4\mathrm{Sn}_{13}$, Phys. Rev. Lett. **109**, 237008 (2012).

[3] L. Mendonça-Ferreira, F. B. Carneiro, M. B. Fontes, E. Baggio-Saitovitch, L. S. I. Veiga, J. R. L. Mardegan, J. Strempfer, M. M. Piva, P. G. Pagliuso, R. D. dos Reis, et al., Pressure Effects on the Structural and Superconducting Transitions in La3Co4Sn13, Journal of Alloys and Compounds **773**, 34 (2019).

[4] J. Hou, K. Y. Chen, J. P. Sun, Z. Zhao, Y. H. Zhang, P. F. Shan, N. N. Wang, H. Zhang, K. Zhu, Y. Uwatoko, et al., Effect of Hydrostatic Pressure on the Unconventional Charge Density Wave and Superconducting Properties in Two Distinct Phases of Doped Kagome Superconductors $CsV_{3-x}Ti_xSb_5$, Phys. Rev. B **107**, 144502 (2023).

[5] F. H. Yu, D. H. Ma, W. Z. Zhuo, S. Q. Liu, X. K. Wen, B. Lei, J. J. Ying, and X. H. Chen, Unusual Competition of Superconductivity and Charge-Density-Wave State in a Compressed Topological Kagome Metal, Nat Commun **12**, 3645 (2021).

[6] J. Chang, E. Blackburn, A. T. Holmes, N. B. Christensen, J. Larsen, J. Mesot, R. Liang, D. A. Bonn, W. N. Hardy, A. Watenphul, et al., Direct Observation of Competition between Superconductivity and Charge Density Wave Order in YBa2Cu3O6.67, Nature Phys **8**, 871 (2012).

[7] C. Girod, C. R. Stevens, A. Huxley, E. D. Bauer, F. B. Santos, J. D. Thompson, R. M. Fernandes, J.-X. Zhu, F. Ronning, P. F. S. Rosa, et al., Thermodynamic and Electrical Transport Properties of UTe_2 under Uniaxial Stress, Phys. Rev. B **106**, L121101 (2022).

[8] F. Jerzembeck, H. S. Røising, A. Steppke, H. Rosner, D. A. Sokolov, N. Kikugawa, T. Scaffidi, S. H. Simon, A. P. Mackenzie, and C. W. Hicks, The Superconductivity of Sr2RuO4 under C-Axis Uniaxial Stress, Nat Commun **13**, 1 (2022).

[9] M. S. Ikeda, T. Worasaran, E. W. Rosenberg, J. C. Palmstrom, S. A. Kivelson, and I. R. Fisher, Elastocaloric Signature of Nematic Fluctuations, Proc. Natl. Acad. Sci. U.S.A. **118**, e2105911118 (2021).

[10] A. Sanna, C. Pellegrini, E. Liebhaber, K. Rossnagel, K. J. Franke, and E. K. U. Gross, Real-Space Anisotropy of the Superconducting Gap in the Charge-Density Wave Material 2H-NbSe2, Npj Quantum Mater. **7**, 1 (2022).

[11] L. Yue, A. R. Pokharel, J. Demsar, S. Zhang, Y. Li, T. Dong, and N. Wang, Highly Anisotropic Transient Optical Response of Charge Density Wave Order in $ZrTe_3$, Phys. Rev. B **107**, 165115 (2023).

[12] T. Qian, M. H. Christensen, C. Hu, A. Saha, B. M. Andersen, R. M. Fernandes, T. Birol, and N. Ni, Revealing the Competition between Charge Density Wave and Superconductivity in CsV_3Sb_5 through Uniaxial Strain, Phys. Rev. B **104**, 144506 (2021).

[13] C. W. Hicks, M. E. Barber, S. D. Edkins, D. O. Brodsky, and A. P. Mackenzie, Piezoelectric-Based Apparatus for Strain Tuning, Review of Scientific Instruments **85**, 065003 (2014).

[14] M. S. Ikeda, J. A. W. Straquadine, A. T. Hristov, T. Worasaran, J. C. Palmstrom, M. Sorensen, P. Walmsley, and I. R. Fisher, AC Elastocaloric Effect as a Probe for Thermodynamic Signatures of Continuous Phase Transitions, Review of Scientific Instruments **90**, 083902 (2019).

[15] J. A. W. Straquadine, M. S. Ikeda, and I. R. Fisher, Evidence for Realignment of the Charge Density Wave State in $ErTe_3$ and $TmTe_3$ under Uniaxial Stress via Elastocaloric and Elastoresistivity Measurements, Phys. Rev. X **12**, 021046 (2022).

[16] L. Ye, Y. Sun, V. Sunko, J. F. Rodriguez-Nieva, M. S. Ikeda, T. Worasaran, M. E. Sorensen, M. D. Bachmann, J. Orenstein, and I. R. Fisher, Elastocaloric Signatures of Symmetric and Antisymmetric Strain-Tuning of Quadrupolar and Magnetic Phases in DyB_2C_2, Proceedings of the National Academy of Sciences **120**, e2302800120 (2023).

[17] Y.-S. Li, M. Garst, J. Schmalian, S. Ghosh, N. Kikugawa, D. A. Sokolov, C. W. Hicks, F. Jerzembeck, M. S. Ikeda, Z. Hu, et al., Elastocaloric Determination of the Phase Diagram of Sr2RuO4, Nature **607**, 7918 (2022).

[18] Zhong, G., X. Lei, e J. Mao. Chemical Bonding, Electronic, and Magnetic Properties of $R_3Co_4Sn_{13}$ Intermetallics (R = La, Ce, Sm, Gd, and Tb): Density Functional Calculations. Physical Review B **79**, nº 9 (2009)

[19] H. W. S. Arachchige, W. R. Meier, M. Marshall, T. Matsuoka, R. Xue, M. A. McGuire, R. P. Hermann, H. Cao, and D. Mandrus, Charge Density Wave in Kagome Lattice Intermetallic ScV_6Sn_6, Phys. Rev. Lett. **129**, 216402 (2022).

[20] S. Cao, C. Xu, H. Fukui, T. Manjo, Y. Dong, M. Shi, Y. Liu, C. Cao, and Y. Song, Competing Charge-Density Wave Instabilities in the Kagome Metal ScV_6Sn_6, Nat Commun **14**, 1 (2023).

[21] R. E. Peierls, Quantum theory of solids. Oxford University Press (1955).

[22] H. Fröhlich, On the Theory of Superconductivity: The One-Dimensional Case, Proceedings of the Royal Society of London. Series A. Mathematical and Physical Sciences **223**, 296 (1997).

[23] G. Grüner, The Dynamics of Charge-Density Waves, Rev. Mod. Phys. **60**, 1129 (1988).

[24] M. D. Johannes and I. I. Mazin, Fermi Surface Nesting and the Origin of Charge Density Waves in Metals, Phys. Rev. B **77**, 165135 (2008).

[25] W. Kohn, Image of the Fermi Surface in the Vibration Spectrum of a Metal, Phys. Rev. Lett. **2**, 393 (1959).

[26] W. L. McMillan, Microscopic Model of Charge-Density Waves in $2H-\mathrm{TaSe}_2$, Phys. Rev. B **16**, 643 (1977).

[27] C. M. Varma and A. L. Simons, Strong-Coupling Theory of Charge-Density-Wave Transitions, Phys. Rev. Lett. **51**, 138 (1983).

[28] H. Li, T. T. Zhang, T. Yilmaz, Y. Y. Pai, C. E. Marvinney, A. Said, Q. W. Yin, C. S. Gong, Z. J. Tu, E. Vescovo, et al., Observation of Unconventional Charge Density Wave without Acoustic Phonon Anomaly in Kagome Superconductors AV_3Sb_5 (A = Rb, Cs), Phys. Rev. X **11**, 031050 (2021).

[29] X. Zhu, J. Guo, J. Zhang, and E. W. Plummer, Misconceptions Associated with the Origin of Charge Density Waves, Advances in Physics: X **2**, 622 (2017).

[30] C. A. Swenson, R. N. Shelton, P. Klavins, and H. D. Yang, Thermal-Expansion Measurements for $Lu_5Ir_4Si_{10}$, $Lu_5Rh_4Si_{10}$, Sc_5 Ir_4Si_{10}, and $Tm_5Ir_4Si_{10}$: Charge-Density-Wave Effects, Phys. Rev. B **43**, 7668 (1991).

[31] C. S. Lue, H. F. Liu, B. D. Ingale, J. N. Li, and Y. K. Kuo, Transport, Thermoelectric, and Thermal Expansion Investigations of the Cage Structure Compound $CeOs_2Al_{10}$, Phys. Rev. B **85**, 245116 (2012).

[32] R. Gupta, A. Thamizhavel, P. Rodière, S. Nandi, K. P. Rajeev, and Z. Hossain, Electrical Resistivity under Pressure and Thermal Expansion of $LaPt_2Si_2$ Single Crystal, Journal of Applied Physics **125**, 143902 (2019).

[33] S. L. Bud'ko, S. A. Law, P. C. Canfield, G. D. Samolyuk, M. S. Torikachvili, and G. M. Schmiedeshoff, Thermal Expansion and Magnetostriction of Pure

and Doped $RAgSb_2$ (R = Y, Sm, La) Single Crystals, J. Phys.: Condens. Matter **20**, 115210 (2008).

[34] H. K. Onnes, The Superconductivity of Mercury. Comm. Phys. Lab. Univ., Leiden, 122-124 (1911).

[35] W. Meissner and R. Ochsenfeld, Naturwissenschaften 21, 787 (1933); for English translation see A. M. Forrest, Eur. J. Phys. **4**, 117 (1983).

[36] F. London, H. London, and F. A. Lindemann, The Electromagnetic Equations of the Supraconductor, Proceedings of the Royal Society of London. Series A - Mathematical and Physical Sciences **149**, 71 (1997).

[37] J. Bardeen, L. N. Cooper, and J. R. Schrieffer, Theory of Superconductivity, Phys. Rev. **108**, 1175 (1957).

[38] A. A. Abrikosov, The Magnetic Properties of Superconducting Alloys, Journal of Physics and Chemistry of Solids **2**, 199 (1957).

[39] G. R. Stewart, Unconventional Superconductivity, Advances in Physics **66**, 75 (2017).

[40] F. Beer, J. E. Russell Johnston, J. DeWolf, and D. Mazurek, Mechanics of Materials, 5th edition (McGraw-Hill Science/Engineering/Math, New York, 2008).

[41] M. Rabiei, A. Palevicius, A. Dashti, S. Nasiri, A. Monshi, A. Vilkauskas, and G. Janusas, Measurement Modulus of Elasticity Related to the Atomic Density of Planes in Unit Cell of Crystal Lattices, Materials **13**, 19 (2020).

[42] J. F. Nye, Physical Properties of Crystals: Their Representation by Tensors and Matrices, 1st published in pbk. with corrections, 1984 (Clarendon press; Oxford University Press, Oxford) [Oxfordshire], New York (1984).

[43] Fisk, Z., & Remeika, J. P, Chapter 81 Growth of single crystals from molten metal fluxes. Handbook on the Physics and Chemistry of Rare Earths, 53–70 (1989). .

[44] Canfield, P. C., & Fisk, Z, Growth of single crystals from metallic fluxes. Philosophical Magazine B, **65(6)**, 1117–1123 (1992).

[45] T. Hu, H. Pi, S. Xu, L. Yue, Q. Wu, Q. Liu, S. Zhang, R. Li, X. Zhou, J. Yuan, et al., Optical Spectroscopy and Band Structure Calculations of the Structural Phase Transition in the Vanadium-Based Kagome Metal ScV_6Sn_6, Phys. Rev. B **107**, 165119 (2023).

[46] Z. Guguchia, D. J. Gawryluk, S. Shin, Z. Hao, C. Mielke III, D. Das, I. Plokhikh, L. Liborio, J. K. Shenton, Y. Hu, et al., Hidden Magnetism Uncovered in a Charge Ordered Bilayer Kagome Material ScV6Sn6, Nat Commun **14**, 1 (2023).

[47] C. Yi, X. Feng, N. Mao, P. Yanda, S. Roychowdhury, Y. Zhang, C. Felser, and C. Shekhar, Quantum Oscillations Revealing Topological Band in Kagome Metal ScV_6Sn_6, Phys. Rev. B **109**, 035124 (2024).

[48] J. R. Collave, H. A. Borges, S. M. Ramos, E. N. Hering, M. B. Fontes, E. Baggio-Saitovitch, L. Mendonça-Ferreira, E. M. Bittar, and P. G. Pagliuso, Heavy Fermion Ce3Co4Sn13 Compound under Pressure, Journal of Applied Physics **117**, 17E307 (2015).

[49] H. F. Liu, C. N. Kuo, C. S. Lue, K.-Z. Syu, and Y. K. Kuo, Partially Gapped Fermi Surfaces in $La_3Co_4Sn_{13}$ Revealed by Nuclear Magnetic Resonance, Phys. Rev. B **88**, 115113 (2013).

[50] Y. W. Cheung, J. Z. Zhang, J. Y. Zhu, W. C. Yu, Y. J. Hu, D. G. Wang, Y. Otomo, K. Iwasa, K. Kaneko, M. Imai, et al., Second-Order Structural Transition in Superconductor $La_3Co_4Sn_{13}$, Phys. Rev. B **93**, 241112 (2016).

---

[51] PPMS Heat Capacity Option User's Manual, 1085-150, Rev. M0, January 2004.

[52] C. Kittel, Introduction to Solid State Physics (Wiley, 2004).

[53] G. M. Schmiedeshoff, A. W. Lounsbury, D. J. Luna, S. J. Tracy, A. J. Schramm, S. W. Tozer, V. F. Correa, S. T. Hannahs, T. P. Murphy, E. C. Palm, et al., Versatile and Compact Capacitive Dilatometer, Review of Scientific Instruments **77**, 123907 (2006).

[54] Razorbill instruments application note. "AP007: Force or Displacement?". https://razorbillinstruments.com/.

[55] Razorbill instruments application note. "AP006: Capacitive sensor performance". https://razorbillinstruments.com/.

[56] M. E. Barber, Uniaxial Stress Technique and Investigations into Correlated Electron Systems, Doctoral thesis, University of St Andrews (2017).

[57] C. E. Ojeda, E. J. Oakes, J. R. Hill, D. Aldi, and G. A. Forsberg, Temperature Effects on Adhesive Bond Strengths and Modulus for Commonly Used Spacecraft Stuctural Adhesives, http://dataverse.jpl.nasa.gov/dataset.xhtml?persistentId=hdl:2014/42025.

[58] A. Lim, New Technique Clearly Reveals Signatures of Subtle Electronic Phase Transitions, Scilight 2019, 320001 (2019).

[59] L. S. I. Veiga, J. R. L. Mardegan, M. V. Zimmermann, D. T. Maimone, F. B. Carneiro, M. B. Fontes, J. Strempfer, E. Granado, P. G. Pagliuso, and E. M. Bittar, Possible Quantum Fluctuations in the Vicinity of the Quantum Critical Point of (Sr , Ca) 3 Ir 4 Sn 13 Revealed by High-Energy x-Ray Diffraction, Phys. Rev. B **101**, 104511 (2020).

[60] S. K. Goh, D. A. Tompsett, P. J. Saines, H. C. Chang, T. Matsumoto, M. Imai, K. Yoshimura, and F. M. Grosche, Ambient Pressure Structural Quantum Critical Point in the Phase Diagram of $(\mathrm{Ca}_x\mathrm{Sr}_{1-x})_3\mathrm{Rh}_4\mathrm{Sn}_{13}$, Phys. Rev. Lett. **114**, 097002 (2015).

[61] C. Israel, E. M. Bittar, O. E. Agüero, R. R. Urbano, C. Rettori, I. Torriani, P. G. Pagliuso, N. O. Moreno, J. D. Thompson, M. F. Hundley, et al., Crystal Structure and Low-Temperature Physical Properties of RMSn Intermetallics, Physica B: Condensed Matter 359–361, 251 (2005).

[62] H. F. Liu, C. N. Kuo, C. S. Lue, K.-Z. Syu, and Y. K. Kuo, Partially Gapped Fermi Surfaces in $La_3Co_4Sn_{13}$ Revealed by Nuclear Magnetic Resonance, Phys. Rev. B **88**, 115113 (2013).

[63] H.-T. Wang, M. K. Srivastava, C.-C. Wu, S.-H. Hsieh, Y.-F. Wang, Y.-C. Shao, Y.-H. Liang, C.-H. Du, J.-W. Chiou, C.-M. Cheng, et al., Electronic and Atomic Structures of the Sr3Ir4Sn13 Single Crystal: A Possible Charge Density Wave Material, Sci Rep **7**, 1 (2017).

[64] J. Choi, Q. Wang, S. Jöhr, N. B. Christensen, J. Küspert, D. Bucher, D. Biscette, M. H. Fischer, M. Hücker, T. Kurosawa, et al., Unveiling Unequivocal Charge Stripe Order in a Prototypical Cuprate Superconductor, Phys. Rev. Lett. **128**, 207002 (2022).

[65] A. Haas, D. Wichert, G. Bruls, B. Lüthi, G. Balakrishnan, and D. McK. Paul, Elastic Properties of Superconducting Stannides: $Yb_3Rh_4Sn_{13}$ and $Ca_3Rh_4Sn_{13}$, Journal of Low Temperature Physics **114**, 285 (1999).

[66] A. V. Narlikar, editor , Frontiers in Superconducting Materials (Springer, Berlin Heidelberg, 2005).

[67] G. Zhong, X. Lei, and J. Mao, Chemical Bonding, Electronic, and Magnetic Properties of R 3Co4Sn13 Intermetallics (R = La , Ce, Sm, Gd, and Tb): Density Functional Calculations, Phys. Rev. B **79**, 094424 (2009).

[68] Y. W. Cheung, J. Z. Zhang, J. Y. Zhu, W. C. Yu, Y. J. Hu, D. G. Wang, Y. Otomo, K. Iwasa, K. Kaneko, M. Imai, et al., Second-Order Structural Transition in the Superconductor La3Co4Sn 13, Phys. Rev. B **93**, 241112 (2016).

[69] G. M. Eliashberg, Soviet Phys.-JEPT 11, 696 (1960); **12**, 1000 (1961).

[70] W. L. McMillan, Transition Temperature of Strong-Coupled Superconductors, Phys. Rev. **167**, 331 (1968).

[71] W.-H. Ko, P. A. Lee, and X.-G. Wen, Doped Kagome System as Exotic Superconductor, Phys. Rev. B **79**, 214502 (2009).

[72] Liu Zheng, Liu Feng, and Wu Yong-Shi, Exotic Electronic States in the World of Flat Bands: From Theory to Material, Chinese Phys. B **23**, 077308 (2014).

[73] H.-M. Guo and M. Franz, Topological Insulator on the Kagome Lattice, Phys. Rev. B **80**, 113102 (2009).

[74] M. Kang, L. Ye, S. Fang, J.-S. You, A. Levitan, M. Han, J. I. Facio, C. Jozwiak, A. Bostwick, E. Rotenberg, *et al.*, Dirac Fermions and Flat Bands in the Ideal Kagome Metal FeSn, Nat. Mater. **19**, 2 (2020).

[75] H. Yang, Y. Sun, Y. Zhang, W.-J. Shi, S. S. P. Parkin, and B. Yan, Topological Weyl Semimetals in the Chiral Antiferromagnetic Materials Mn3Ge and Mn3Sn, New J. Phys. **19**, 015008 (2017).

[76] L. Ye, M. Kang, J. Liu, F. von Cube, C. R. Wicker, T. Suzuki, C. Jozwiak, A. Bostwick, E. Rotenberg, D. C. Bell, *et al.*, Massive Dirac Fermions in a Ferromagnetic Kagome Metal, Nature **555**, 7698 (2018).

[77] Y. Luo, Y. Han, J. Liu, H. Chen, Z. Huang, L. Huai, H. Li, B. Wang, J. Shen, S. Ding, *et al.*, A Unique van Hove Singularity in Kagome Superconductor $\mathrm{CsV}_{3-x}\mathrm{Ta}_x\mathrm{Sb}_5$ with Enhanced Superconductivity, Nat Commun **14**, 1 (2023).

[78] X. Han, A. P. Schnyder, and X. Wu, Enhanced Nematicity Emerging from Higher-Order Van Hove Singularities, Phys. Rev. B **107**, 184504 (2023).

[79] L. Kautzsch, Y. M. Oey, H. Li, Z. Ren, B. R. Ortiz, G. Pokharel, R. Seshadri, J. Ruff, T. Kongruengkit, J. W. Harter, *et al.*, Incommensurate Charge-Stripe Correlations in the Kagome Superconductor $\mathrm{CsV}_3\mathrm{Sb}_{5-x}\mathrm{Sn}_x$, Npj Quantum Mater. **8**, 1 (2023).

[80] X. Teng, L. Chen, F. Ye, E. Rosenberg, Z. Liu, J.-X. Yin, Y.-X. Jiang, J. S. Oh, M. Z. Hasan, K. J. Neubauer, *et al.*, Discovery of Charge Density Wave in a Kagome Lattice Antiferromagnet, Nature **609**, 7927 (2022).

[81] H. Li, D. Oh, M. Kang, H. Zhao, B. R. Ortiz, Y. Oey, S. Fang, Z. Ren, C. Jozwiak, A. Bostwick, *et al.*, Small Fermi Pockets Intertwined with Charge Stripes and Pair Density Wave Order in a Kagome Superconductor, Phys. Rev. X **13**, 031030 (2023).

[82] W.-S. Wang, Z.-Z. Li, Y.-Y. Xiang, and Q.-H. Wang, Competing Electronic Orders on Kagome Lattices at van Hove Filling, Phys. Rev. B **87**, 115135 (2013).

[83] Y.-P. Lin and R. M. Nandkishore, Complex Charge Density Waves at Van Hove Singularity on Hexagonal Lattices: Haldane-Model Phase Diagram and Potential Realization in the Kagome Metals AV_3Sb_5 (A=K, Rb, Cs), Phys. Rev. B **104**, 045122 (2021).

.

[84] J. M. DeStefano, E. Rosenberg, O. Peek, Y. Lee, Z. Liu, Q. Jiang, L. Ke, and J.-H. Chu, Pseudogap Behavior in Charge Density Wave Kagome Material ScV6Sn6 Revealed by Magnetotransport Measurements, Npj Quantum Mater. 8, 1 (2023).

[85] G. Venturini, B. C. E. Idrissi, and B. Malaman, Magnetic Properties of RMn6Sn6 (R = Sc, Y, Gd-Tm, Lu) Compounds with HfFe6Ge6 Type Structure, Journal of Magnetism and Magnetic Materials **94**, 35 (1991).

[86] H. Zhang, X. Feng, T. Heitmann, A. I. Kolesnikov, M. B. Stone, Y.-M. Lu, and X. Ke, Topological Magnon Bands in a Room-Temperature Kagome Magnet, Phys. Rev. B **101**, 100405 (2020).

[87] H. Ishikawa, T. Yajima, M. Kawamura, H. Mitamura, and K. Kindo, GdV6Sn6: A Multi-Carrier Metal with Non-Magnetic 3d-Electron Kagome Bands and 4f-Electron Magnetism, J. Phys. Soc. Jpn. **90**, 124704 (2021).

[88] N. J. Ghimire, R. L. Dally, L. Poudel, D. C. Jones, D. Michel, N. T. Magar, M. Bleuel, M. A. McGuire, J. S. Jiang, J. F. Mitchell, *et al.*, Competing Magnetic Phases and Fluctuation-Driven Scalar Spin Chirality in the Kagome Metal YMn6Sn6, Science Advances **6**, eabe2680 (2020).

[89] E. Rosenberg, J. M. DeStefano, Y. Guo, J. S. Oh, M. Hashimoto, D. Lu, R. J. Birgeneau, Y. Lee, L. Ke, M. Yi, et al., Uniaxial Ferromagnetism in the Kagome Metal TbV_6Sn_6, Phys. Rev. B **106**, 115139 (2022).

[90] S. X. M. Riberolles, T. J. Slade, D. L. Abernathy, G. E. Granroth, B. Li, Y. Lee, P. C. Canfield, B. G. Ueland, L. Ke, and R. J. McQueeney, Low-Temperature Competing Magnetic Energy Scales in the Topological Ferrimagnet $TbMn_6Sn_6$, Phys. Rev. X **12**, 021043 (2022).

[91] T. Asaba, S. M. Thomas, M. Curtis, J. D. Thompson, E. D. Bauer, and F. Ronning, Anomalous Hall Effect in the Kagome Ferrimagnet $GdMn_6Sn_6$, Phys. Rev. B **101**, 174415 (2020).

[92] G. Pokharel, B. Ortiz, J. Chamorro, P. Sarte, L. Kautzsch, G. Wu, J. Ruff, and S. D. Wilson, Highly Anisotropic Magnetism in the Vanadium-Based Kagome Metal TbV_6Sn_6, Phys. Rev. Mater. **6**, 104202 (2022).

[93] G. Pokharel, S. M. L. Teicher, B. R. Ortiz, P. M. Sarte, G. Wu, S. Peng, J. He, R. Seshadri, and S. D. Wilson, Electronic Properties of the Topological Kagome Metals YV_6Sn_6 and GdV_6Sn_6, Phys. Rev. B **104**, 235139 (2021).

[94] X. Xu, J.-X. Yin, W. Ma, H.-J. Tien, X.-B. Qiang, P. V. S. Reddy, H. Zhou, J. Shen, H.-Z. Lu, T.-R. Chang, *et al.*, Topological Charge-Entropy Scaling in Kagome Chern Magnet TbMn6Sn6, Nat Commun **13**, 1 (2022).

[95] H. Tan, Y. Liu, Z. Wang, and B. Yan, Charge Density Waves and Electronic Properties of Superconducting Kagome Metals, Phys. Rev. Lett. **127**, 046401 (2021).

[96] B. R. Ortiz, S. M. L. Teicher, L. Kautzsch, P. M. Sarte, N. Ratcliff, J. Harter, J. P. C. Ruff, R. Seshadri, and S. D. Wilson, Fermi Surface Mapping and the Nature of Charge-Density-Wave Order in the Kagome Superconductor CsV_3Sb_5, Phys. Rev. X **11**, 041030 (2021).

[97] B. R. Ortiz, S. M. L. Teicher, Y. Hu, J. L. Zuo, P. M. Sarte, E. C. Schueller, A. M. M. Abeykoon, M. J. Krogstad, S. Rosenkranz, R. Osborn, *et al.*, CsV_3Sb_5: A Z_2 Topological Kagome Metal with a Superconducting Ground State, Phys. Rev. Lett. **125**, 247002 (2020).

[98] K. Jiang, T. Wu, J.-X. Yin, Z. Wang, M. Z. Hasan, S. D. Wilson, X. Chen, and J. Hu, Kagome Superconductors AV3Sb5 (A = K, Rb, Cs), National Science Review **10**, nwac199 (2023).

[99] R. Gupta, D. Das, C. Mielke, E. T. Ritz, F. Hotz, Q. Yin, Z. Tu, C. Gong, H. Lei, T. Birol, *et al.*, Two Types of Charge Order with Distinct Interplay with Superconductivity in the Kagome Material CsV3Sb5, Commun Phys **5**, 1 (2022).

[100] Y.-X. Jiang, J.-X. Yin, M. M. Denner, N. Shumiya, B. R. Ortiz, G. Xu, Z. Guguchia, J. He, M. S. Hossain, X. Liu, *et al.*, Unconventional Chiral Charge Order in Kagome Superconductor KV3Sb5, Nat. Mater. **20**, 10 (2021).

[101] X. Zhang, J. Hou, W. Xia, Z. Xu, P. Yang, A. Wang, Z. Liu, J. Shen, H. Zhang, X. Dong, *et al.*, Destabilization of the Charge Density Wave and the Absence of Superconductivity in ScV_6Sn_6 under High Pressures up to 11 GPa, Materials **15**, 20 (2022).

[102] S. Mozaffari, W. R. Meier, R. P. Madhogaria, N. Peshcherenko, S.-H. Kang, J. W. Villanova, H. W. S. Arachchige, G. Zheng, Y. Zhu, K.-W. Chen, *et al.*, Universal Sublinear Resistivity in Vanadium Kagome Materials Hosting Charge Density Waves, arXiv:2305.02393 (2023).

[103] C. Yi, X. Feng, P. Yanda, S. Roychowdhury, C. Felser, and C. Shekhar, Charge Density Wave Induced Anomalous Hall Effect in Kagome ScV_6Sn_6, arXiv:2305.04683 (2023).

[104] Z. Guguchia, D. J. Gawryluk, S. Shin, Z. Hao, C. Mielke III, D. Das, I. Plokhikh, L. Liborio, J. K. Shenton, Y. Hu, *et al.*, Hidden Magnetism Uncovered in a Charge Ordered Bilayer Kagome Material ScV_6Sn_6, Nat Commun **14**, 1 (2023).

[105] H. Li, S. Wan, Han Li, Q. Li, Q. Gu, H. Yang, Y. Li, Z. Wang, Y. Yao, and H.-H. Wen, No Observation of Chiral Flux Current in the Topological Kagome Metal CsV_3Sb_5, Phys. Rev. B **105**, 045102 (2022).

[106] D. R. Saykin, C. Farhang, E. D. Kountz, D. Chen, B. R. Ortiz, C. Shekhar, C. Felser, S. D. Wilson, R. Thomale, J. Xia, *et al.*, High Resolution Polar Kerr Effect Studies of CsV_3Sb_5: Tests for Time-Reversal Symmetry Breaking below the Charge-Order Transition, Phys. Rev. Lett. **131**, 016901 (2023).

[107] A. Korshunov, H. Hu, D. Subires, Y. Jiang, D. Calugaru, X. Feng, A. Rajapitamahuni, C. Yi, S. Roychowdhury, M. G. Vergniory, *et al.*, Softening of a Flat Phonon Mode in the Kagome ScV_6Sn_6, Nat Commun 14, 1 (2023).

[108] H. Tan and B. Yan, Abundant Lattice Instability in Kagome Metal ScV_6Sn_6, Phys. Rev. Lett. **130**, 266402 (2023).

[109] S. Lee, C. Won, J. Kim, J. Yoo, S. Park, J. Denlinger, C. Jozwiak, A. Bostwick, E. Rotenberg, R. Comin, *et al.*, Nature of Charge Density Wave in Kagome Metal ScV6Sn6, Npj Quantum Mater. **9**, 1 (2024).

[110] M. Tuniz, A. Consiglio, D. Puntel, C. Bigi, S. Enzner, G. Pokharel, P. Orgiani, W. Bronsch, F. Parmigiani, V. Polewczyk, *et al.*, Dynamics and Resilience of the Unconventional Charge Density Wave in ScV_6Sn_6 Bilayer Kagome Metal, Commun Mater **4**, 1 (2023).

[111] K. Momma and F. Izumi, VESTA 3 for Three-Dimensional Visualization of Crystal, Volumetric and Morphology Data, J Appl Cryst **44**, 1272 (2011).

[112] M. Kang, S. Fang, J.-K. Kim, B. R. Ortiz, S. H. Ryu, J. Kim, J. Yoo, G. Sangiovanni, D. Di Sante, B.-G. Park, et al., Twofold van Hove Singularity and Origin of Charge Order in Topological Kagome Superconductor CsV3Sb5, Nat. Phys. *18*, 3 (2022).

[113] S. Cho, H. Ma, W. Xia, Y. Yang, Z. Liu, Z. Huang, Z. Jiang, X. Lu, J. Liu, Zhonghao Liu, et al., Emergence of New van Hove Singularities in the Charge Density Wave State of a Topological Kagome Metal RbV_3Sb_5, Phys. Rev. Lett. **127**, 236401 (2021).

[114] G. Pokharel, B. R. Ortiz, L. Kautzsch, S. J. Gomez Alvarado, K. Mallayya, G. Wu, E.-A. Kim, J. P. C. Ruff, S. Sarker, and S. D. Wilson, Frustrated

Charge Order and Cooperative Distortions in ScV_6Sn_6, Phys. Rev. Materials **7**, 104201 (2023).

[115] A. Subedi, Order-by-Disorder Charge Density Wave Condensation at $q = (\frac{1}{3}, \frac{1}{3}, \frac{1}{3})$ in Kagome Metal ScV_6Sn_6, Phys. Rev. Materials **8**, 014006 (2024).

[116] A. Chubukov, Order from Disorder in a Kagomé Antiferromagnet, Phys. Rev. Lett. **69**, 832 (1992).

[117] E. Gati, L. Xiang, S. L. Bud'ko, and P. C. Canfield,Hydrostatic and Uniaxial Pressure Tuning of Iron-Based Superconductors: Insights into Superconductivity, Magnetism, Nematicity, and Collapsed Tetragonal Transitions, Annalen Der Physik **532**, 2000248 (2020).

[118] F. Jerzembeck, H. S. Røising, A. Steppke, H. Rosner, D. A. Sokolov, N. Kikugawa, T. Scaffidi, S. H. Simon, A. P. Mackenzie, and C. W. Hicks, The Superconductivity of Sr_2RuO_4 under c-Axis Uniaxial Stress, Nat Commun **13**, 1 (2022).

[119] C. Girod, C. R. Stevens, A. Huxley, E. D. Bauer, F. B. Santos, J. D. Thompson, R. M. Fernandes, J.-X. Zhu, F. Ronning, P. F. S. Rosa, *et al.*, Thermodynamic and Electrical Transport Properties of UTe_2 under Uniaxial Stress, Phys. Rev. B **106**, L121101 (2022).

[120] H.-H. Kim, S. M. Souliou, M. E. Barber, E. Lefrançois, M. Minola, M. Tortora, R. Heid, N. Nandi, R. A. Borzi, G. Garbarino, *et al.*, Uniaxial Pressure Control of Competing Orders in a High-Temperature Superconductor, Science **362**, 1040 (2018).

[121] J. A. W. Straquadine, M. S. Ikeda, and I. R. Fisher, Evidence for Realignment of the Charge Density Wave State in $ErTe_3$ and $TmTe_3$ under Uniaxial Stress via Elastocaloric and Elastoresistivity Measurements, Phys. Rev. X **12**, 021046 (2022).

[122] T. Qian, M. H. Christensen, C. Hu, A. Saha, B. M. Andersen, R. M. Fernandes, T. Birol, and N. Ni, Revealing the Competition between Charge Density Wave

and Superconductivity in CsV_3Sb_5 through Uniaxial Strain, Phys. Rev. B **104**, 144506 (2021).

[123] M. Frachet, L. Wang, W. Xia, Y. Guo, M. He, N. Maraytta, R. Heid, A.-A. Haghighirad, M. Merz, C. Meingast, et al., Colossal C-Axis Response and Lack of Rotational Symmetry Breaking within the Kagome Plane of the CsV_3Sb_5 Superconductor, arXiv:2310.06102.

[124] C. Yi, X. Feng, N. Kumar, C. Felser, and C. Shekhar, Tuning Charge Density Wave of Kagome Metal ScV6Sn6, arXiv:2403.02463 (2024).

[125] N. A. Lanzillo, J. B. Thomas, B. Watson, M. Washington, and S. K. Nayak, Pressure-Enabled Phonon Engineering in Metals, Proceedings of the National Academy of Sciences **111**, 8712 (2014).

[126] K. Miyake, O. Narikiyo, and Y. Onishi, Superconductivity of Ce-Based Heavy Fermions under Pressure: Valence Fluctuation Mediated Pairing Associated with Valence Instability of Ce, Physica B: Condensed Matter 259-261, **676** (1999).

[127] Y. Hu, J. Ma, Y. Li, Y. Jiang, D. J. Gawryluk, T. Hu, J. Teyssier, V. Multian, Z. Yin, S. Xu, et al., Phonon Promoted Charge Density Wave in Topological Kagome Metal ScV6Sn6, Nat Commun 15, 1658 (2024).

[128] S. Mozaffari, W. R. Meier, R. P. Madhogaria, N. Peshcherenko, S.-H. Kang, J. W. Villanova, H. W. S. Arachchige, G. Zheng, Y. Zhu, K.-W. Chen, et al., Universal Sublinear Resistivity in Vanadium Kagome Materials Hosting Charge Density Waves, arXiv:2305.02393.

[129] M. Lifshitz, ANOMALIES OF ELECTRON CHARACTERISTICS OF A METAL IN THE HIGH PRESSURE REGION, (n.d.).

[130] M. E. Barber, A. S. Gibbs, Y. Maeno, A. P. Mackenzie, and C. W. Hicks, Resistivity in the Vicinity of a van Hove Singularity: Sr_2RuO_4 under Uniaxial Pressure, Phys. Rev. Lett. **120**, 076602 (2018).

[131] F. H. Yu, D. H. Ma, W. Z. Zhuo, S. Q. Liu, X. K. Wen, B. Lei, J. J. Ying, and X. H. Chen, Unusual Competition of Superconductivity and Charge-Density-Wave State in a Compressed Topological Kagome Metal, Nat Commun **12**, 3645 (2021).

[132] Z. Zhang, Z. Chen, Y. Zhou, Y. Yuan, S. Wang, J. Wang, H. Yang, C. An, L. Zhang, X. Zhu, et al., Pressure-Induced Reemergence of Superconductivity in the Topological Kagome Metal CsV_3Sb_5, Phys. Rev. B **103**, 224513 (2021).

Appendix A

Full-field imaging of the charge density wave structure using Dark-field X-ray microscopy (DFXM)

Acknowledgment

In this appendix of the thesis, I would like to extend special thanks to Zahir Islam (Scientist and beamline staff at 6ID-C - Advanced Photon Source), Elliot Kisiel (PhD student at the University of California - San Diego), and Jayden Plumb (PhD student at the University of California - Santa Barbara). Their wealth experience with DFXM has been invaluable in assisting me during the experiments and guiding me through data analysis in our bi-weekly meetings (creatively named “DFXM Therapy”). Additionally, I am grateful to the 6-ID-C beamline for being the pioneering platform for low-temperature DFXM studies, and I appreciate the opportunity to participate in various challenging experiments conducted there.

Abstract

Charge density waves (CDW) are a collective phenomenon where below a certain transition temperature T_{CDW}, there is a modulation of the conduction electrons accompanied by a distortion in the crystalline lattice. Experimental signatures of CDW can be observed even in macroscopic measurements such as thermal and electrical transport, as well as X-ray diffraction, where new reflections appear in the diffraction pattern below T_{CDW}. CDW often emerge in systems that also exhibit superconductivity, coexisting and/or competing with the superconducting state, raising the question of the role of CDW in the formation and stabilization of the superconducting state. This work aims to explore the formation of charge density wave domains in order to enrich the knowledge about this fundamental state, as well as its possible implications for the emergence of the superconducting state. Here, X-ray diffraction and dark-field X-ray microscopy (DFXM) were used as the main techniques. Using these techniques, we hope to explore and characterize the mesoscopic and macroscopic properties of CDW in the intermetallic compound $Sr_{0.4}Ca_{0.6}Rh_4Sn_{13}$ and its possible connection with the superconducting state.

Introuction

Charge density waves are characterized by the periodic modulation of conduction electrons and are frequently observed in various materials. This fundamental state can have a significant influence on the physical properties of a material; therefore, characterizing and understanding this phenomenon is of great interest in the scientific community. Experimentally, such transitions can be macroscopically characterized using specific heat, magnetization, electrical resistivity, among other transport and thermodynamic measurements. However, due to the way they are performed, these measurements result in average information of these quantities and may hide important details that occur on the mesoscopic scale. CDW can connect with intrinsic and extrinsic degrees of freedom within a material. For example, the spatial distribution and formation of CDW domains can occur in different ways and on different scales depending on the internal structure of the material.

The spatial characterization of CDW is generally performed using microscopy techniques. Among them, scanning tunneling microscopy (STM) and transmission electron microscopy (TEM) [1, 2, 3] are notable. However, despite being extremely powerful techniques for observing electronic modulation, they are limited to fields of view of a few hundred nanometers and are primarily sensitive to the surface of materials, extremely thin samples, or are destructive in nature. Such conditions often do not represent the mesoscopic or macroscopic nature of the material, making it difficult to connect with the macroscopic physical properties of the system under study. Therefore, the search for techniques that enable the study of materials on a mesoscopic or even macroscopic scale has become a necessity in the academic community of materials science.

The technique called Dark-field X-ray microscopy (DFXM) has shown promise for structural characterization of materials on multiple scales. DFXM is an X-ray microscopy technique performed in synchrotron laboratories. However, it is relatively new, and its first dedicated beamline was implemented in 2019 at the European Synchrotron Radiation Facility (ESRF) in Grenoble, France [4]. Since then, at this laboratory, DFXM has been primarily used to characterize defects in crystals [5], formation of ferroelectric domains [6], and even the microstructure of biominerals [7]. A DFXM microscope can produce images on scales ranging from nanometers to hundreds of micrometers and, because it uses X-rays, is a non-destructive technique for most solids. This technique was recently implemented at the 6-ID-C beamline of the Advanced Photon Source (APS) in Illinois, USA, where this work was conducted. Unlike the ESRF, this beamline focuses on applying the technique in sample environments with access to low temperatures and static and pulsed magnetic fields, being the first beamline to enable the use of DFXM under these conditions [8, 9, 10, 11].

In this work we use of DFXM to characterize, for the first time on a mesoscopic scale, the charge density wave structure of an intermetallic system using a Bulk sensitive probe. For this purpose, the prototype system chosen was a material previously studied in our research group at the Brazilian Center for Physics Research (CBPF). The studied compound was $\mathrm{Sr_{0.4}Ca_{0.6}Rh_4Sn_{13}}$, which belongs to the family of $\mathrm{R_3T_4Sn_{13}}$ compounds (R = rare earth or alkaline earth metal, T = transition metal), which exhibit a wide range of physical properties, including charge density waves [12, 13, 14]. This compound undergoes a CDW transition around $T_{CDW} \sim 40$

K and a superconducting transition at $T_c \sim 7.5$ K [13]. The main objective of this study is to observe, on a Bulk mesoscopic scale, the formation of the CDW using DFXM images and to observe how the charge ordering domain structure connects with the primitive internal structure of the material and its relation to intrinsic defects in the crystalline structure. Additionally, with the possibility of studies at temperatures below T_c, we can observe if there is any change in the distribution of CDW domains within the superconducting state, which may indicate the correlation of CDW domains with superconductivity stabilization. Besides the scientific problem, since it is a newly developed and little-applied technique for low-temperature systems, this work allows us to explore its limitations and contribute to its development.

Domain structure in CDW

Charge density waves in real materials exhibit long-range structure. The formation of this structure is generally non-uniform and can unfold into different domains within the material, consequently altering its physical properties. In this section, we will describe some examples of materials where CDW domains have been observed and their implications for their physical properties. Most of these materials are of low dimensionality (quasi-1D or 2D), and studies of CDW in 3D materials are scarce due to their complexity and the absence of examples of CDW in higher dimensions. One example of a low-dimensional material class that exhibits CDW is transition metal dichalcogenides. Among their varieties, many show charge ordering where there is a breaking of translational symmetry both by the conduction electrons and the crystalline structure. Studies of domains in these compounds are abundant in the literature. In particular, the compound 1T-TaS$_2$, classified as quasi-bidimensional with a star-of-David hexagonal structure [Figure A.1(a)], undergoes a commensurate CDW transition forming a $\sqrt{13} \times \sqrt{13}$ superstructure at $T = 180$ K. Additionally, this material exhibits a state called Mott insulator, which generally occurs when Coulomb repulsion is strong enough to create a gap in the Fermi surface. Figures A.1(b, c) show STM images of the formation of different domain walls (DW) in 1T-TaS$_2$. The formation of DWs is connected to the propagation vector of the CDW and extends in an irregular network with typical sizes up to several hundred nanometers [22, 23]. It has been shown that these domain walls can be manipulated by exciting the material through laser pulses or voltage pulses, and in turn, the formation of DWs has a significant impact on the electronic properties of the compound. For example, a metallic state is induced from the Mott insulating state, indicating that CDW domain walls may be correlated with the Mott state [22]. Another similar compound is 1T-TiSe$_2$, which below T = 202 K exhibits a CDW that can be suppressed by hydrostatic pressure, giving rise to a superconducting state. X-ray diffraction studies under pressure have shown a possible correlation of domain formation with the emergence of superconductivity, as it emerges in the vicinity of a commensurate-to-incommensurate (C/I) CDW transition and not exactly where the CDW is completely suppressed by hydrostatic pressure [24]. In the phase diagram of Figure A.2, we can see that superconductivity, represented by the red region, is close to where the C/I transition of the CDW occurs, around $P = 3$ GPa, while the complete suppression occurs around $P = 5$ GPa. In these examples, CDW domain structures can play an important role in the properties of materials and the emergence of other fundamental states. Therefore, characterizing this type of structure becomes relevant for understanding the nature of states of matter and also for the possibility of manipulating these properties for technological purposes.

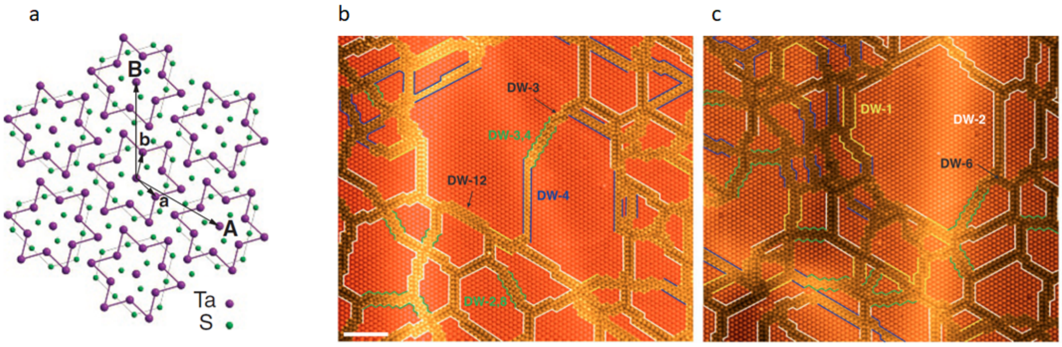

Figure A.1: (a) Structure of the compound 1T-TaS$_2$. Figure from [22]. (b, c) Charge density wave domain walls in the compound 1T-TaS$_2$. Figure from [23].

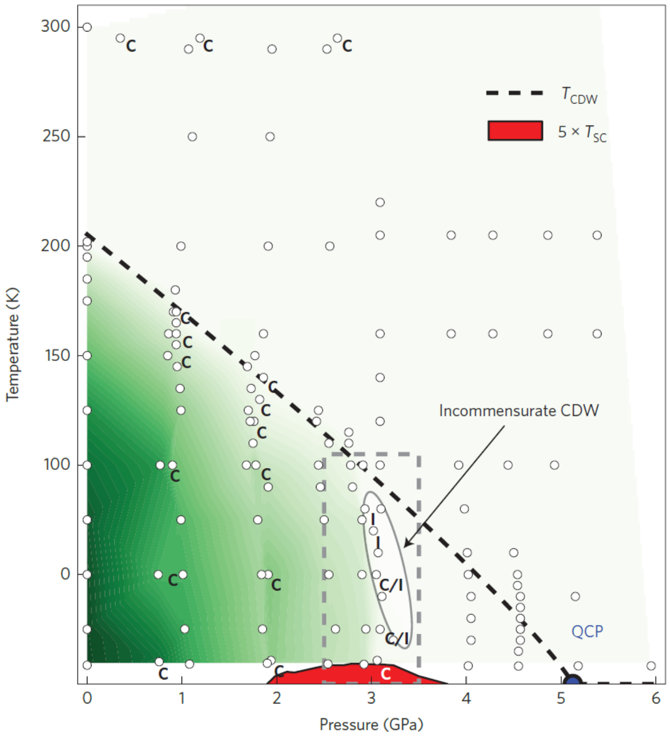

Figure A.2: Phase diagram $T \times P$ of the compound 1T-TiSe$_2$ [24].

CDW in $(\mathrm{Sr}_{1-x}\mathrm{Ca}_x)_3\mathrm{Rh}_4\mathrm{Sn}_{13}$

The compound studied in this project was $(\mathrm{Sr}_{1-x}\mathrm{Ca}_x)_3\mathrm{Rh}_4\mathrm{Sn}_{13}$ with $x = 0.6$. This belongs to the family of $\mathrm{R}_3\mathrm{T}_4\mathrm{Sn}_{13}$ compounds (R = rare earth or alkaline earth metal, T = transition metal), most of which exhibit commensurate charge density waves with propagation vector $\mathbf{q}_{CDW} = (0.5\ 0.5\ 0)$. Unlike the compounds mentioned earlier, this family has a three-dimensional character, making it an interesting platform for studying CDW in higher dimensions. As mentioned earlier, CDW manifest in macroscopic measurements, and for this compound, it is no different. In Figure A.3(a), resistivity curves as a function of temperature for different pressures applied to the compound $\mathrm{Sr}_3\mathrm{Rh}_4\mathrm{Sn}_{13}$ are shown. The increase in electrical resistivity around the transition (T^*) is associated with the partial opening of the gap in the Fermi surface, and superconductivity emerges around $T_c \sim 4.7$ K. Here, the CDW can be suppressed both by hydrostatic pressure and by increasing the concentration of Calcium in the system. Looking at the phase diagram, we see that T_c reaches its maximum at $x = 0.9$, where the CDW can no longer be observed [Figure A.3(b)]. There is also evidence of quantum criticality at the point where the CDW disappears, such as non-Fermi liquid behavior of the electrical resistivity and the increase in the ratio between the specific heat jump at the superconducting transition and T_c ($\Delta C_p/T_c$) [13, 25]. The interaction between CDW and superconductivity in this material is not yet fully understood, and the study of domain structure may be important for understanding this mechanism, as is the case with low-dimensional materials. For the study of this domain structure, composition $x = 0.6$ was chosen so that the CDW superstructure peaks are still present in X-ray diffraction, and the superconducting transition temperature is high enough to be accessed with the cryostats used in this work.

Synthesis and characterization of the compound

Single crystals of $\mathrm{Sr}_{0.4}\mathrm{Ca}_{0.6}\mathrm{Rh}_4\mathrm{Sn}_{13}$ with typical sizes of 1 - 4 mm were synthesized using the metal flux technique [26]. To determine the macroscopic physical properties, we used measurements of electrical resistivity and magnetic susceptibility to observe the CDW and superconducting transitions. Figure A.4(a) shows the resis-

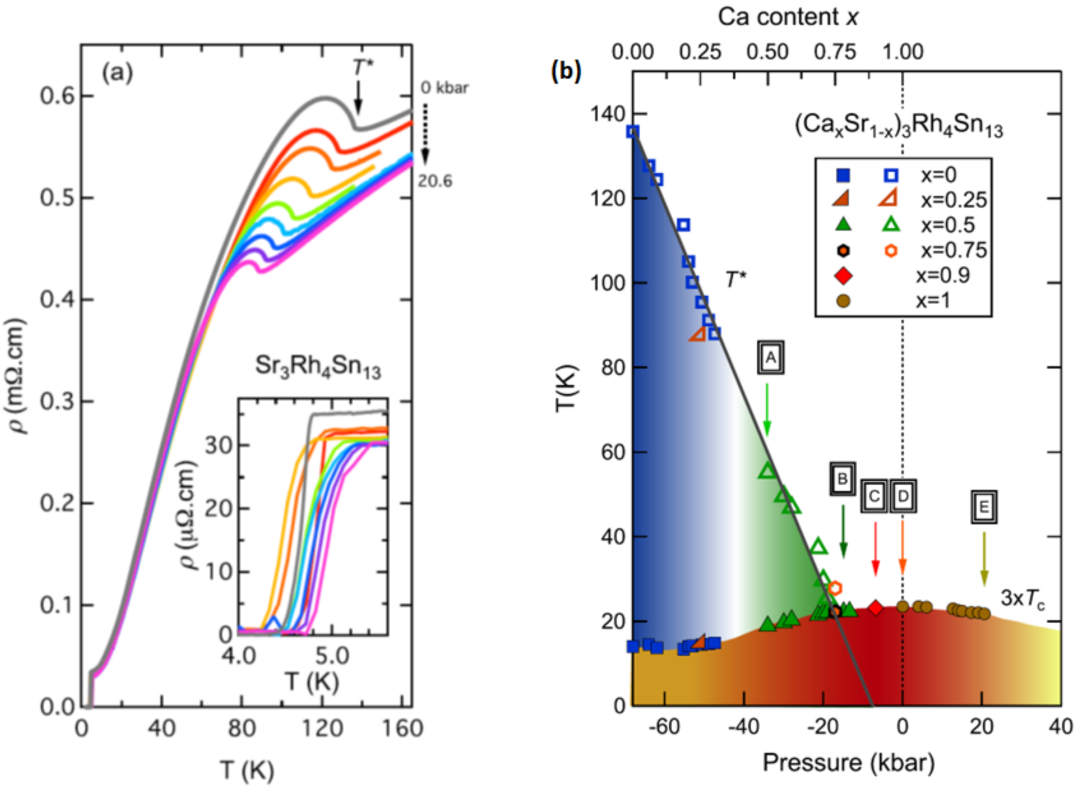

Figure A.3: (a) Resistivity curves as a function of temperature for different applied pressures. (b) Phase diagram $T \times P, x$ of the compound $(Sr_{1-x}Ca_x)_3Rh_4Sn_{13}$ [13].

tivity curve, its derivative (b), and the magnetic susceptibility (c) as a function of temperature. We observe that the CDW transition occurs around $T_{CDW} \sim 40$ K and the superconducting transition arises around $T_c \sim 7.5$ K [inset figure A.4(a)], both in agreement with values reported previously in the literature for this Calcium concentration [13]. In our preliminary X-ray diffraction experiments on single crystals at low temperatures, we observed the temperature dependence of the superstructure peak related to the CDW transition, as expected for charge ordering systems [figure A.5(a). Interestingly, we do not observe a quench of the CDW reflection across the superconducting transition, which indicate an absence of competition between these states. For the DFXM experiments, a piece of single crystal was polished to a thickness of 150 μm and oriented using Laue diffraction with its surface perpendicular to the [110] direction, as shown in figure A.6(a and b).

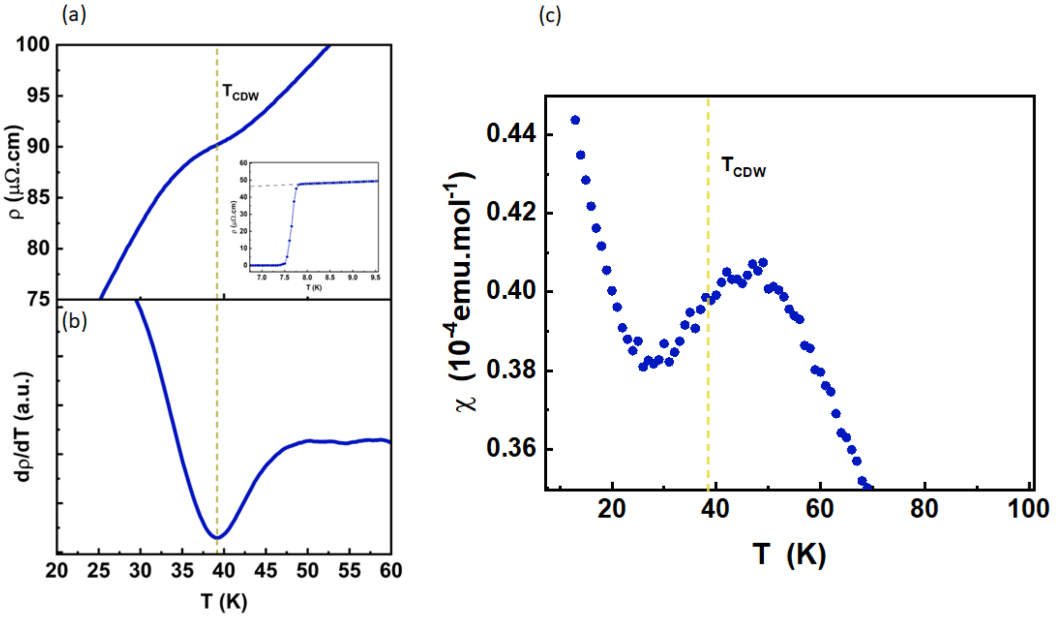

Figure A.4: . (a) Electrical resistivity as a function of temperature and its first derivative (b). Magnetic susceptibility as a function of temperature (c).

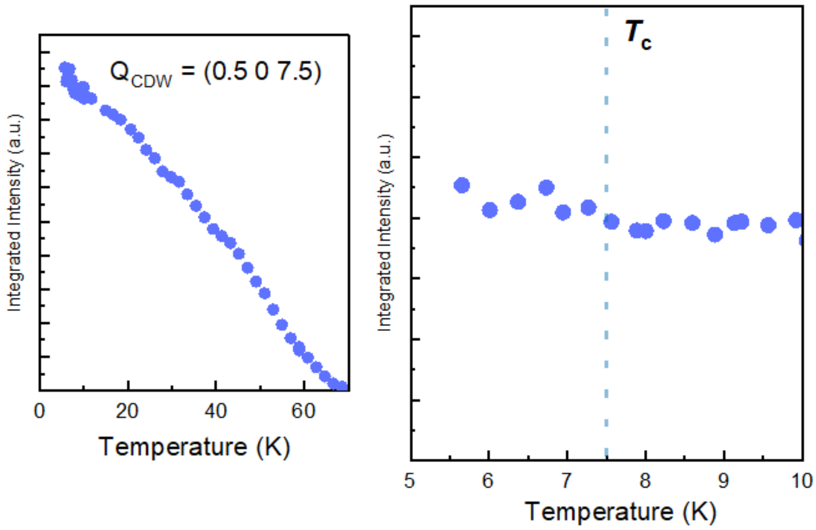

Figure A.5: (a) Temperature dependence of the reflection $Q_{CDW} = (0.5\ 0\ 7.5)$.

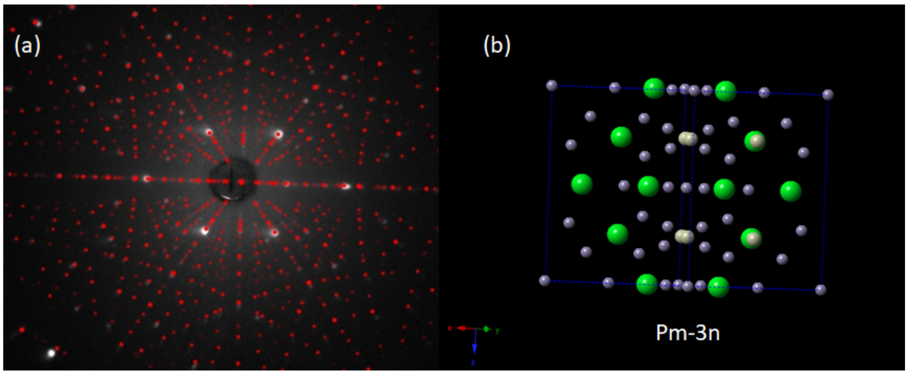

Figure A.6: (a) Laue diffraction pattern of the [110] direction perpendicular to the crystal surface. (b) Orientation of the crystal structure obtained by Laue diffraction.

Dark Field X-ray Microscopy (DFXM)

As briefly mentioned in the introduction, DFXM has proven to be a powerful tool for characterizing materials on multiple scales. In this section, we describe the functioning of this technique and how it can aid in the study of CDW domains. DFXM is a full-field technique that allows imaging of the projection of an illuminated volume of the sample with resolutions of the order of 100 nm. DFXM is based on X-ray diffraction and is conceptually similar to dark-field techniques used in transmission electron microscopy. However, since X-rays have high penetration power, it allows a non-destructive study of bulk materials, i.e., materials with thicknesses of the order of hundreds of micrometers. The basic principle of DFXM is to magnify the X-rays diffracted by the material using polymer compound refractive lenses (pCRLs) designed to focus X-rays. A monochromatic beam from a synchrotron source is incident on the sample under diffraction conditions, and the diffracted beam is subsequently magnified by the polymer lenses, generating an inverted image in the real space of the illuminated volume (Figure A.7). Images can be obtained by rotating the sample slightly around the diffraction angle θ to obtain different projections of the illuminated volume, providing a mosaic mapping of the region of interest, and enabling to scan different regions of the sample by translating the sample relative to the beam. These real-space images will have contrast due to local variations in crystal lattice symmetry, orientation, and strain [27]. Images are obtained by positioning 2D detectors in the image plane, and magnification can be adjusted by modifying the sample-lens-detector distance. The 6-ID-C line, where the experiments were conducted, is equipped with a high-resolution diffractometer, pCRLs with an effective aperture of 68× 68 μm optimized to operate at 20 keV. We have used two types of area detectors, Zyla sCMOS, which is a scintillator-type detector with an effective pixel size of 6.5×6.5 μm and optical magnification of 5x, and Lambda, which uses direct detection with a pixel size of 55×55 μm. The latter is particularly important for obtaining images of CDW diffraction peaks, as these peaks generally have low intensity compared to structure peaks. Imaging techniques, usually require high intensity beams, in the case of DFXM, where the imaging is performed at the diffraction condition, a reasonable intensity can be achieved for structural peaks. However, for CDW, the satellite peaks are frequently have intensities of a

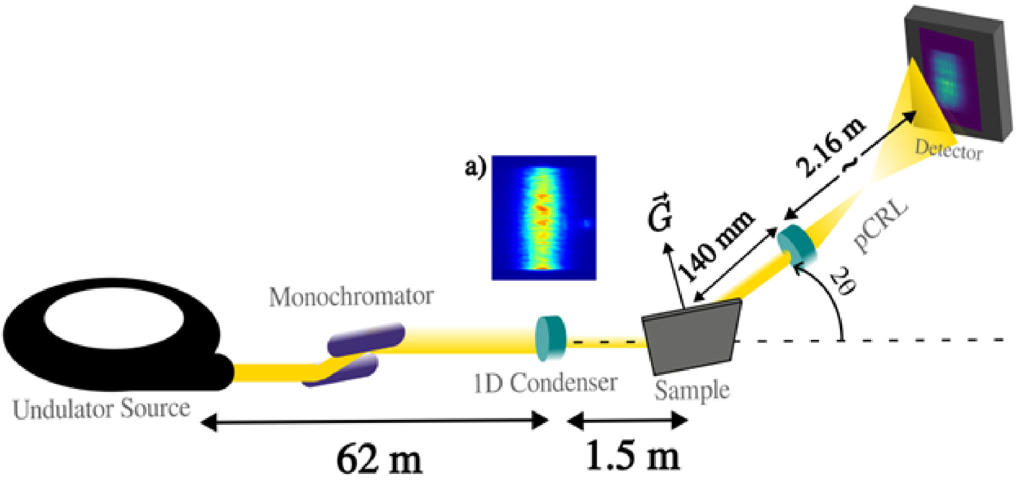

Figure A.7: Scheme of the DFXM experiment. Figure from reference [10].

order of million/billion times lower than the peaks from the pristine structure. For low-temperature experiments, the low-vibration Montana cryostat was used, which has a beryllium window for diffraction experiments and can operate at temperatures between 3 - 300 K (see figure A.8).

Experimental Procedure

In order to spatially characterize the CDW in the compound of interest, the following experimental procedure was performed. A sample of $Sr_{0.4}Ca_{0.6}Rh_4Sn_{13}$ with a thickness of 150 μm was mounted in the cryostat, cooled to $T = 3 < T_c = 7.5 < T_{CDW} = 40$ K, and aligned so that the peak $Q_{CDW} = (9/5\ 7/5\ 0)$ is in diffraction condition. The sample was illuminated with a nearly-1D beam with dimensions of 20×200 μm to enable vertical cuts in different regions within the sample volume. The pCRLs and detector were aligned with the diffracted beam to obtain images containing spatially resolved diffraction contrast of the CDW electronic modulation. A pinhole with aproximated diameter of ≈ 40 μm diameter is placed between the sample and the lenses in order to keep the same field of view and prevent any other light but the diffracted to pass through the lens. The focal length of the pCRLs for

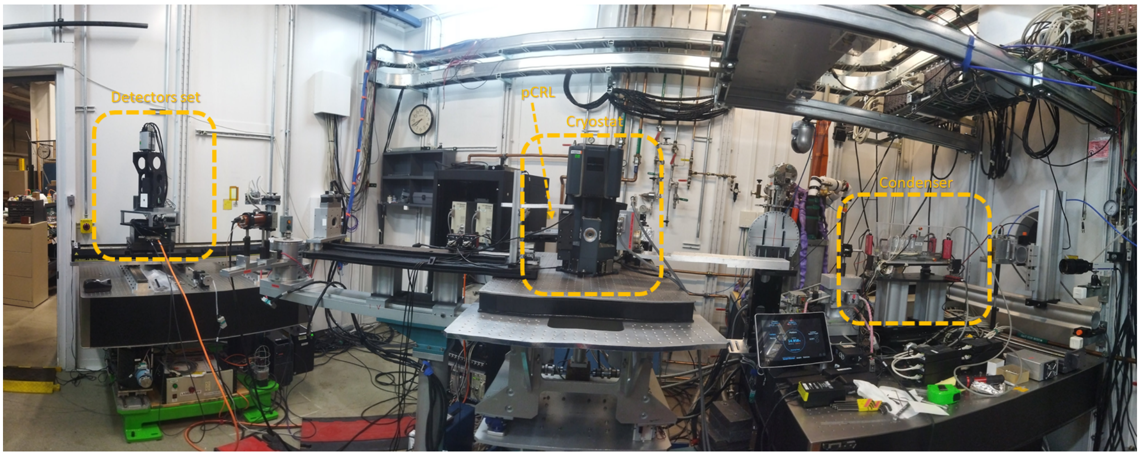

Figure A.8: Experimental setup of DFXM at the 6-ID-C beamline.

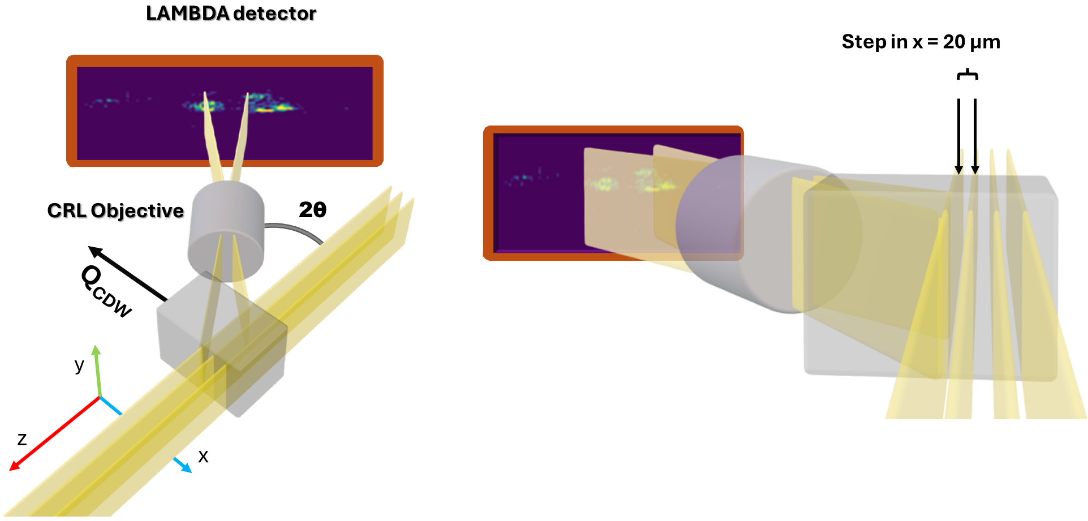

Figure A.9: Schematics of the procedure performed for CDW spatial mapping.

the energy used (20 keV) is 131 mm, giving us a magnification of × 26. Subsequently, the sample was systematically translated in intervals of 20 μm in the horizontal (x) and vertical (y) directions (see figure A.9) until covering an area of 300×900 μm, and for each x and y position, an image was obtained; The x, y, z coordinate system is defined relative to the laboratory. At each x and y position, we rock the sample around the scattering vector Q_{CDW} = (9/5 7/5 0), taking one image at each theta value θ in steps of $\Delta\theta \approx 0.005°$. This theta positions are marked as yellow stars in figure A.10b.

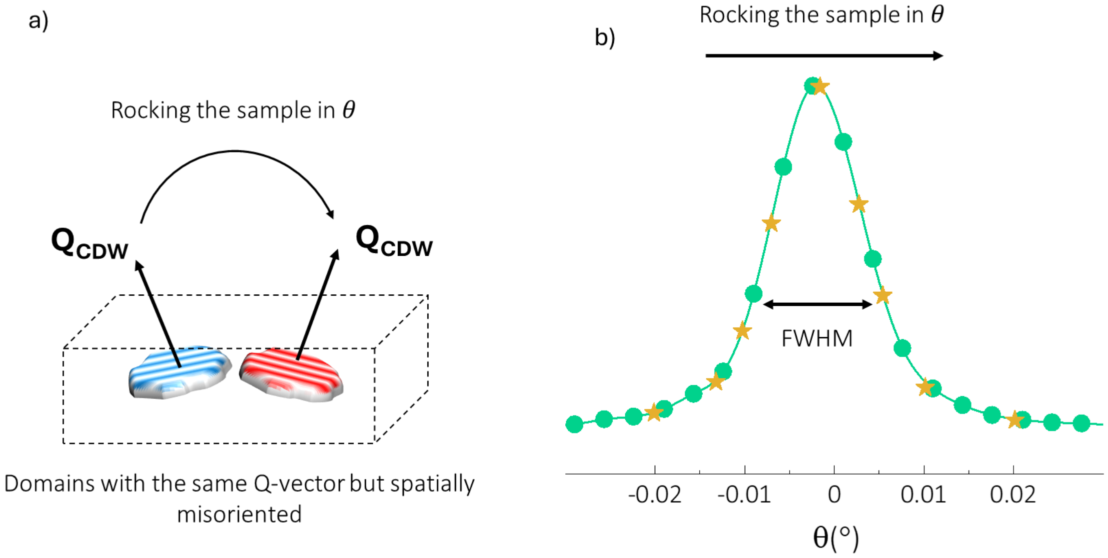

Figure A.10: (a) Schematics showing different misaligned domains related to the same CDW wave vector. (b) Example of a rocking curve around the CDW peak Q_{CDW} = (9/5 7/5 0) of $Sr_{0.4}Ca_{0.6}Rh_4Sn_{13}$, measured using a point detector.

The procedure described above is called rocking curve image (RCI), and it gives information of how different domains related to that specific scattering vector are distributed spatially within the illuminated area. By slightly rocking the sample around the diffraction condition, keeping the 2θ angle fixed, different misaligned domains will be aligned in diffraction condition (see figure A.10a). Note that, this is not necessarily related to strain, since the 2θ angle is kept fixed, it means that we are probing the same interplanar distance. When a simple diffraction experiment is performed, we loose the spatial resolution and the domain distribution is reflected in an enlargement of the rock curve peak width (or Full width at half maximum [FWHM]), therefore all information about the domain distribution is averaged in a single peak, as shown in figure A.10b. However, when the diffracted beam is magnified by the lenses, one can separate this contributions and recover the spatial information.

Two main large data sets were taken at T = 15 and 3 K, covering an area of 300 × 900 μm. This process was also repeated for different temperatures below and above the superconducting state in a reduced area of 100 × 300 μm to observe the correlation of the CDW spatial distribution with the superconducting state. Additionally, images of the original structure were made in the same volume by aligning the Bragg peak $Q_{Bragg} = (3\ 2\ 0)$ and repeating the experiment for various temperatures, now using the Zyla sCMOS detector, which has higher resolution. With this dataset, we hope to observe the connection of the CDW with the primitive structure of the material and its intrinsic defects. In addition how the CDW domain distribution is affected by the onset of the superconductivity. The images obtained are proccessed using an adapted version of the *darfix* code [28].

Data analysis and preliminary results

Most of the data analysis were done using the *darfix* python package [28], which enables fast processing and visualization of the DFXM data. Before get in to the principal analysis, all the data is cropped around the region of interest (ROI), in order to reduce the computational costs. A background subtraction is performed to give a consistent background with dark images collected during the scans, used as reference. The analysis is performed computing the Gaussian moments. Each pixel in the image is fitted using a peak profile, e.g., a Gaussian. The zeroth-order moment corresponds to the integrated intensity, the first-order moment is called center of mass (COM) to the peak position and the second-order moment is the variance to the square peak width. The measured intensity of a pixel, $I_{uv,\mathrm{meas}}$, where uv indicates the pixel position within the image, as a function of the motor position, i.e., the rocking angle θ, is fitted to a Gaussian.

$$I_{uv,\text{fit}}(\theta) = b_{uv} + A_{uv}\text{exp}\left[-\frac{1}{2}\frac{(\theta - p_{uv})^2}{\sigma_{uv}^2}\right]. \tag{A.1}$$

Fitting all pixel in the image, results in maps of the background (b_{uv}), amplitude

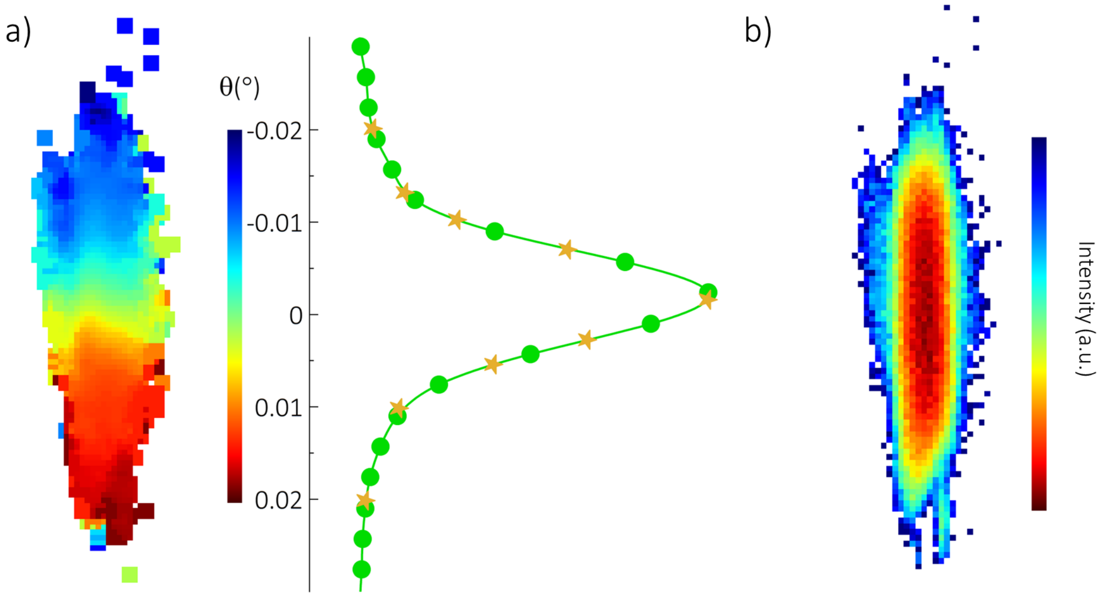

Figure A.11: (a) COM of the CDW peak Q_{CDW}, showing to main domains locally misoriented. (b) Sum of all images at the same xy position in the sample at different θ angles, recovering the diffraction peak.

(A_{uv}), peak position (p_{uv}) and peak width (σ_{uv}), where the FHWM $= 2.355\sigma_{uv}$. The COM is one of the most important moment for identifying the CDW domains, it corresponds to the local orientation of different domains in the illuminated area. The figure A.11a shows the COM image around the CDW peak Q_{CDW}, shown on the right of the image. The colormap represents the rocking angle varying from the center of the peak by ±0.02 °. This image was taken at $T = 15$ K at one single beam position xy in the sample (see the coordinates of the sample regarded to the beam in figure A.9). In figure A.11b the summed images in all θ positions recover the diffraction beam, as one can see, we loose the spatial information. From the COM image we can readily identify the existence of two main CDW domains locally misoriented (low-angle in blue and high-angle in red). We probed the sample by slicing it at each 20 μm in x and y. Therefore, each single image as shown in the figure A.11a, have an x and y position corresponding to the position of the beam in the sample. To reconstruct the entire probed volume we must stitch the images in y, side by side, and stack them in x one on top of each other, by the same distance of the step used for slicing. In x there is no overlap between the subsequent images, since the beam width and the step size was the same (20 μm). In y, the size of the beam hitting the detector is about 40 μm (limited by the pinhole diameter), which is larger than the step, so the images must be properly overlapped. The figure A.12 show a collection of COM images at $T = 15$ K. Along the y axis, the images are already stitched (i.e., multiple COM images as shown in A.11a placed side by side, using the correct overlap between them) and the images are stacked in x. The total length for a single slice in this figure 900 μm in y, 20 μm in x, and 40 μm in z (limited by the FOV). Therefore, after combining every x slice, we obtain a total of $7 \times 20 = 140$ μm.

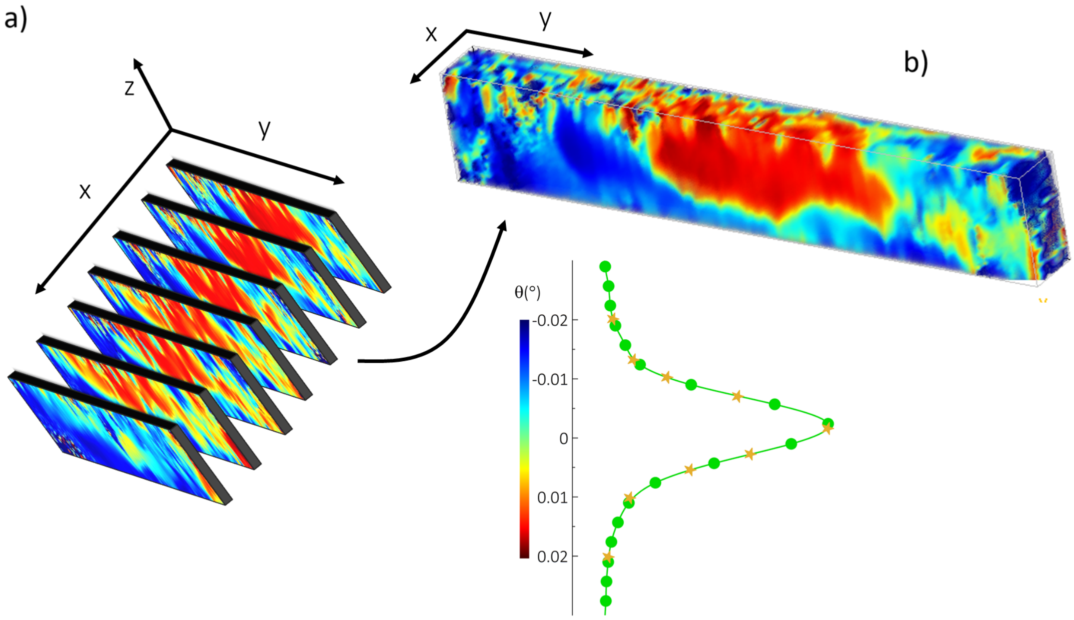

Figure A.12: (a) Different COM images already merged in y, representing multiple x positions in the sample. These slices are used to reconstruct in 3D the probed volume. (b) Reconstructed volume of the Q_{CDW} peak COM. The scale is show below altogether with the diffraction peak as in the previous images.

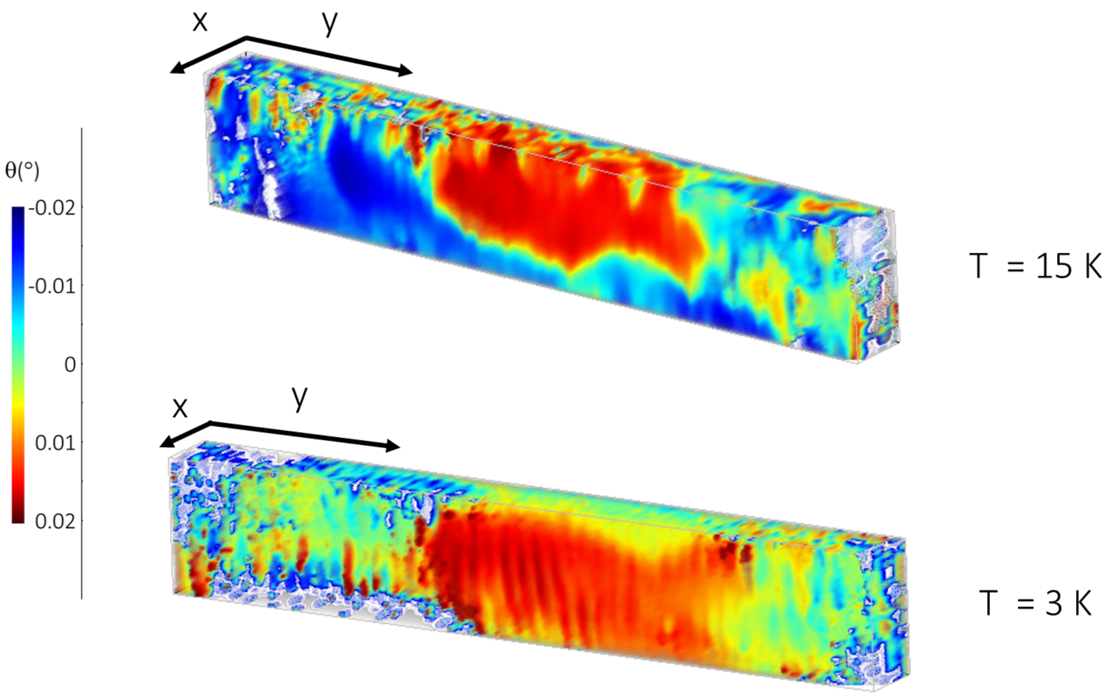

Figure A.13: COM volume for two temperatures, above (upper panel) and below (lower panel) T_c.

Indeed, this was the final goal, reconstruct the probed volume and create a 3D view of the CDW domain distribution. This can be achieve by interpolating the slices, since there are no gaps or overlaps between the slices one can use different types of interpolations to create a correlation between the subsequent slices, and reconstruct the volume. In a first attempt, we used the software FIJI ImageJ, with the 3D volume viewer plug-in [29]. The resulting volume is shown in figure A.12b, one can now identify the distribution of the two main observed domains in a 3D space. As can be inferred, the domain in blue dominates the volume at this temperautre and the high-angle domain (red) is mainly located in the center of the volume. The same analysis was performed $T = 3$ K, below the superconducting transition and it is show in figure A.13. The upper volume is at $T = 15$ K and the lower is at $T = 3$ K. Since the same region in the sample was probed one, at this moment, qualitatively compare them. We see an important change in the distribution of the domains. While above T_c there is two clear well separated domains, below T_c the low-angle domain is smeared out and the distribution is mainly lies in the higher angles.

Next steps

To better understand this changes across the superconducting transition, small volumes of the sample were probed in small steps of temperature (4, 4.5, 5, 5.5, 6, 6.5, 7, 7.5, 8 K). This analysis is in progress. Moreover, in order to compare the CDW domains with possible twinning effects of the pristine structure other data sets were taken with the microscope aligned with the Bragg peak (3 2 0). The volume reconstructions are also being performed using the Software Aviso 3D, from Thermo Fischer, which offer better tools for interpolation between slices and segmentation of the domains, so that one can have a quantitative analysis.

Bibliography

[1] Wang Z. Z., Girard J. C., Pasquier C., Jérome D., and Bechgaard K., “Scanning Tunneling Microscopy in TTF-TCNQ: Phase and Amplitude Modulated Charge Density Waves.” Physical Review B 67, no. 12 (March 5, 2003): 121401. https://doi.org/10.1103/PhysRevB.67.121401.

[2] Hu Y., Tianzhen Z., Dongming Z., Chen C., Shuyue D., Wentao Y., Xu W., et al., “Real-Space Observation of Incommensurate Spin Density Wave and Coexisting Charge Density Wave on Cr (001) Surface.” Nature Communications 13, no. 1 (January 21, 2022): 445. https://doi.org/10.1038/s41467-022-28104-2.

[3] Sakabe D., Zheng L., Kazutomo S., Keiji N., and Satoshi T., “Direct Observation of Mono-Layer, Bi-Layer, and Tri-Layer Charge Density Waves in 1T-TaS_2 by Transmission Electron Microscopy without a Substrate.” Npj Quantum Materials 2, no. 1 (April 25, 2017): 1–6. https://doi.org/10.1038/s41535-017-0025-8.

[4] Kutsal M., Bernard P., Berruyer G., Cook P. K., Hino R., Jakobsen A. C., Ludwig W., et al., “The ESRF Dark-Field x-Ray Microscope at ID06.” IOP Conference Series: Materials Science and Engineering 580, no. 1 (August 1, 2019): 012007. https://doi.org/10.1088/1757-899X/580/1/012007.

[5] Dresselhaus-Marais L. E., Grethe W., Howard M., Gonzalez A., Breckling S. R., Yildirim C., Cook P. K. Kutsal M., Hugh S. and Detlefs C., “In Situ Visualization of Long-Range Defect Interactions at the Edge of Melting.” no. 7, Issue 29 (July 14, 2021). https://doi.org/10.1126/sciadv.abe8311.

[6] Simons H., Astri B. H., Anders C. J., Søren S., Frederik S., Marta M., Carsten D., Daniels J. E., Dragan D. and Henning F. P., "Long-Range Symmetry Breaking in Embedded Ferroelectrics." Nature Materials 17, no. 9 (September 2018): 814–19. https://doi.org/10.1038/s41563-018-0116-3.

[7] Cook P. K., Simons H., Anders C. J., Yildirim C., Henning F. P., and Detlefs C., "Insights into the Exceptional Crystallographic Order of Biominerals Using Dark-Field X-Ray Microscopy." Microscopy and Microanalysis 24, no. S2 (August 2018): 88–89. https://doi.org/10.1017/S1431927618012837.

[8] Abulshohoud O., Poudyal I., McChesney J., Zhang Z., Qiao Z., Welp U., and Islam Z., "A General Method for Multiresolutional Analysis of Mesoscale Features in Dark-Field x-Ray Microscopy Images." arXiv, October 27, 2022. https://doi.org/10.48550/arXiv.2210.15757.

[9] Qiao Z., Xianbo S., Kenesei P., Last A., Assoufid L., and Islam Z., "A Large Field-of-View High-Resolution Hard x-Ray Microscope Using Polymer Optics." Review of Scientific Instruments 91, no. 11 (November 11, 2020): 113703. https://doi.org/10.1063/5.0011961.

[10] Kisiel E., Poudyal I., Kenesei P., Engbretson M., Last A., Basak R., Zaluzhnyy I., et al. "Full-Field Nanoscale X-Ray Diffraction-Contrast Imaging Using Direct Detection." arXiv, January 4, 2023. http://arxiv.org/abs/2212.07303.

[11] Plumb J., Poudyal I., L. Dally R. L., Daly S., D. Wilson S. D., and Islam Z., "Dark Field X-Ray Microscopy Below Liquid-Helium Temperature: The Case of NaMnO2." arXiv, November 16, 2022. https://doi.org/10.48550/arXiv.2211.09247.

[12] Mendonça-Ferreira L., Carneiro F. B., Fontes M. B., Baggio-Saitovitch E., Veiga L. S. I., Mardegan J. R. L., Strempfer J., Bittar E.M., "Pressure Effects on the Structural and Superconducting Transitions in La3Co4Sn13." Journal of Alloys and Compounds 773 (January 30, 2019): 34–39. https://doi.org/10.1016/j.jallcom.2018.09.236.

[13] Goh S.K., Tompsett D.A., Saines P.J., Chang H.C., Matsumoto T., Imai M., Yoshimura K. and Grosche F.M. "Phys. Rev. Lett. 114,

097002 (2015) - Ambient Pressure Structural Quantum Critical Point in the Phase Diagram of $(\mathrm{Ca}_x\mathrm{Sr}_{1-x})_3\mathrm{Rh}_4\mathrm{Sn}_{13}$.” Accessed July 15, 2023. https://journals.aps.org/prl/abstract/10.1103/PhysRevLett.114.097002.

[14] Klintberg L. E., Goh S. K., Alireza P. L., Saines P. J., Tompsett D. A., Logg P. W., Yang J., Chen B., Yoshimura K., and Malte Grosche F., “Pressure- and Composition-Induced Structural Quantum Phase Transition in the Cubic Superconductor $(\mathrm{Sr},\mathrm{Ca})_3\mathrm{Ir}_4\mathrm{Sn}_{13}$.” Physical Review Letters 109, no. 23 (December 5, 2012): 237008. https://doi.org/10.1103/PhysRevLett.109.237008.

[15] Peierls, Rudolf Ernst. Quantum Theory of Solids. Clarendon Press, 1955.

[16] Fröhlich H., “Electrons in Lattice Fields.” Advances in Physics 3, no. 11 (July 1954): 325–61. https://doi.org/10.1080/00018735400101213.

[17] Grüner G., “The Dynamics of Charge-Density Waves.” Reviews of Modern Physics 60, no. 4 (October 1, 1988): 1129–81. https://doi.org/10.1103/RevModPhys.60.1129.

[18] Johannes M. D. and Mazin I. I., “Fermi Surface Nesting and the Origin of Charge Density Waves in Metals.” Physical Review B 77, no. 16 (April 30, 2008): 165135. https://doi.org/10.1103/PhysRevB.77.165135.

[19] Chu C. W., Harper J. M. E., Geballe T. H. and Greene R. L., “Pressure Dependence of the Metal-Insulator Transition in Tetrathiofulvalinium Tetracyanoquinodimethane (TTF-TCNQ).” Physical Review Letters 31, no. 25 (December 17, 1973): 1491–94. https://doi.org/10.1103/PhysRevLett.31.1491.

[20] Kenji K., Ishizaka K., Kiss T., Okawa M., Kato R. and Shin S., “Bulk-Sensitive Angle-Resolved Photoemission Spectroscopy on TTF-TCNQ.” Journal of the Physical Society of Japan 82, no. 2 (February 15, 2013): 025004. https://doi.org/10.7566/JPSJ.82.025004.

[21] Wang H. T., Srivastava M. K., Wu C. C., Hsieh S. H., Wang Y. F., Shao Y. C., Liang Y. H., et al. “Electronic and Atomic Structures of the Sr3Ir4Sn13 Single Crystal: A Possible Charge Density Wave Material.” Scientific Reports 7, no. 1 (January 20, 2017): 40886. https://doi.org/10.1038/srep40886.

[22] Liguo M., Ye C., Yu Y., Fang Lu X., Niu X., Kim S., Feng D., et al. “A Metallic Mosaic Phase and the Origin of Mott-Insulating State in 1T-TaS2.” Nature Communications 7, no. 1 (March 10, 2016): 10956. https://doi.org/10.1038/ncomms10956.

[23] Park J. W., Lee J., and Yeom H. W., “Zoology of Domain Walls in Quasi-2D Correlated Charge Density Wave of 1T-TaS2.” Npj Quantum Materials 6, no. 1 (March 22, 2021): 1–6. https://doi.org/10.1038/s41535-021-00330-9.

[24] Joe Y. I., Chen X. M., Ghaemi P., Finkelstein K. D., de la Peña G. A., Gan Y., Lee J. C. T., et al. “Emergence of Charge Density Wave Domain Walls above the Superconducting Dome in 1T-TiSe2.” Nature Physics 10, no. 6 (June 2014): 421–25. https://doi.org/10.1038/nphys2935.

[25] Yu, Wing Chi, Yiu Wing Cheung, Paul J. Saines, Masaki Imai, Takuya Matsumoto, Chishiro Michioka, Kazuyoshi Yoshimura, and Swee K. Goh. “Strong Coupling Superconductivity in the Vicinity of the Structural Quantum Critical Point in $(Ca_xSr_{1-x})_3Rh_4Sn_{13}$.” Physical Review Letters 115, no. 20 (November 11, 2015): 207003. https://doi.org/10.1103/PhysRevLett.115.207003.

[26] Tachibana, Makoto. Beginner’s Guide to Flux Crystal Growth. NIMS Monographs. Tokyo: Springer Japan, 2017. https://doi.org/10.1007/978-4-431-56587-1.

[27] Simons H., King A., Ludwig W., Detlefs C.,Pantleon W. ,Schmidt S., Stöhr F., Snigireva I., Snigirev A., and Poulsen H. F. “Dark-Field X-Ray Microscopy for Multiscale Structural Characterization.” Nature Communications 6, no. 1 (January 14, 2015): 6098. https://doi.org/10.1038/ncomms7098.

[28] Ferrer J. G., Rodríguez-Lamas R., Payno H., De Nolf W., Cook P., Solé Jover V. A., Favre-Nicolin V., Yıldırım C., and Detlefs C,. “Darfix: Data Analysis for Dark-Field X-Ray Microscopy.” arXiv, May 11, 2022. https://doi.org/10.48550/arXiv.2205.05494.

[29] Schneider, C. A., Rasband, W. S., and Eliceiri, K. W. (2012). NIH Image to ImageJ: 25 years of image analysis. Nature Methods, 9(7), 671–675. doi:10.1038/nmeth.2089

Appendix B

Publications

- **F. B. Carneiro**, L. S. I. Veiga, J. R. L. Mardegan, R. Khan, C. Macchiutti, A. López, and E. M. Bittar, *Unveiling charge density wave quantum phase transitions by x-ray diffraction*, Phys. Rev. B **101**, 195135 (2020).
- **F. B. Carneiro**, M. O. Ajeesh, C. Girod, C. S. Kengle, G. S. Freitas, P. G. Pagliuso, E.M. Bittar, S. M. Thomas, and P. S. F. Rosa, *Tunning the Charge Density Wave correlations ScV_6Sn_6 by c-axis stress.* (2024) - preprint.
- **F. B Carneiro**, C. Girod, G. S. Freitas, P. G. Pagliuso, P. F. S. Rosa, S. M. Thomas and E. M. Bittar, *Uniaxial pressure effect on superconducting and charge density wave transitions in $La_3Co_4Sn_{13}$.* (2024) - preprint.

Appendix C

Co-authorship publications

- L. S. I. Veiga, J. R. L. Mardegan, M. V. Zimmermann, D. T. Maimone, **F. B. Carneiro**, M. B. Fontes, J. Strempfer, E. Granado, P. G. Pagliuso, and E. M. Bittar, PossibleQuantum Fluctuations in the Vicinity of the Quantum Critical Point of $(Sr, Ca)_3Ir_4Sn_{13}$ Revealed by High-Energy x-Ray Diffraction, Phys. Rev. B, **101** (10), 104511 (2020).
- C. Macchiutti, J. R. Jesus, **F. B. Carneiro**, L. Bufaiçal, M. Ciomaga Hatnean, G.Balakrishnan, and E. M. Bittar, *Absence of Zero-Field-Cooled Exchange Bias Effect in Single Crystalline* $La_{2-x}A_xCoMnO_6$ *(A = Ca, Sr) Compounds*, Phys. Rev. Mater. **5**, 094402 (2021).
- C. Macchiutti, J. R. Jesus, **F. B. Carneiro**, L. Bufaical, R. A. Klein, Q. Zhang, M.Kirkham, C. M. Brown, R. D. dos Reis, and E. M. Bittar, *Tuning the Spontaneous Exchange Bias Effect in* $La_{1.5}Sr_{0.5}CoMnO_6$ *with Sintering Temperature*, arXiv:2312.09149 (2023). (preprint).
- E. Kisiel, P. Salev, I. Poudyal, **F. Carneiro**, F. Rodolakis, Z. Zhang, O. Shpyrko, I. K.Schuller, Z. Islam, and A. Frano, *High-Resolution Full-Field Structural Microscopy of the Voltage Induced Filament Formation in Neuromorphic Devices*, arXiv:2309.15712 (2023). (preprint).
- G. S. Freitas, Kevin R. Pakuszewski, Alisson P. Machado, H. Pizzi, **F. B. Carneiro**, E.M. Bittar, C. Adriano, A. D. Bianchi, E. D. Bauer, J. D. Thompson, F. Ronning, S. M. Thomas, P. F. S. Rosa, Y. Kopelevich and P. G.

Pagliuso, *Putative non-trivial topology in* $YNiSn_2$ *Dirac semimetal* (2024) - preprint.

- G. S. Freitas, S. G. Mercena, C. B. R. Jesus, C. Adriano, M. M. Piva, C. Souza, H. B.Pizzi, A. M. Caffer, **F. B. Carneiro**, M. H. Carvalho, C. Girod, M. M. Bordelon, X. Gratens,E. D. Bauer, F. Ronning, J. D. Thompson, S. M. Thomas, Z. Fisk, N. F. Oliveira Jr., D. J.Garcia, P. F. S. Rosa and P. G. Pagliuso. *De Gennes scaling breakdown in the* $RTBi_2$ *(R = Ce, Pr, Nd; T = Cu, Au) series: the role of crystal field effects and anisotropic magnetic interactions.* (Submitted to Physical Review B.).

- G. S. Freitas, H. Pizzi, **F. B. Carneiro**, M. H. Carvalho, E. M. Bittar, E. D. Bauer, J. D.Thompson, F. Ronning, S. M. Thomas, P. F. S. Rosa, S. M. Greer and P. G. Pagliuso, *Electron Spin Resonance (ESR) on* $GdCuBi_2$ *Intermetallic Antiferromagnet.* (2024) - preprint.